Univerza
v Ljubljani
Fakulteta
za gradbeništvo
in geodezijo

Jamova cesta 2
1000 Ljubljana, Slovenija
http://www3.fgg.uni-lj.si/

DRUGG – Digitalni repozitorij UL FGG
http://drugg.fgg.uni-lj.si/

V zbirki je izvirna različica izdajatelja.

Prosimo, da se pri navajanju sklicujete na bibliografske podatke, kot je navedeno:

University
of Ljubljana
Faculty of
Civil and Geodetic
Engineering

Jamova cesta 2
SI – 1000 Ljubljana, Slovenia
http://www3.fgg.uni-lj.si/en/

DRUGG – The Digital Repository
http://drugg.fgg.uni-lj.si/

This is a publisher's version PDF file.

When citing, please refer to the publisher's bibliographic information as follows:

Pečenko, R. 2016. Mehanski odziv ukrivljenih lesenih nosilcev s spremenljivo višino pri požarni obtežbi. Doktorska disertacija. = Mechanical response of curved timber beams with variable height under fire conditions. Doctoral dissertation. Ljubljana, Univerza v Ljubljani, Fakulteta za gradbeništvo in geodezijo: 121 str. (mentor: doc. dr. Tomaž Hozjan).

http://drugg.fgg.uni-lj.si/5469/

Arhivirano/Archived: 08-04-2016

Univerza
v Ljubljani

Fakulteta za
gradbeništvo in
geodezijo

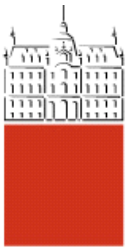

DOKTORSKI ŠTUDIJSKI PROGRAM III. STOPNJE
GRAJENO OKOLJE

Kandidat:
ROBERT PEČENKO

MEHANSKI ODZIV UKRIVLJENIH LESENIH NOSILCEV S SPREMENLJIVO VIŠINO PRI POŽARNI OBTEŽBI

Doktorska disertacija štev: 34/GO

MECHANICAL RESPONSE OF CURVED TIMBER BEAMS WITH VARIABLE HEIGHT UNDER FIRE CONDITIONS

Doctoral thesis No.: 34/GO

Komisija za doktorski študij je na 41. seji, 3. julija 2013, po pooblastilu 30. seje Senata Univerze v Ljubljani z dne 20. januarja 2009, dala soglasje k temi doktorske disertacije.

Za mentorja je bil imenovan doc. dr. Tomaž Hozjan,
za somentorja pa prof. dr. Goran Turk.

Ljubljana, 1. april 2016

Univerza
v Ljubljani

Fakulteta za
gradbeništvo in
geodezijo

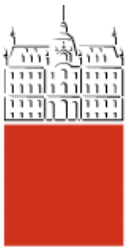

Komisijo za oceno ustreznosti teme doktorske disertacije v sestavi:

- prof. dr. Goran Turk,
- prof. dr. Stojan Petelin, UL FPP,
- izr. prof. dr. Stanislav Srpčič,
- doc. dr. Simon Schnabl,

je imenoval Senat Fakultete za gradbeništvo in geodezijo na 39. seji, 27. marca 2013.

Poročevalce za oceno doktorske disertacije v sestavi:

- izr. prof. dr. Stanislav Srpčič, upok.,
- izr. prof. dr. Simon Schnabl, UL FKKT,
- prof. dr. Staffan Svensson, University of Borås, Švedska,

je imenoval Senat Fakultete za gradbeništvo in geodezijo na 23. seji, 4. novembra 2015.

Komisijo za zagovor doktorske disertacije v sestavi:

- prof. dr. Matjaž Mikoš, dekan UL FGG, predsednik ,
- doc. dr. Tomaž Hozjan, mentor,
- prof. dr. Goran Turk, somentor,
- izr. prof. dr. Stanislav Srpčič, upok.,
- izr. prof. dr. Simon Schnabl, UL FKKT,
- prof. dr. Staffan Svensson, University of Borås, Švedska,

je imenoval Senat Fakultete za gradbeništvo in geodezijo na 26. seji, 24. februarja 2016.

STRAN S POPRAVKI / ERRATA

Stran z napako Page	Vrstica z napako Line	Namesto Error	Naj bo Correction

"Blank page"

IZJAVE

Podpisani Robert Pečenko izjavljam, da sem avtor doktorske disertacije z naslovom "Mehanski odziv ukrivljenih lesenih nosilcev s spremenljivo višino pri požarni obtežbi".

Izjavljam, da je elektronska različica disertacije enaka tiskani različici, in dovoljujem njeno objavo v digitalnem repozitoriju UL FGG.

STATEMENTS

I, the undersigned Robert Pečenko, hereby declare that I am the author of the PhD thesis entitled "Mechanical response of curved timber beams with variable height under fire conditions"

I declare, that the digital version is identical to the printed one, and allow its publication in the digital repository UL FGG.

Ljubljana, 27.3.2016 Robert Pečenko

"Blank page"

BIBLIOGRAPHIC-DOCUMENTALISTIC INFORMATION AND ABSTRACT

UDC	**624.011.1(043)**
Author:	**Robert Pečenko**
Supervisor:	**assist. prof. Tomaž Hozjan, Ph.D.**
Co-supervisor:	**prof. Goran Turk, Ph.D.**
Title:	**Mechanical response of curved timber beams with variable height under fire conditions**
Document type:	**doctoral dissertation**
Notes:	**121 p., 72 fig., 13 tab., 191 eq., 129 ref.**
Keywords:	**timber beam, fire analysis, coupled heat and moisture transfer, sorption, char formation, reliability analysis**

Abstract

The thesis discusses the behaviour of a curved and tapered timber beam exposed to fire. For this purpose a new three-phase numerical model for the geometrical and material non-linear fire analysis is developed. In the first phase, the development of the gas temperature with time, within the fire compartment is determined. New mathematical and numerical model to determine the coupled heat and moisture transfer in timber exposed to fire is introduced in the second phase. The model accounts for the transfer of bound water, water vapour and air, coupled with the heat transfer. The main novelties of the model are: (i) the bound water transfer is refined by including the Soret effect, (ii) a modified description of sorption applicable for the temperatures above the boiling point of water is given, (iii) a moving boundary surface to prescribe water vapour flux and pressure at the contact between the unburned timber and the char layer is introduced. The system of governing differential equations is solved by the finite element method developed in the Matlab® environment. The basic unknowns of the model are: the temperature, the gas pressure, the water vapour and the bound water concentration. After validating the model and conducting parametric studies, the following conclusions can be given: (i) the model accurately predicts both the temperature field and the charring depth, (ii) the higher initial moisture content results in a slower development of temperatures, (iii) a significant effect of bound water diffusion on the total moisture content is shown and (iv) the influence of the convective heat transfer on the temperature distribution is negligible. In the third phase, a mechanical model to determine the stress–strain state of a curved and tapered timber beam exposed to fire is presented. The Reissner geometrically exact planar beam model is employed. Membrane, shear and flexural deformations of the beam are accounted for. The finite element method is used to solve the system of the governing non-linear equations. By validating and verifying the model it can be concluded that the model is very accurate and therefore suitable for the fire analysis of a curved and tapered timber beam. Beside the three-phase numerical model, the thesis also extensively discusses the methodology for estimating reliability of a timber beam exposed to fire, thus giving a firm basis for the modern performance based approach aiming at introducing uncertainties in the fire analysis.

"Blank page"

BIBLIOGRAFSKO-DOKUMENTACIJSKA STRAN IN IZVLEČEK

UDK	**624.011.1(043)**
Avtor:	**Robert Pečenko**
Mentor:	**doc. dr. Tomaž Hozjan**
Somentor:	**prof. Goran Turk**
Naslov:	**Mehanski odziv ukrivljenih lesenih nosilcev s spremenljivo višino pri požarni obtežbi.**
Tip dokumenta:	**doktorska disertacija**
Obseg in oprema:	**121 str., 72 sl., 13 pregl., 191 en., 129 vir.**
Ključne besede:	**lesen nosilec, požarna analiza, model povezanega prenosa toplote in vlage, sorpcija, razvoj zoglenele plasti, analiza zanesljivosti**

Izvleček

V doktorski disertaciji je obravnavano obnašanje ukrivljenega nosilca s spremenljivo višino izpostavljenega požaru. V ta namen je bil razvit nov tri-fazni numerični model za geometrijsko in materialno nelinearno požarno analizo. V prvi fazi je določen časovni razvoj temperatur znotraj požarnega sektorja. V drugi fazi, ki predstavlja glavno temo te disertacije, je bil razvit nov matematični in numerični model za določitev povezanega prehoda toplote in vlage po lesu med požarom. Model upošteva prenos vezane vode, vodne pare in zraka ob hkratnem prenosu toplote. Glavne novosti modela so naslednje: (i) prenos vezane vode je izpopolnjen in vključuje Soretov efekt, (ii) podan je modificiran zapis sorpcije, primeren tudi za temperature nad točko vrelišča, (iii) vpeljana je premikajoča se robna ploskev na stiku med nepoškodovanim lesom in zoglenelo plastjo, kjer sta predpisana tok vodne pare in pritisk. Sistem osnovnih enačb je rešen z metodo končnih elementov v programskem okolju Matlab®. Osnovne neznanke modela so: temperatura, tlak plinske mešanice ter koncentracija vodne pare in vezane vode v lesu. Z validacijo modela in ob upoštevanju parametričnih študij je ugotovljeno naslednje: (i) model omogoča natančno določitev temperaturnega polja in debeline zoglenele plasti, (ii) višja začetna vlažnost lesa vodi v počasnejši razvoj temperatur, (iii) odkrit je bil velik vpliv difuzije vezane vode glede na skupno vsebnost vlage lesa in (iv) vpliv konvekcijskega prenosa toplote na razvoj temperatur je zanemarljiv. V zadnji fazi je predstavljen mehanski model za določitev napetostno-deformacijskega stanja ukrivljenega nosilca in nosilca s spremenljivo višino med požarom. Model je formuliran na podlagi Reissnerjevega geometrijsko točnega modela ravninskega nosilca in zajema vpliv membranske, strižne in upogibne deformacije. Sistem osnovnih enačb je rešen z metodo končnih elementov. Z validacijo in verifikacijo modela je bilo ugotovljeno, da je model zelo natančen in kot tak primeren za požarno analizo omenjenih tipov nosilcev. Poleg tri-faznega numeričnega modela, disertacija prikazuje tudi metodologijo za določitev zanesljivosti lesenega nosilca med požarom, s čimer je prikazan performančni pristop za implementacijo negotovosti v požarno analizo.

“Blank page”

ZAHVALA

Iskreno se zahvaljujem doc. dr. Tomažu Hozjanu, ob katerem sem se naučil pomembnega načela: "*Do or do not. There is no try.*"~Yoda. Hvaležen sem za vso pomoč, vodenje in nasvete pri nastajanju doktorske disertacije, za nepozabna druženja na COST sestankih in mednarodnih konferencah, za vse prekolesarjene klance ter seveda za vse ostale izven-službene dogodivščine.

Za vso pomoč in nasvete, v trenutkih ko sem to najbolj potreboval, se iskreno zahvaljujemo tudi somentorju prof. dr. Goranu Turku.

Da je delo potekalo v mirnem okolju se zahvaljujem bivšemu ter sedanjemu predstojniku UL FGG Katedre za mehaniko, prof. dr. Miranu Sajetu ter prof. dr Igorju Planincu. Hvala tudi vsem ostalim sodelavcem s Katedre za mehaniko za izjemno vzdušje v pisarni ter tudi izven nje.

Za zanimivo izkušnjo s študijem ter raziskovanjem v tujini se iskreno zahvaljujem prof. dr. Staffan Svenssonu.

Hvala Javni agenciji za raziskovalno dejavnost Republike Slovenije za dodeljena finančna sredstva za podiplomski študij.

Hvala staršema za vso podporo v težkih trenutkih, ki so nastopili med nastajanjem naloge. Hvala tudi sestri z družino. Hvala Niki in Eneju, da sem ponovno zbudil otroka v sebi.

Nuša, hvala za razumevanje in ljubezen.

Hvala prijateljem, plezalni druščini ter vsem ostalim za vsa druženja, zanimive debate in vse ostale "neumnosti" tekom študija.

Nenazadnje pa bi se zahvalil tudi Egonu, da je bil za celotno obdobje študija relativno priden.

“Blank page”

TABLE OF CONTENTS

LIST OF FIGURES

LIST OF TABLES

KAZALO SLIK

KAZALO PREGLEDNIC

"Blank page"

1 INTRODUCTION

Timber is one of the oldest known building materials. At first it was probably used as a shelter against natural phenomena and only later on has developed into an advanced engineering material. The reason for its wide use lies in a number of its favourable characteristics. Wood is known for a high strength-to-weight ratio and is capable of withstanding equally well both tension and compression forces, which makes it an ideal material for flexural members. Further on, it is environmentally friendly and low energy is required for its production. In recent decades, its advantages compared to other materials also arise from its potential for the continuous and sustainable supply.

In civil engineering, different applications of timber as the primary supporting system can be found. In general, two of them stand out, i.e. lightweight and large-scaled timber systems. The latter are commonly installed as bearing elements in large buildings, especially in a roof or bridge construction. However, since the maximum cross-section dimension of solid sawn timber is limited to roughly 30 cm, in general even less, special techniques are required to overcome larger spans. One example is the production of a glued laminated timber (glulam), manufactured from timber lamellas glued on top of each other, thus forming members with large cross-sectional dimensions. By bending lamellas prior to being glued together, curved members can also be created. The maximum span of typical representatives of large scaled timber systems, i.e. tapered and curved timber beam, varies from 30 up to 100 m [1]. Such beams are commonly found in sport halls (Fig. 1.1), railway and bus stations, industrial objects, etc.

Figure 1.1: Glulam arch roof in the Richmond Olympic hall [2].
Slika 1.1: Streha iz ukrivljnih lepljenih nosilcev v Richmond Olympic dvorani [2].

Fire represents a destructive force that may result in casualties and extensive damage. Therefore, fire safety is one of the essential requirements that every building must meet. To ensure the acceptable level of fire safety, different precautions can be introduced. Provision of alarm and smoke control system, sprinkler system, access routes for external fire fighting and other rescue teams, are part of the active measures. On the other hand, appropriate compartment formation, provision of fixed escape routes and adequate structural performance are recognised as passive measures. The thesis discusses the latter, since it is primarily focused on the determination of the structural response during fire. There are two different approaches used for this purpose: prescriptive and performance-based approach. The prescriptive approach follows the rules based on the experiences of the structural responses from past fire accidents. A prescriptive code determines how the building has to be constructed in order to achieve the required degree of fire safety. The measures are usually given in standards or technical guidelines. This approach is still the most commonly applied in practice, mainly due to its ease of implementation. However, the prescriptive approach is often regarded as too conservative, uneconomical and in some cases also unsafe. What is more, it is not even required from the engineer to understand the structural behaviour during fire. The desire for a better knowledge of the structural response in fire gave birth to a new branch, performance-based approach. This approach provides an excellent potential to improve structural fire safety design in terms of reducing construction costs and improving the structural safety. The determination of structural response with the perfomance-based approach is usually, due to its complexity, divided in three general steps. Firstly, fire behaviour is determined, followed by the heat transfer analysis as a tool to determine temperature distribution in the structure, and last, the thermo-mechanical analysis of structure to determine its fire resistance.

1.1 State of the art

Compared to other structural materials, large scaled timber members are known for their good fire resistance. In many cases it has been reported that timber members remained practically undamaged and undeformed after severe fires and were rapidly renovated and ready for reuse [3]. The reason for a good fire behaviour of timber lies in the physical and chemical composition of wood. When exposed to fire, at a temperature around 300 °C the wood surface ignites and burns immediately. The burned wood, also recognized as charcoal, acts as a protection layer for the unburned wood underneath the charcoal. In combination with the lack of oxygen underneath the charcoal, the burning rate (charring rate) of the unburned wood underneath the charcoal decreases to a slower steady rate which is maintained during fire exposure. The temperatures on the char surface reach the fire compartment temperatures. However, due to the low thermal conductivity of the charcoal, a steep temperature decrease occurs inside the member. Under the char layer, the zone of the heated timber with the thickness only about 35 mm is found [4]. In the part of this zone where temperatures exceeds 200 °C, wood is subjected to the thermo-chemical decomposition in the absence of oxygen, followed by a weight loss. This process is know as the pyrolysis. Due to the decomposition of wood fibres in the pyrolysis zone the strength of wood significantly decreases. Nonetheless, the pyrolysis zone is commonly very thin compared to the cross-section dimensions of the member. Therefore, wood in the inner core of the member remains intact and provides good load-bearing capacity.

When analysing timber structures during fire, a complex thermal analysis is inevitable. A straightforward

way is to consider timber as solid material and therefore to account only for the transfer of heat by conduction. However, timber is a porous material, since it is composed of cell walls and lumens. Within the cell wall, the presence of bound water is observed, while water vapour and air are found in the lumens. Thus, heat transfer by conduction is accompanied by the transfer of heat by convection and thermophoresis. In addition, timber dries at elevated temperatures, meaning that moisture changes its phase from bound water to water vapour. Such a phase change requires energy, which results in a slower temperature increase inside a member. Therefore, it is obvious that coupling between heat and moisture needs to be considered in an advanced model of timber structures exposed to fire. In the early stages of the research, in the 1960s, a simplified description of the coupled heat and moisture problem was proposed by Luikov [5]. The transport of moisture was simplified into one non-linear partial differential equation for mass conservation. Since then, many models have been based on this approach [6–11]. More advanced models were derived in the 1990s, describing moisture transport for each water phase separately. These models were established mainly with the purpose to simulate the drying of wood. Di Blasi [12] simulated the multi-phase moisture transfer during high-temperature drying of wood particles. The model accounted for the convective and diffusive transport of gas (vapour and air), capillary water convection in the pores and bound water diffusion in the solid wood. In addition, latent heat of evaporation due to the phase change between free water and vapour was taken into account. A similar model was developed by Johansson et al. [13], where convective drying of wood with super heated steam was considered. A comprehensive 2D and 3D drying model was developed by Perré et al. [14, 15]. Nijdam [16] established a high-temperature drying model especially for softwood timber. Despite all the complexities of the described models, none of them accounts for the charring and the pyrolysis. In this field, many empirical models based on experimental results can be found. Eurocode [17] offers constant charring rates β_0 and β_n for different wood species. Constant charring rates were also proposed by several other researchers [18–20]. Contrary to the empirical models, the tendency of research nowadays is the numerical modelling of the pyrolysis and charring. Lautenberger and Fernandez-Pello presented a generalized pyrolysis model for combustible solids [21]. Their work was further extended to the oxidative pyrolysis of wood [22]. The most advanced work was developed by Turner et al. [23], DiBlasi [24] and Park et al. [25], where the formation of gases, tar and char during the wood pyrolysis was included in a coupled heat and moisture transfer model.

Recently, many numerical and experimental studies can be found in the research area of the mechanical behaviour of timber members in fire. Many researchers are still engaged in standard fire tests. Frangi et al. [26, 27] provided experimental research on the cross-laminated and hollow-core timber slab. Experimental investigation of the behaviour of a straight glulam was carried out by Yang et al. [28]. Zhang et al. [29] conducted an experimental and numerical study on a straight timber beam. A simplified heat transfer analysis was considered and, as reported, this was the main reason for the poor agreement between the calculated and the measured quantities. Although standard fire tests are of great importance to determine the nominal fire resistance, they do not give a sufficient insight into the behaviour of a member during a real fire. This can only be achieved if the effect of a real, natural fire inside a fire compartment is investigated. Some recent research can be found in Lennon et al. [30] where the effect of a natural fire on a protected timber floor systems was investigated. The main objective was to determine the mode of failure of different floor systems. Another research was provided by Kolaitis et al. [31], where a full-scale natural fire test was conducted in order to analyse the influence of fire protection cladding on the

behaviour of a timber frame and a cross-laminated timber slab. The coupling effect of heat and moisture transfer in the comprehensive analysis of a timber member was studied by Zhu and Kaliske [32]. They analysed the stress distribution during drying of a long wood board, in ambient temperatures up to 60 °C. The Luikov approach was adopted to determine the temperature and moisture distribution within the wooden board. The effects of the elastic, plastic and mechano-sorptive strain as well as the thermal and hygro expansions were considered in the analysis. A related study was performed by Zhou et al. [33], where the behaviour of a curved glulam beam exposed to changing environmental conditions was investigated. The heat and moisture transfer was modelled by the Fourier and Fick's law. The mechanical model accounted for the elasic strain, thermal and moisture induced strain, mechano-sorptive strain and creep strain. The theory and numerical method were incorporated in the ABAQUS software, where a 3D model was employed. The development of the beam midspan deflection and the distribution of stresses perpendicular to the grain with time were investigated in their study.

In the research group Chair of Mechanics, Faculty of Civil and Geodetic Engineering, University of Ljubljana, the first work dealing with coupled heat and moisture problem was the graduation thesis by Gams [34]. The coupled heat and moisture problem through porous medium was modelled by Luik's equations [5]. The solution was obtained by the finite difference method. This work continued in the doctoral thesis of Schnabl [11], where Luik's equations were embedded in the coupled heat and moisture analysis of a composite beam in fire. The recent works in this field are the doctoral theses of Hozjan [35] and Kolšek [36]. They modelled the coupled heat and moisture transfer through concrete in case of fire. Their models were a combination of the formulations proposed by Tenchev et al. [37] and Davie el al. [38], which, unlike Luik's model, take into account the multiphase moisture transfer through concrete. The first research that focused on the numerical modelling of timber elements exposed to fire was performed by Schnabl [11]. A numerical model of multi-layered composite beams with interlayer slip, shear deformation and charring of timber, exposed to mechanical and fire load, was presented. In the model, the strain based finite element was considered [39], based on the Reissner geometrically exact model of a planar beam. Later on, Schnabl expanded the model to be applicable for the buckling analysis of timber columns exposed to fire [40]. An interesting research was conducted by Srpčič et al. [41]. They carried out a mechanical analysis of glulam beams while changing relative humidity of surrounding air.

The literature overview reveals the lack of research in the area of large-scale timber members exposed to fire; in particular, advanced and comprehensive models for the analysis of timber members exposed to natural fire are missing. In addition, when modelling heat transfer, the majority of the researchers adopt the simplified approach based on the Fourier partial differential equation. The simplified thermal model can account for only one moisture state of timber and gives acceptable results with 12 % of the initial moisture content of timber [42]. However, in an everyday use, timber with different levels of the initial moisture content can be found. In cases when the inital moisture content of timber was not 12 %, an incorrect temperature field in the structure and eventually an inaccurate mechanical behaviour was obtained [29, 43, 44]. This generates a need for advanced thermal modelling of timber exposed to fire. For this reason, the main task of this thesis is to develop an advanced numerical model for the analysis of large-scaled timber members exposed to natural fire with the main emphasis on the coupled heat and moisture transfer model that is capable to predict the temperature, moisture and char depth development and can account for the different initial moisture states of timber.

1.2 Scope of work

The thesis presents new mathematical and numerical model to determine the performance based response of a curved and tapered timber beam simultaneously exposed to mechanical and fire loads. The model is divided in three phases. The first phase deals with the determination of temperatures inside a fire compartment. Two different approaches are introduced. In the first approach, the temperatures are calculated by the standardized time-dependent fire curves. Secondly, performance based approach to model fire behaviour is presented. An advanced computational model based on the computational fluid dynamics is applied. Program package Fire Dynamics Simulator [45] was chosen, which solves the Navier-Stokes equations derived for thermally driven, low speed flow. Since an existing software is adopted, this phase does not represent any novelty. Yet, it represents an important step to implement the performance based approach in fire analysis.

The main subject of the thesis is the second phase of the fire analysis. Here, new mathematical and numerical model for a coupled heat and moisture transfer in timber member exposed to fire is presented. The model accounts for the moisture transport of different water phases observed inside timber accompanied by the transfer of air, both coupled by the heat transfer. Due to porous nature of wood, the transport of bound water, vapour and air takes place along several paths. The transfers of water vapour and air are restricted to the lumens and are described by the convective and diffusive transfer. On the other hand, the bound water transfer takes place inside a cell wall and is described by Fick's law of diffusion, refined to include also the Soret effect. Further on, the model accounts for the coupling between bound water and water vapour, know as sorption. A modified description of sorption suitable for the temperatures above the boiling point of water is incorporated in the model. The heat transfer by conduction is considered, followed by the convective heat transfer of the gaseous mixture. The latent heat due to the phase change from bound water to water vapour is accounted for as well. In addition, the temperature dependent charring is implemented. Since the charring depth increases with fire exposure, the moving boundary surface to prescribe the water vapour flux and the pressure at the contact between the unburned wood and the char layer is introduced. Mathematically, the coupled heat and moisture transfer is described by a system of four non-linear partial differential equations. Since the analytical solution of the system is difficult to obtain, the problem is solved by the finite element method with the Galerkin discretisation [46], where the four–node isoparametric element is used. The basic unknowns of the problem are: temperature, pressure of the gaseous mixture, water vapour concentration and bound water concentration. The software has been developed in the Matlab environment using implicit time discretisation.

In the third phase, the mechanical model used to determine stress-strain state in the curved and tapered timber beam exposed to fire is presented. The formulation of the curved beam is presented in Čas thesis [47]. Here, it is generalized to be applicable for elevated temperatures and modified for tapered beams. The Reissner geometrically exact model of planar beam [48] is used, where the effect of the shear strain is also considered. Further on, the model accounts for the material non-linear [49] and the temperature dependent timber behaviour [17]. The system of generalized equilibrium equations is solved by the finite element method, where the strain-based finite element is employed [39]. The corresponding system of non-linear algebraic equations is solved by the Newton increment-iterative method. A failure occurs when the tangent stiffness matrix of structure becomes singular. This can occur due to the global instability of the structure or due to material failure. The latter occurs when the determinant of the

tangent constitutive matrix of the beam cross-section becomes zero, which indicates that the ultimate bearing capacity of the cross-section has been reached [50].

Beside the three-phase numerical model, the thesis additionally presents an important aspect of the fire safety of timber beam. The methodology for the reliability of a timber beam exposed to fire is demonstrated. The uncertain behaviour of fire, thermal and mechanical properties of wood and the mechanical load are implemented in the fire analysis. Therefore, this part of the thesis presents an important performance-based approach to include the randomness of certain parameters in the fire analysis of timber beam.

The introduction is followed by six chapters. In the second chapter, different approaches to determine gas temperatures within a fire compartment are presented. In the third chapter, the mathematical and numerical model for a coupled heat and moisture transfer for timber exposed to fire is introduced and discussed. The fourth chapter considers the mathematical and numerical mechanical models which serve to determine the stress-strain state of curved and tapered timber beam simultaneously subjected to mechanical and fire loads. The fifth chapter presents the theoretical background for the reliability analysis. The efficiency and applicability of the presented computational models are demonstrated in the sixth chapter. At the end, the thesis conclusions are given.

2 FIRE BEHAVIOUR

Fire is a complex chemical reaction where energy is released in the form of heat. To exist, fire requires three key elements that represent equal sides of what is called “fire triangle”, i.e. fuel, oxygen and heat. For structural fire engineering an assessment of gas temperatures within a fire compartment is required. The assessed temperatures are used as thermal boundary conditions in the next phase of the fire analysis. In general, compartment fires can be described by the different fire phases (Fig. 2.1), i.e. ignition, fire spread/growth, flashover, fully developed fire, post-flashover and fire decay [51, 52].

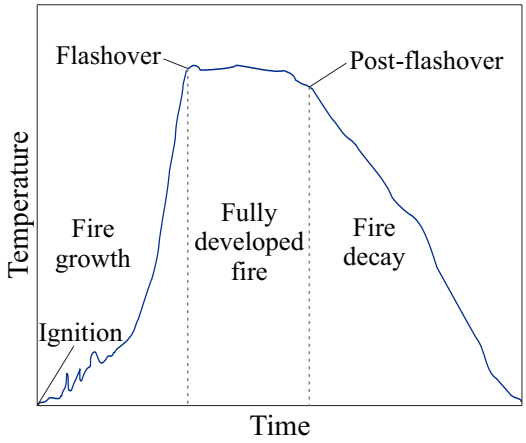

Figure 2.1: Fire phases in compartment fires.
Slika 2.1: Faze požara v požarnem sektorju.

There are different approaches available to determine time-temperature relationship in a fire compartment. The most simple are fire curves that can be found in different standards. More advanced are zone models which are based on the mass and energy conservation in a fire compartment. The most advanced are the computational fluid dynamics models based on the Navier-Stokes equations. For the purposes of this thesis the first and the last approach are applied and briefly presented below.

2.1 Standardized fire curves

Standardized fire curves are most widely used methods of estimating temperatures in compartment fires. The main assumption is that temperature in fire compartment is uniform. The standardized fire curves are divided in two groups: nominal and parametric fire curves.

Nominal fire curves are independent of ventilation and boundary conditions, and were historically developed for fire resistance furnace tests of building materials and elements for their classification and verification. The most recognized is the ISO fire curve [53], followed by the hydrocarbon (HC) fire curve and the external fire curve [54], presented in Fig. 2.2.

The parametric fire curves are based on the assumption that the entire fire load burns out. These curves

provide a rather simple design method to approximate fully-developed compartment fire. In general, fire depends on many parameters and is thus hard to describe. The parametric fire curve as given in Eurocode [54] accounts for the most essential parameters and thus enables more realistic description of compartment fire compared to the nominal fire curves. The considered parameters are compartment size, ventilation conditions, thermal properties of compartment walls and ceilings, fire load density and fire growth rate coefficient [55]. In the following subsections the fire curves considered in the parametric studies are concisely presented.

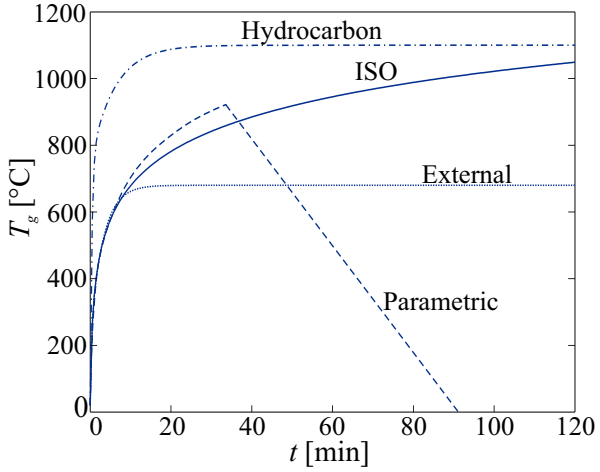

Figure 2.2: Different fire curves given by Eurocode [54].
Slika 2.2: Različne požarne krivulje, ki ji predlaga Evrokod [54].

2.1.1 Standard ISO fire curve

Standard fire curve [53] represents fully developed compartment fire in case of cellulose type of fire load. The curve is defined by the following expression:

$$T_g = 20 + 345\log_{10}(8t+1), \qquad [^\circ\mathrm{C}] \tag{2.1}$$

where T_g is the gas temperature in the fire compartment and t is time in minutes.

2.1.2 Parametric fire curve

Parametric fire curve [54], as a simplified model of natural fire, represents the gas temperature in fire compartment determined on the basis of physical parameters. It is valid for fire compartment floor area up to 500 m^2, without an opening in the ceiling and with a maximum sector height of 4 m. It is further assumed that the fire load of the sector burns out entirely. Parametric fire curve in the heating phase is given as:

$$T_\mathrm{g} = 20 + 1325\left(1 - 0.324e^{-0.2t^*} - 0.204e^{-1.7t^*} - 0.427e^{-19t^*}\right), \tag{2.2}$$

and

$$t^* = t\,\Gamma, \tag{2.3}$$

where T_g is gas temperature in fire compartment in °C, t is time in hours and Γ is time factor function of opening factor O and thermal absorptivity b, determined as:

$$\Gamma = \frac{\left(\frac{O}{b}\right)^2}{\left(\frac{0.04}{1160}\right)^2}, \tag{2.4}$$

where the opening factor and thermal absorptivity are:

$$O = A_v \frac{\sqrt{h_{eq}}}{A_t}, \qquad 0.02 \leq O \leq 0.2 \text{ m}^{1/2}, \tag{2.5}$$

$$b = \sqrt{\rho c \lambda}, \qquad 100 \leq b \leq 2000 \text{ J/m}^2\text{s}^{1/2}\text{K}. \tag{2.6}$$

Here, A_v is the total area of vertical openings in walls, A_t is the total area of enclosure, ρ, c, λ are density, specific heat and thermal conductivity of boundary enclosure, respectively, and finally, h_{eq} is weighted average of window heights on all walls, defined as:

$$h_{eq} = \frac{\sum_i A_{v,i} h_i}{A_v}, \tag{2.7}$$

where $A_{v,i}$ is area and h_i height of window i.

The maximum gas temperature T_{max} in the heating phase occurs at time $t = t_{max}$:

$$t_{max} = \max \left\{ \begin{array}{c} 0.0002 \, \frac{q_{t,d}}{O} \\ t_{lim} \end{array} \right\} \tag{2.8}$$

where t_{lim} is time given in hours. If time t_{max} is equal to t_{lim}, then the fire is fuel controlled, otherwise the fire is ventilation controlled. The term $q_{t,d}$ in expression (2.8) denotes the design value of the fire load correlated to the total surface area of enclosure A_t, written as:

$$q_{t,d} = q_{f,d} \frac{A_f}{A_t}, \tag{2.9}$$

where $q_{f,d}$ is the design value of fire load density associated with the floor area of fire compartment A_f.

Parameter t_{lim} depends on the fire growth rate:

$$t_{lim} = \left\{ \begin{array}{l} 25 \text{ min for slow fire growth rate,} \\ 20 \text{ min for medium fire growth rate,} \\ 15 \text{ min for fast fire growth rate.} \end{array} \right. \tag{2.10}$$

In case when $t_{max} = t_{lim}$, time t^* in Eq. (2.2) is replaced by $t^* = t \, \Gamma_{lim}$, where:

$$\Gamma_{lim} = \frac{\left(\frac{O_{lim}}{b}\right)^2}{\left(\frac{0.04}{1160}\right)^2}, \tag{2.11}$$

and

$$O_{lim} = 0.0002 \frac{q_{t,d}}{t_{lim}}. \tag{2.12}$$

Parametric fire curve in the cooling phase is given as:

$$T_{\mathrm{g}} = \begin{cases} T_{\max} - 625(t^* - t^*_{\max}\, x), & t^*_{\max} \leq 0.5, \\ T_{\max} - 250(3 - t^*_{\max})(t^* - t^*_{\max}\, x), & 0.5 < t^*_{\max} < 2, \\ T_{\max} - 250(t^* - t^*_{\max}\, x), & t^*_{\max} \geq 2. \end{cases} \tag{2.13}$$

where

$$t^*_{\max} = 0.0002 \frac{q_{\mathrm{t,d}}}{O} \Gamma, \tag{2.14}$$

$$x = \begin{cases} 1, & \text{for } t_{\max} > t_{\lim}, \\ t_{\lim} \dfrac{\Gamma}{t^*_{\max}}, & \text{for } t_{\max} = t_{\lim}. \end{cases} \tag{2.15}$$

2.2 Computational fluid dynamics

The CFD models are formed on the theory of fluid dynamics where the behaviour of fire is described by a system of partial differential equations which can be solved analytically only for special cases. More generally, approximate numerical solution of the problem can be obtained where a different discretisation method to approximate differential equations with a system of algebraic equations is applied. The approximations are then employed in small discrete domains where the solution is obtained. Despite approximations, solving problems of fluid dynamics still requires high computational effort. For this reason, the application of CFD methods has spread in just recent decades, with the development of computer hardware and software. In the thesis, advanced program package for the accurate prediction of fire behaviour, i.e. Fire Dynamics Simulator [45] is chosen.

2.2.1 Fire dynamics simulator (FDS)

Fire dynamics simulator, FDS [45], is a numerical model which solves Navier-Stokes equations suitable for thermally driven, low speed flow. In the model, the turbulent flows are considered by two different approaches. The most accurate approach, the direct numerical simulation (DNS), solves the Navier-Stokes equations without averaging or approximating the turbulent flows. The results of a DNS carry detailed information about the flow, since all the motions involved in the flow are determined, such as the velocity, pressure, kinetic energy, and other variables of interest at a large number of mesh grid points. The detailed results lead to better understanding of the flow physics. Nonetheless, the DNS is usually too expensive to be employed, and, as such, inappropriate as design tool. Turbulent flows accommodate an extensive range of length and time scales. Therefore, a large range of eddy sizes can be found in a flow (Fig. 2.3a). Generally, energy is transported by large scale motions, making them the governing transporters of the conserved properties. Small scale motions are weaker and their contribution to the transport of these properties is insignificant. For this reason, the default mode of operation to model turbulent flow in the FDS is the Large Eddy Simulation (LES), where only large eddies are considered and the turbulence is modelled by the Smagorinsky form. The main advantage of the LES is significantly reduced computational time compared to the DNS [56], while the acceptable accuracy of the results is preserved. The flow velocity calculated with different turbulent models is presented in Fig. 2.3.

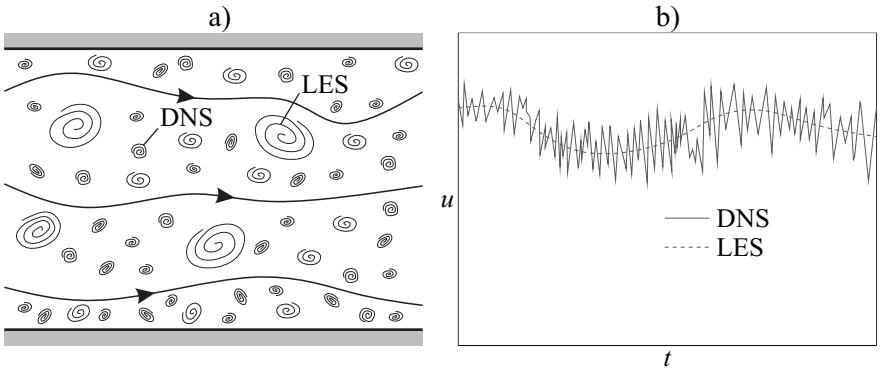

Figure 2.3: a) Turbulent motion - schematic representation [57]. b) Time dependent flow velocity in a chosen point [57].
Slika 2.3: a) Turbulentno gibanje - shematični prikaz [57]. b) Časovno odvisna hitrost toka v izbrani točki [57].

The combustion model in the FDS is based on the mixture fraction concept. Mixture fraction is regarded as conserved scalar quantity defined as the fraction of gas at an observed point in the flow field that originates as a fuel. The reaction between fuel and oxygen is not necessarily instantaneous and complete, meaning that the degree of combustion in under-ventilated fire can be predicted with several optional schemes [56].

The radiative heat transfer in the FDS is considered with the radiative transport equation for the gray gas. The gray gas model uses the average absorption coefficient across the entire spectrum of the gray gas. With the purpose to provide a better spectral accuracy, the wide band model is introduced in order to divide the spectrum to different number of spectral bands. For each band different absorption coefficients are considered [58, 59]. The radiative transport equations are solved by the finite volume method, where, to obtain the discretized form of the radiative transport equations, the unit sphere is divided to a finite number of solid angles. Usually, around 100 discrete angles are applied, which occupy approximately 20% of the total CPU calculation time. This represents a modest cost considering the complexity of the radiative heat transfer.

To approximate differential equations, the FDS uses finite difference method where the calculation domain can be discretized on only rectilinear grid (three-dimensional). Disadvantage is the limitation of the geometry on the rectangular shapes. However, such an approach results in a significant calculation efficiency [56].

2.2.1.1 Modelling fire

When designing fire scenario, first the source of fire and the amount of released heat during fire should be specified. There are several approaches to model the ignition of elements that dictates the fire development in a fire compartment. The most realistic one is to model the ignition and burning of elements with the pyrolysis model. However, the FDS simulations are extremely sensitive to the large number of combustible components and large number of parameters associated with the pyrolysis reaction. Quite often, these parameters cannot be found directly in literature and therefore have to be determined exper-

imentally, which makes the approach impractical and time consuming. Consequently, simpler approach is commonly applied in the form of prescribed heat release rate (*HRR*) for each burning element in fire compartment, together with the corresponding ignition time based on the ignition temperature. It is shown in [60] that this approach is sufficiently accurate for the determination of structural fire resistance. However, the designed fire scenario can be simplified even more by introducing “vent" element. This element is used to apply a particular boundary condition on a solid surface. Therefore, the *HRR* of all burning elements in fire compartment can be prescribed on one or more “vent" elements. In the thesis, the *HRR* of all burning elements in the fire compartment is defined by the idealised and designed *HRR* proposed by Eurocode [54], which can be described by the following parameters:

- $RHR_{\mathrm{f}}\left[\mathrm{kW/m^2}\right]$ - is the maximum rate of heat release per square meter,
- $q_{\mathrm{f,d}}\left[\mathrm{MJ/m^2}\right]$ - is design fire load density related to floor area A_{fi},
- $A_{\mathrm{fi}}\left[\mathrm{m^2}\right]$ - is maximum fire area; in the case of uniformly distributed fire load it is equal to the floor area of the fire compartment, in the case of localised fire it is smaller than the floor area of the fire compartment,
- $t_\alpha\,[\mathrm{s}]$ - is fire growth rate coefficient, which declares the time needed to reach heat release rate of 1 MW.

According to Eurocode, the design fire load density $q_{\mathrm{f,d}}$ is defined as:

$$q_{\mathrm{f,d}} = q_{\mathrm{f,k}} m \delta_{q1} \delta_{q2} \delta_n, \tag{2.16}$$

where m is the combustion factor, δ_{q1} and δ_{q2} are the factors that account for the fire activation risk due to the size and type of the occupancy of the fire compartment, δ_n is a factor that accounts for the different fire fighting measures and $q_{\mathrm{f,k}}$ is the characteristic fire load density per unit floor area. In general, parameters $q_{\mathrm{f,k}}$, RHR_{f} and t_α depend on the amount, arrangement and type of fire load, geometry of the fire compartment and ventilation condition within it. However, Eurocode [54] uses a simpler approach, where these parameters depend only on the occupancy of the building and are given in Table 2.1.

Determination of times t_1, t_2 and t_3 is presented below. Time t_1 and total heat released in the fire growth phase Q_1 are determined as:

$$t_1 = t_\alpha \sqrt{HRR_{\mathrm{max}}}, \tag{2.17}$$

where

$$HRR_{\mathrm{max}} = RHR_{\mathrm{f}} A_{\mathrm{fi}}, \quad [\mathrm{MW}] \tag{2.18}$$

and

$$Q_1 = \int_0^{t_1} HRR\,dt = \frac{1}{3} HRR_{\mathrm{max}} t_1. \tag{2.19}$$

From Fig. 2.4 it can be seen that the total energy released can be calculated as:

$$Q = Q_1 + Q_2 + Q_3 = \int_0^{\infty} HRR\; dt, \quad [\mathrm{MJ}] \tag{2.20}$$

Table 2.1: Characteristic fire load density $q_{f,k}$, fire growth rate t_α and RHR_f for different occupancies.
Preglednica 2.1: Karakteristična gostota požarne obtežbe $q_{f,k}$, stopnja razvoja požara t_α in RHR_f za različne namembnosti stavbe.

Occupancy	$q_{f,k}\left[\mathrm{MJ/m^2}\right]$	t_α	RHR_f
Dwelling	780	300	250
Hospital room	230	300	250
Hotel room	310	300	250
Library	1500	150	500
Office	420	300	250
School classroom	285	300	250
Shopping centre	600	150	250
Cinema	300	150	500
Public transport place	100	600	250

where the total energy released can also be expressed as the product of the design fire load density and the maximum area of fire:

$$Q = q_{f,d} A_{fi}. \tag{2.21}$$

The horizontal plateau, i.e. the phase of fully developed fire, is limited by the decay phase which starts after 70 % of the total energy has been released, thus:

$$Q_3 = 0.3\ Q. \tag{2.22}$$

Time t_2 and energy released in the phase of fully developed fire Q_2 are:

$$Q_2 = HRR_{max}\,(t_2 - t_1) = Q - Q_1 - Q_3 = 0.7\ Q - Q_1. \tag{2.23}$$

$$t_2 = t_1 + \frac{0.7\ Q - Q_1}{HRR_{max}}. \tag{2.24}$$

Finally, time t_3 is determined as:

$$t_3 = t_2 + 2\frac{0.3\ Q}{HRR_{max}}. \tag{2.25}$$

In Fig. 2.4 the idealised *HRR* as proposed by Eurocode [54] is presented.

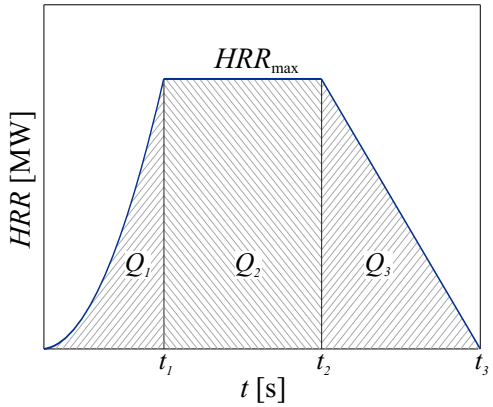

Figure 2.4: Idealised heat release rate [54].
Slika 2.4: Idealizirana hitrost sproščanja toplote [54].

In the thesis, the advanced fire modelling is used as a tool to determine the development of temperatures in fire compartment. For this reason, only the basic principles and methodology are presented. Full description of fire modelling in the FDS software can be found in [60, 61].

3 COUPLED HEAT AND MOISTURE TRANSFER

3.1 Introduction

To understand the behaviour of wood at elevated temperatures, the knowledge about wood structure and chemical composition is needed. The description is limited to softwood, since the vast majority of timber structures are made of softwood. There are four main structural levels of wood to observe: macrostructure, microstructure, ultrastructure and chemical structure. Below all the four levels are described.

Composition of wood seen with a naked eye is identified as the macrostructure (Fig. 3.1a). Tree growth and cell division take place in a layer between the wood and the bark called cambium. This layer is followed by several growth rings which consist of lighter earlywood and darker latewood. The transport of water and minerals in a tree is restricted to the outer zone of growth rings called sapwood. The inner core of the log is recognized as heartwood and is cut off from the transport of water and nutrients.

The microstructure of wood is shown in Fig. 3.1b. The growth ring is composed of longitudinal tubular tracheid cells (Fig. 3.1c). The length of tracheids is about 2.5 to 5 mm, while their width is about hundred times smaller. The cells give structural support to the tree, while the transport of water and nutrients takes place in the empty spaces inside the cell walls (lumens). Earlywood tracheids can be recognised by large

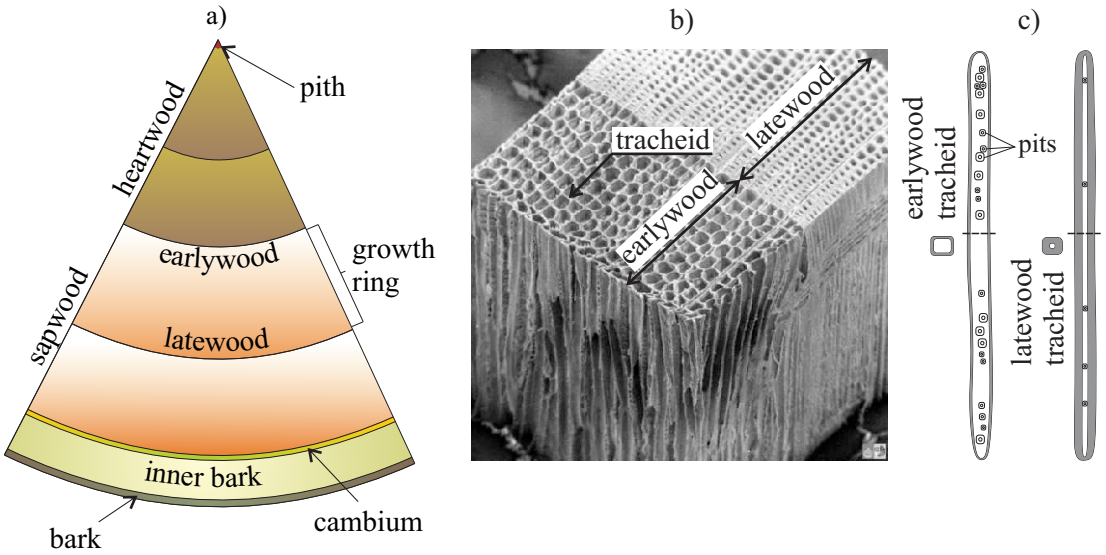

Figure 3.1: a) Wood macrostructure. b) Wood structure under microscope [62]. c) Schematic illustration of tracheids.

Slika 3.1: a) Makroskopska zgradba lesa. b) Struktura lesa vidna pod mikroskopom [62]. c) Shematski prikaz trahednih celic.

lumens and thin cell walls, which allow faster transport of water and nutrients during the tree growth in the spring. Circular openings in the cell wall known as pits enable the transport of water and nutrients from one cell to another. More pits can be found in the earlywood compared to the latewood. The

latewood tracheids are distinguished from the earlywood tracheids by having thicker walls and smaller lumens. They are formed in the summer and autumn and are important for the strength of the tree.

The ultrastructure of a tracheid wall is presented in Fig. 3.2. The cell wall is divided in the primary and secondary cell wall. All the cell wall layers are regarded as composite material with reinforcing microfibrils and a matrix material [63]. The primary wall represents the first layer of the growing cell in the cambium. It is very thin and the microfibrils are randomly and sparsely arranged. The secondary wall is composed of three layers, the outer layer S1, the middle layer S2 and the inner layer S3. The microfibrils in the secondary wall are parallel to each other and closely arranged. In the thickest S2 layer, the microfibrils are oriented in the right-hand spiral with a low microfibrillar angle and therefore provide good tensile and bending behaviour of the cell wall. Microfibrillar angle in S2 layer is the angle between the microfibrils and the longitudinal axis of the cell wall. In Fig. 3.2 the angles can be seen as lines in the different layers of the cell wall. The microfibrils in the S1 and S3 layer are aligned transversely to the cell wall and thus provide torsional and shear stiffness. The molecular composition of wood is presented below.

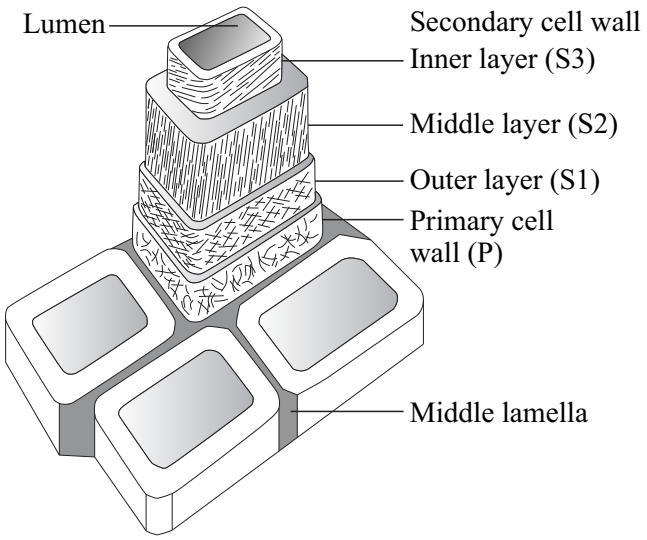

Figure 3.2: Wood ultrastructure [64].
Slika 3.2: Ultraskopska zgradba lesa [64].

Chemically, wood is composed of cellulose, hemicellulose and lignin. Cellulose is a chain composed of glucose units $[C_6H_{10}O_5]_n$ with the degree of polymerisation from 5000 to 10000. Cellulose chains are interconnected by the hydrogen bonds between hydroxyl groups of the glucose units, forming what is called microfibrils. The unbounded hydroxyl groups of the glucose units are recognized as sorption sites where water molecules can bind. Compared to the cellulose, hemicellulose is made of different sugar units and is very hygroscopic. Lignin is the least hygroscopic among the three basic components, due to its different chemical structure. In the absence of oxygen it is resistant to bacterial and fungal decomposition. Lignin found in the cell wall binds with the cellulose and gives stiffness to the cell wall and is also a bonding agent in the middle lamella, cementing together the tracheids.

As presented above, wood is a non-homogeneous, open porous and hygroscopic material. Therefore, the heat and moisture transport in timber exposed to fire represents a complex system of coupled processes.

The transfer of moisture takes place along several transport paths. These are related to the different phases of water observed inside timber. In the case of structural timber, wood fibres are usually below saturation point and therefore only bound water and water vapour are present. Water vapour transfer is restricted to the lumens, whereas the bound water transfer takes place inside the cell wall. Mass transfers can be described by different physical processes, usually by the transfer of water phase by diffusion and/or by convection. Mass diffusion in a mixture of two or more phases (gases and liquids) occurs when a concentration gradient exists, i.e., when the phases are distributed unevenly. On the other hand, convection is a phenomenon that describes the flow of fluid through porous medium when a pressure gradient is present. The transfer of bound water and water vapour is coupled. The connection arises through the exchange of mass between the phases, known as sorption, i.e., absorption of water into the cell-wall and desorption of bound water to water vapour. The transfer of heat takes place along several transport paths as well. In the cell wall, the heat is transferred by conduction, in the cell lumen convective transfer of gases takes place. Further on, coupling between moisture and heat transfer occurs. When timber is heated, the temperature gradient acts as a driving force for the mass diffusion in the phenomenon called thermophoresis or the Soret effect. Moreover, faster desorption of bound water at elevated temperatures results in the increased concentration of water vapour. Therefore, the pressures inside timber increase, contributing an additional driving force for the convective heat transfer. What is more, due to the phase change from water vapour to bound water (adsorption) or vice versa (desorption), energy is released or required. For instance, when drying, energy is required for bound water desorption, which results in a slower temperature increase.

Wood is also a flammable and combustible material. Exposed to fire or elevated temperatures it is subjected to thermal degradation, called pyrolysis (Fig. 3.3a). Pyrolysis is an extremely complex process. It represents the interaction of various chemical processes with the process of heat and moisture transfer. At a temperature of 200°C the decomposition of the least stable wood components takes place (Fig. 3.3b). More stable components decompose at around 250°C and 350°C and also above 400°C. The result is formation of different gases, resins and acids (carbon dioxide and monoxide, methane, formaldehyde, formic and acetylene acid, tar, etc.). In the temperature range between 270°C and 300°C wood material ignites. Burned wood recognised as charcoal represents an insulation layer for unburned wood for the temperatures up to 500 °C [17]. However, due to the physical and chemical degradation of charcoal, during further temperature increase the charcoal cracks. This leads to the increased heat transfer through the charcoal.

As described, the problem of heat and moisture transfer together with the pyrolysis of timber is a highly complex process. The phenomenon is transient, non-linear and the material properties of separated phases (solid, liquid, gas) are state dependent. Therefore, it is challenging to derive the complete mathematical model based on detailed physical and chemical description of the problem. Certain simplifications are, thus, implemented in the model presented in this thesis. The main simplification is that the the pyrolysis reaction is not considered in the model. Therefore, only temperature dependent charring is included. Since the charring depth increases with the fire exposure, a moving boundary surface to prescribe vapour flux and pressure at the contact between the unburned wood and the char layer is introduced. Beside simplified determination of charring, the coupled heat and moisture transfer model accounts for the advanced description of the transfer of both water phases, bound water and water vapour, accompanied also by the transfer of air. The transfer of air and water vapour is described by the convective and dif-

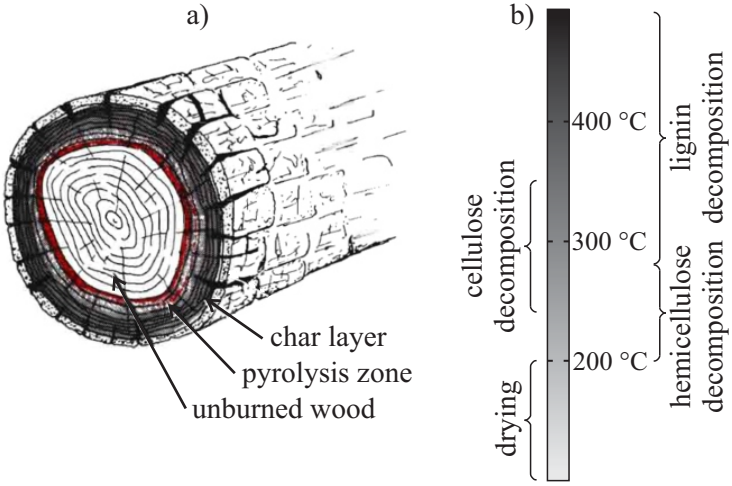

Figure 3.3: a) Pyrolysis of a wooden log [65]. b) Degradation of wood components at elevated temperatures [66].
Slika 3.3: a) Piroliza lesenega debla [65]. b) Degradacija osnovnih komponent lesa pri povišanih temperaturah [66].

fusive transfer. The bound water transfer in the cell wall is defined by the Fick's law, refined to also include the Soret effect. Furthermore, the model accounts for a modified description of sorption suitable for temperatures above the boiling point of water. Beside the conductive heat transfer, the model also considers the convective heat transfer of the gaseous mixture. In addition, the latent heat due to the phase change from bound water to water vapour is accounted for.

3.2 Governing equations

Mathematically, coupled problem of heat and moisture transport is described with a system of continuity equations for mass conservation, supplemented with an equation describing the conservation of enthalpy. In the following parts of this section all the governing equations for the coupled problem are described.

3.2.1 Conservation equations

Mass conservation equations for each phase are:

$$\text{bound water:} \qquad \frac{\partial c_b}{\partial t} + \nabla \cdot \mathbf{J}_b = \dot{c}, \tag{3.1}$$

$$\text{water vapour:} \qquad \frac{\partial \left(\varepsilon_g \widetilde{\rho}_v\right)}{\partial t} + \nabla \cdot \mathbf{J}_v = -\dot{c}, \tag{3.2}$$

$$\text{air:} \qquad \frac{\partial \left(\varepsilon_g \widetilde{\rho}_a\right)}{\partial t} + \nabla \cdot \mathbf{J}_a = 0. \tag{3.3}$$

The concentration of bound water c_b is defined per unit volume of wood. The concentrations of water vapour and dry air, $\widetilde{\rho}_v$ and $\widetilde{\rho}_a$, are defined per unit volume of gaseouse mixture. ε_g is the porosity of wood. Mass fluxes for bound water, water vapour and air, $\mathbf{J}_i$ $(i = b, v, a)$, are defined per unit volume of

wood. $\dot{c}$ is sorption rate which interconnects mass conservation of bound water and water vapour, ∇ is the nabla operator. The enthalpy conservation equation is:

$$\underbrace{\frac{\partial}{\partial t}\left(c_b h_b + \varepsilon_g \widetilde{\rho}_v h_v + \varepsilon_g \widetilde{\rho}_a h_a + \rho_0 h_0\right)}_{a} = \underbrace{-\nabla \cdot (h_b \mathbf{J}_b + h_v \mathbf{J}_v + h_a \mathbf{J}_a)}_{b} + \underbrace{\nabla \cdot (\mathbf{k} \nabla T)}_{c}. \tag{3.4}$$

The change of enthalpy of wood (term a) is balanced by heat conduction (term c) as well as heat convection through mass transport of each medium ($i = b, v, a$) with its enthalpy h_i (term b). The $\mathbf{k}$ matrix contains thermal conductivities for the different wood directions. The density and enthalpy of dry wood are denoted as ρ_0 and h_0, respectively.

3.2.2 Constitutive relations

3.2.2.1 Bound water

Bound water transfer in the cell wall is driven by concentration (∇c_b) and temperature gradients (∇T). Mathematical model for this was proposed in [63] as:

$$\mathbf{J}_b = -\mathbf{D}_b \nabla c_b - \mathbf{D}_{bT} \nabla T. \tag{3.5}$$

In Eq. (3.5), the Soret effect is recognised as the second term on the right side. Matrices $\mathbf{D}_b$ and $\mathbf{D}_{bT}$ contain diffusion coefficients and thermal coupling diffusion coefficients:

$$\mathbf{D}_b = \mathbf{D}_0 \exp\left(-\frac{E_b}{RT}\right), \tag{3.6}$$

$$\mathbf{D}_{bT} = \mathbf{D}_b \frac{c_b E_b}{RT^2}, \tag{3.7}$$

where R is the universal gas constant and $\mathbf{D}_0$ is the diffusivity matrix which contains base values for diffusion coefficients in the different material directions, i.e., longitudinal and transverse (D_L^0 and D_T^0).

Water is bound to wood by hydrogen bonds between water molecules and hydroxyls groups of the wood polymer chains. Energy required to break the hydrogen bond, E_b, is according to [67]:

$$E_b = (38.5 - 29\ m) \cdot 10^3, \tag{3.8}$$

where moisture content m is defined as:

$$m = \frac{c_b}{\rho_0}. \tag{3.9}$$

The increase of diffusion coefficients over base values for diffusion coefficient as a function of moisture content is presented in Fig. 3.4. The results are shown for different temperatures. It can be observed that D_{bT}/D_0 is significantly larger than D_b/D_0 at elevated temperatures ($T > 100°\mathrm{C}$) and at moisture content above 15 %, meaning that bound water flux in this range of temperatures and moisture content is driven mainly by the Soret effect.

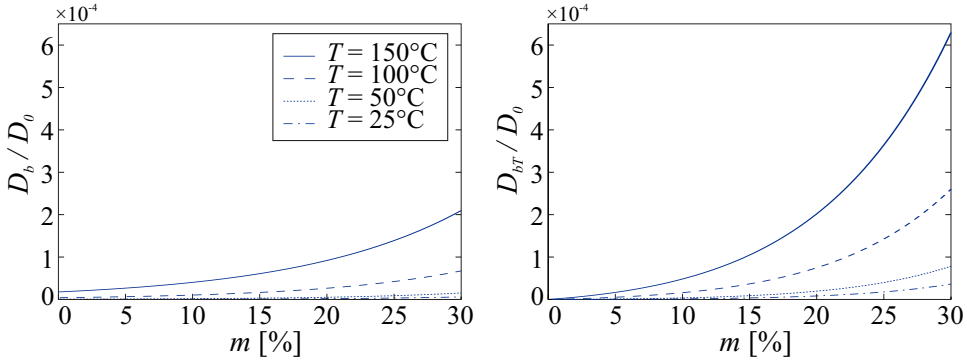

Figure 3.4: Development of D_b/D_0 and D_{bT}/D_0 as a function of moisture content, at different temperatures. ρ_0 = 500 kg/m^3.

Slika 3.4: Razvoj D_b/D_0 in D_{bT}/D_0 v odvisnosti od vsebnosti vlage ter pri različnih temperaturah. ρ_0 = 500 kg/m^3.

3.2.2.2 Water vapour and air

The gaseous mixture inside timber, excluding the products of pyrolysis, is comprised of water vapour and air and is therefore defined as: $\widetilde{\rho}_g = \widetilde{\rho}_v + \widetilde{\rho}_a$. Convection of gas in porous media is driven by pressure gradient, as described by Darcy's law. Furthermore, the diffusion between water vapour and air occurs, which is described by Fick's law. The fluxes of air and water vapour are therefore:

$$\mathbf{J}_a = \varepsilon_g \widetilde{\rho}_a \mathbf{v}_g - \varepsilon_g \widetilde{\rho}_g \mathbf{D}_{av} \nabla \left(\frac{\widetilde{\rho}_a}{\widetilde{\rho}_g} \right), \tag{3.10}$$

$$\mathbf{J}_v = \varepsilon_g \widetilde{\rho}_v \mathbf{v}_g - \varepsilon_g \widetilde{\rho}_g \mathbf{D}_{va} \nabla \left(\frac{\widetilde{\rho}_v}{\widetilde{\rho}_g} \right). \tag{3.11}$$

Following Darcy's law, the velocity of gaseous mixture, $\mathbf{v}_g$, is:

$$\mathbf{v}_g = \frac{\mathbf{K} K_g}{\mu_g} \nabla P_g. \tag{3.12}$$

The $\mathbf{K}$ matrix contains specific permeability of dry wood for different material directions, where K_g is relative permeability of gas in timber, μ_g dynamic viscosity of gas and ∇P_g gas pressure gradient. In accordance with Dalton's law, the pressure of the gaseous mixture is equal to the sum of partial pressure of air and partial pressure of water vapour: $P_g = P_a + P_v$. It is assumed that an ideal gas law can describe the pressures with sufficient accuracy [37]:

$$P_a = R_a \widetilde{\rho}_a T, \tag{3.13}$$

$$P_v = R_v \widetilde{\rho}_v T, \tag{3.14}$$

where R_a and R_v are the gas constants for air and water vapour.

Diffusion coefficient of air into water vapour $\mathbf{D}_{va}$ is identical to the diffusion coefficient of water vapour into air $\mathbf{D}_{av}$. Both are defined as [68]:

$$\mathbf{D}_{va} = \mathbf{D}_{av} = \zeta 1.87 \left(\frac{T^{2.072}}{P_g} \right) \cdot 10^{-5}, \tag{3.15}$$

where $\boldsymbol{\zeta}$ is the material direction dependent reduction factor due to the hindrance of the diffusion in the cellular structure of wood.

3.2.2.3 Enthalpy balance

Expanding the derivatives of terms *a* and *b*, Eq. (3.4) becomes:

$$\begin{aligned}&\frac{\partial h_b}{\partial t}c_b+\frac{\partial h_v}{\partial t}\varepsilon_g\widetilde{\rho}_v+\frac{\partial h_a}{\partial t}\varepsilon_g\widetilde{\rho}_a+\frac{\partial h_0}{\partial t}\rho_0+h_b\frac{\partial c_b}{\partial t}+h_v\frac{\partial \varepsilon_g\widetilde{\rho}_v}{\partial t}+h_a\frac{\partial \varepsilon_g\widetilde{\rho}_a}{\partial t}+\\&+h_b\nabla\cdot\mathbf{J}_b+h_v\nabla\cdot\mathbf{J}_v+h_a\nabla\cdot\mathbf{J}_a+\mathbf{J}_b\cdot\nabla h_b+\mathbf{J}_v\cdot\nabla h_v+\mathbf{J}_a\cdot\nabla h_a=\nabla\cdot(\mathbf{k}\nabla T)\,.\end{aligned}\tag{3.16}$$

Whitaker [69] proposed the enthalpy for the different phases to be a linear function of temperature:

$$h_\alpha=h_\alpha^0+C_\alpha\left(T_\alpha-T_{ref}\right),\tag{3.17}$$

where h_α^0 and C_α are the enthalpy and specific heat capacity of the α component ($\alpha=b,v,a,0$) at the reference temperature T_{ref}. Inserting the mass conservation (Eqs. (3.1)–(3.3)) and temperature dependence of the enthalpy (Eq. (3.17)) into Eq. (3.16), and assuming local thermal equilibrium between the phases ($T_\alpha=T$), Eq. (3.16) yields:

$$\begin{aligned}&\underbrace{\left(\varepsilon_g\widetilde{\rho}_aC_a+\varepsilon_g\widetilde{\rho}_vC_v+c_bC_w+\rho_0C_0\right)}_{\underline{\rho C}}\frac{\partial T}{\partial t}+\underbrace{(h_b-h_v)}_{\Delta H_s}\dot{c}+\\&\qquad(C_b\mathbf{J}_b+C_v\mathbf{J}_v+C_a\mathbf{J}_a)\,\nabla T=\nabla\cdot(\mathbf{k}\nabla T)\,.\end{aligned}\tag{3.18}$$

Here, ΔH_s represents heat of sorption defined as the difference between the enthalpy of bound water and water vapour. Since bound water and water vapour are found in different states, the heat of sorption includes also the latent heat due to the phase change. The enthalpy of bound water is comparable to that of frozen water and has a lower enthalpy than liquid water [70]. Fig. 3.5 presents relative enthalpy levels (REL) of water vapour, liquid water, ice and bound water. Relative liquid water enthalpy Q_l is defined as reference quantity for other RELs, thus $Q_\mathrm{l}=0$. Q_0 is the REL of vaporisation of liquid water, Q_f is the REL of ice, Q_u is the REL of vaporisation of frozen water (sublimation), Q_s is the REL of sorption of liquid water in the wood and Q_v is the REL of vaporisation of bound water [70, 71]. Heat of sorption can be written as $\Delta H_s=Q_0+Q_\mathrm{s}=Q_\mathrm{v}$.

In the literature, [12–14], the contributions of diffusion in $\mathbf{J}_v$ and $\mathbf{J}_a$ (Eqs. (3.10) and (3.11)) are usually neglected from Eq. (3.18). Furthermore, according to the findings in [72], the bound water flux is considerably lower compared to the vapour flux and thus neglected in Eq. (3.18). When accounting for these simplifications, the heat transfer equation takes the following form:

$$\left(\underline{\rho C}\right)\frac{\partial T}{\partial t}=\nabla\cdot(\mathbf{k}\nabla T)-\left(\underline{\rho C\mathbf{v}}\right)\nabla T-\Delta H_s\dot{c},\tag{3.19}$$

where heat convection $\underline{\rho C\mathbf{v}}$ is determined as:

$$\underline{\rho C\mathbf{v}}=\rho_gC_g\mathbf{v}_g=\left(\varepsilon_g\widetilde{\rho}_aC_a+\varepsilon_g\widetilde{\rho}_vC_v\right)\mathbf{v}_g.\tag{3.20}$$

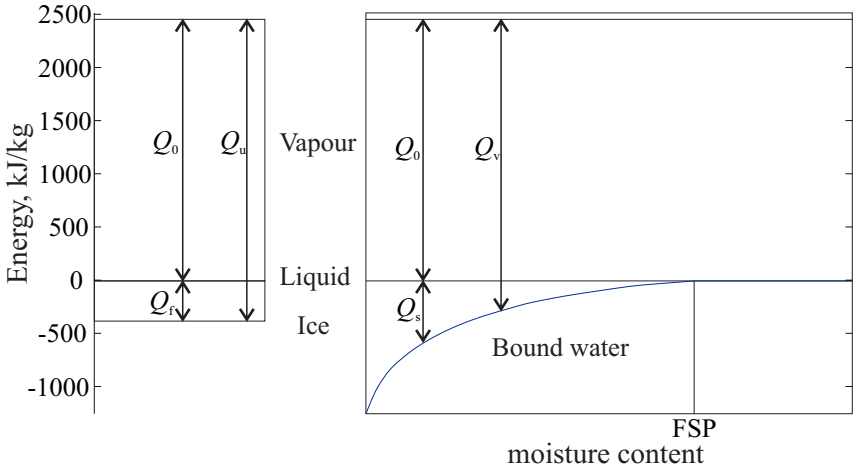

Figure 3.5: Relative enthalpy levels of water vapour, liquid water, ice and bound water as a function of moisture content [70, 71].

Slika 3.5: Relativne entalpije vodne pare, proste vode, ledu in vezane vode kot funkcija vsebnosti vlage [70, 71].

3.2.2.4 Sorption

In everyday use wood is usually subjected to the variations of relative humidity in the ambient air, which causes the increase or decrease in the moisture content, known as adsorption or desorption, respectively. Sorption is a common term associated with absorption and desorption. It is driven by the difference between moisture in the cell wall and moisture in the lumens. Moisture in the cell wall is represented by the bound water, while moisture in the lumens is represented by the water vapour. The equilibrium between the two phases (equilibrium moisture state) is described by the sorption isotherm. Modified formulation for sorption model [73], applicable for temperatures above the pressure dependent boiling point, T_{boil}, is proposed here:

$$\dot{c} = \begin{cases} H_c\,(c_{bl} - c_b)\,, & T \le T_{boil}, \\ H_c\,(0 - c_b)\,, & T > T_{boil}. \end{cases} \tag{3.21}$$

In Eq. (3.21) c_{bl} is the equivalent bound water concentration for a known water vapour pressure P_v at the equilibrium moisture state (Fig. 3.6). According to [73] the reaction rate function H_c is:

$$H_c = \begin{cases} C_1 \exp\left(-C_2 \left(\frac{c_{bl}}{c_b}\right)^{C_3}\right) + C_4, & c_b \le c_{bl}, \\ C_1 \exp\left(-C_2 \left(2 - \frac{c_{bl}}{c_b}\right)^{C_3}\right) + C_4, & c_b > c_{bl}, \end{cases} \tag{3.22}$$

and

$$C_2 = C_{21} \exp\left(C_{22} h\right), \tag{3.23}$$

where C_1 to C_4 are the model parameters [63].

The equilibrium moisture content, EMC, is assumed to follow the Anderson-McCharty sorption isotherm [74] defined as:

$$\mathrm{EMC} = \frac{c_{bl}}{\rho_0} = \frac{\ln(\ln(1/h)/f_1^k)}{f_2^k}. \tag{3.24}$$

Here, h is the relative humidity defined as the ratio between partial pressure of water vapour P_v and saturated vapour pressure P_s at a given temperature. f_i^k are parameters that determine the shape of the adsorption ($k = a$) and desorption ($k = d$) isotherms. They are defined as:

$$f_i^k = \sum_{j=0}^{n} b_{ij}^k T^j, \qquad i \in \{1,2\}. \tag{3.25}$$

Parameters b_{ij} are determined based on the fitting of desorption isotherms measured by Kelsey [75].

Temperature dependency of sorption isotherms is depicted in Fig. 3.6. At the same humidity, the equilibrium moisture content (EMC) is smaller for higher temperatures, meaning that smaller amount of water can bind to wood at higher temperatures.

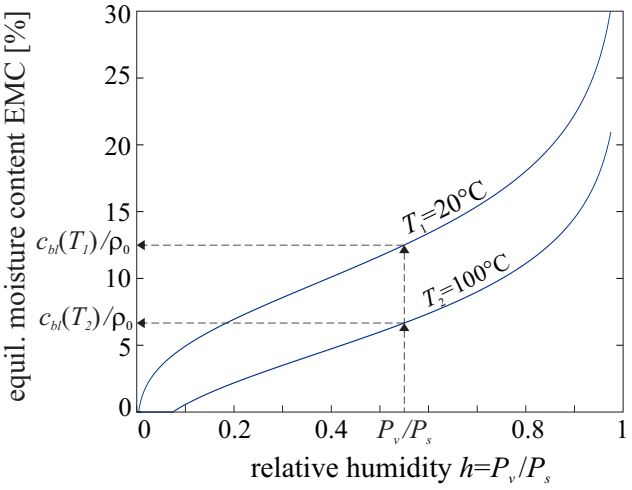

Figure 3.6: Desorption boundary curves based on the Anderson-McCharty model for chosen temperatures. The relation between vapour pressure P_v and equivalent bound water concentration c_{bl} is presented by arrows.

Slika 3.6: Desorpcijska robna krivulja na podlagi Anderson-McCharty modela pri izbranih temperaturah. S puščicami je prikazana zveza med tlakom vodne pare P_v in ekvivalentno koncentracijo vezane vode c_{bl}.

3.2.2.5 Thermal properties of wood and char layer at elevated temperatures

At elevated temperatures, pyrolysis of wood occurs which is followed by the wood fibre decomposition. This results in changed thermal properties of the material. In adition, the charcoal caused by the pyrolysis, exhibits completely different thermal properties compared to the unburned wood. In the presented coupled heat and moisture model, the change of thermal properties of wood is following the

Eurocode [17]. Temperature dependent thermal conductivity of wood and char layer is presented in Fig. 3.7. Significant increase in conductivity above 500 °C is observed. In this way, the increased heat transfer between the ambient and the unburned wood due to shrinkage cracks above this temperature is considered.

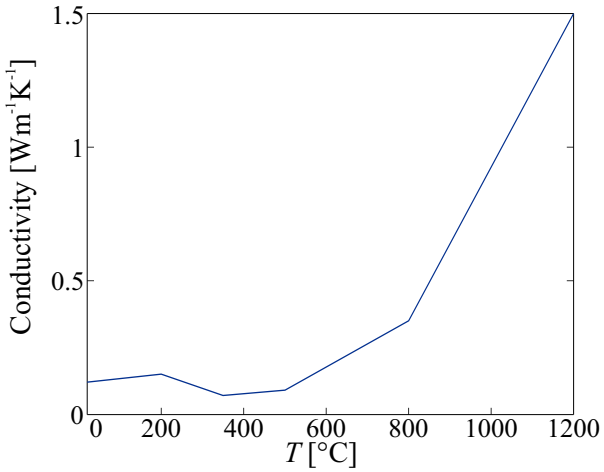

Figure 3.7: Temperature dependent thermal conductivity for wood and char layer in the transverse direction.

Slika 3.7: Temperaturno odvisna toplotna prevodnost lesa in zoglenele plasti v smeri pravokotno na vlakna.

Specific heat of timber as a function of temperature is shown in Fig. 3.8. Specific heat described by the solid line is applied in the presented heat and moisture model. In the case when heat transfer in timber is modelled by the Fourier partial differential equation [76], the specific heat with the increase in temperature range between 100 °C and 120 °C can be considered (dotted line). By doing so, the influence of water evaporation on the temperature development can be accounted for.

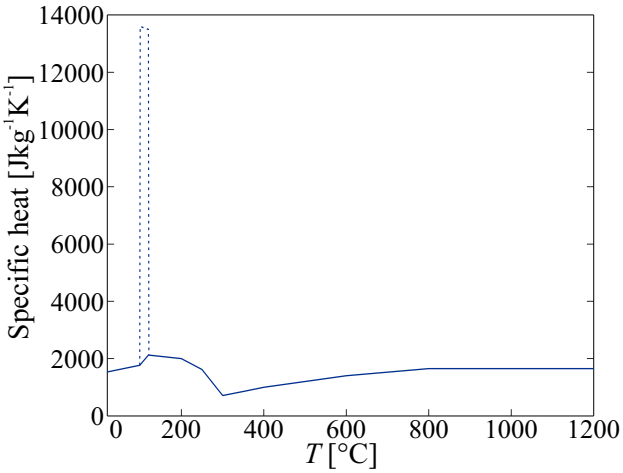

Figure 3.8: Temperature dependent specific heat of timber and char layer.

Slika 3.8: Temperaturno odvisna specifična toplota lesa in zoglenele plasti.

Temperature dependent density ratio of softwood is demonstrated in Fig. 3.9. At 200 °C the thermal

decomposition of wood components begins, which is also accompanied by the mass loss. Therefore, above 200 °C the density ratio starts decreasing.

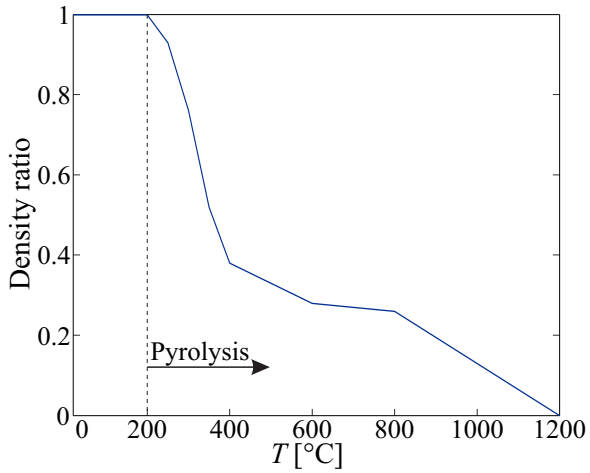

Figure 3.9: Temperature dependent density ratio of softwood.
Slika 3.9: Temperaturno odvisno razmerje gostote za mehki les.

3.2.3 Boundary conditions

It is assumed that at the interface between timber and the surroundings or the char layer the pressure in pores is equal to ambient pressure $P_{g,\infty}$:

$$P_g = P_{g,\infty}. \tag{3.26}$$

Heat exchange between the timber volume and the surroundings is prescribed as heat flux at the boundary surface:

$$h_{cr} = k\frac{\partial T}{\partial n}, \tag{3.27}$$

where $\frac{\partial T}{\partial n}$ represents the derivative of temperature normal to the boundary surface and h_{cr} is heat flux at the boundary surface composed of heat flux due to convection and radiation: $h_{cr} = h_c + h_r$. Heat flux due to convection is determined as:

$$h_c = \alpha_c \left(T_\infty - T_m\right), \tag{3.28}$$

where α_c is the coefficient of heat transfer by convection, T_∞ is ambient temperature and T_m is the surface temperature of timber at the exposed side. Radiative heat flux is calculated according to the Stefan-Boltzmann law:

$$h_r = \sigma \varepsilon_m \varepsilon_f \left(T_\infty^4 - T_m^4\right). \tag{3.29}$$

Here, σ is the Stefan-Boltzmann constant, ε_m is the surface emissivity of timber and ε_f the emissivity of fire. According to [17, 54], $\varepsilon_f = 1$ and $\varepsilon_m = 0.8$.

Water vapour exchange between the water vapour in the pores and the water vapour in the surroundings is described by the water vapour flux through the outer surface or the char layer:

$$\mathbf{n} \cdot \mathbf{J}_v = -k_c \left(\widetilde{\rho}_{v,\infty} - \widetilde{\rho}_v \right), \tag{3.30}$$

where $\widetilde{\rho}_{v,\infty}$ is water vapour concentration in ambient, $\mathbf{n}$ is a unit vector normal to the outer surface of timber or char layer and k_c is mass transfer coefficient determined by [68], where the Chilton-Coldburn analogy is suggested, which couples heat and mass transfer coefficients as:

$$k_c = \frac{\alpha_c}{\widetilde{\rho}_a C_a} \left(\frac{D_{av}}{\alpha_{air}} \right)^{2/3}, \tag{3.31}$$

where α_{air} is thermal diffusivity of air.

The bound water is restricted to the wood cell wall and is only exchanged by sorption. Therefore, the Neumann boundary condition on the surface is applied, accordingly:

$$\mathbf{n} \cdot \mathbf{J}_b = 0. \tag{3.32}$$

3.3 Charring of wood

In the present model, charring occurs when the average finite element temperature $T_{\text{av,el}}$ exceeds the charring front temperature T_{char}. $T_{\text{av,el}}$ is determined as the average of temperatures in the finite element integration points (Gaussian points). For fires with the growth rate similar to standard ISO fire, the charring temperature is assumed to be 300°C [17]. In the char layer only heat transfer is assumed. Thermal parameters of the char layer are taken from [17]. Moreover, boundary surface for the water vapour exchange and pressure moves with the char front, as shown in Fig. 3.10. The change of the boundary surface position is discrete. It moves by the length of the finite element when the charring criterion is reached ($T_{\text{av,el}} > T_{\text{char}}$).

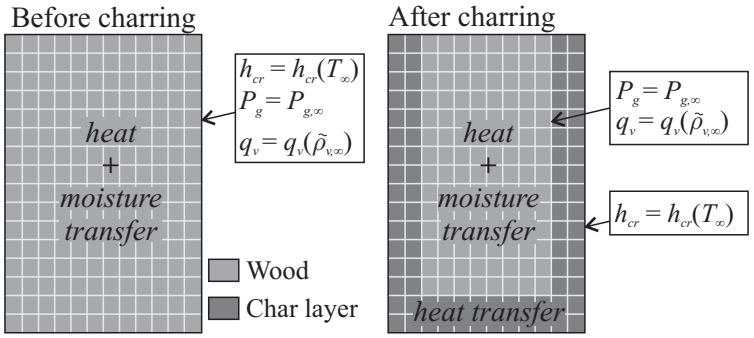

Figure 3.10: Charring formation in the presented model for timber specimen exposed to fire from three sides.

Slika 3.10: Prikaz modeliranja nastanka zoglenele plasti za lesen vzorec ognju izpostavljen iz treh strani.

3.4 Basic system of differential equations of coupled heat and moisture transfer model

Equations presented in section 3.2 do not have a known analytical solution. In order to find a solution, numerical approximations are done. Therefore, the governing equations (3.1)–(3.4) together with the constitutive relations presented in section 3.2.2 are rearranged to a form suitable for a numerical finite element formulation. The chosen primary unknowns of the coupled heat and moisture transfer model are: temperature T, pressure of gaseous mixture P_g, concentration of water vapour $\widetilde{\rho}_v$ and bound water concentration c_b. The system of differential equations for coupled heat and moisture transfer model with respect to primary unknowns can be written as:

$$C_{TT}\frac{\partial T}{\partial t}+(0)\frac{\partial P_g}{\partial t}+(0)\frac{\partial \widetilde{\rho}_v}{\partial t}+C_{TB}\frac{\partial c_b}{\partial t}= \\ =\nabla\cdot\left(K_{TT}\nabla T+(0)\nabla P_g+(0)\nabla\widetilde{\rho}_v+K_{TB}\nabla c_b\right)-K_{TVV}\nabla T, \quad (3.33)$$

$$C_{AT}\frac{\partial T}{\partial t}+C_{AP}\frac{\partial P_g}{\partial t}+C_{AV}\frac{\partial \widetilde{\rho}_v}{\partial t}+(0)\frac{\partial c_b}{\partial t}= \\ =\nabla\cdot\left(K_{AT}\nabla T+K_{AP}\nabla P_g+K_{AV}\nabla\widetilde{\rho}_v+(0)\nabla c_b\right), \quad (3.34)$$

$$(0)\frac{\partial T}{\partial t}+(0)\frac{\partial P_g}{\partial t}+C_{VV}\frac{\partial \widetilde{\rho}_v}{\partial t}+(0)\frac{\partial c_b}{\partial t}= \\ =\nabla\cdot\left(K_{VT}\nabla T+K_{VP}\nabla P_g+K_{VV}\nabla\widetilde{\rho}_v+(0)\nabla c_b\right)-\dot{c}, \quad (3.35)$$

$$(0)\frac{\partial T}{\partial t}+(0)\frac{\partial P_g}{\partial t}+(0)\frac{\partial \widetilde{\rho}_v}{\partial t}+C_{BB}\frac{\partial c_b}{\partial t}= \\ =\nabla\cdot\left(K_{BT}\nabla T+(0)\nabla P_g+(0)\nabla\widetilde{\rho}_v+K_{BB}\nabla c_b\right)+\dot{c}. \quad (3.36)$$

Below, the mathematical procedures to convert conservation equations together with constitutive relations to a system with primary unknowns (Eqs. (3.33)–(3.36)) are presented.

3.4.1 Fluxes of water vapour, air and bound water

The fluxes of each moving medium ($\mathbf{J}_v, \mathbf{J}_a, \mathbf{J}_b$) are rearranged so that they are expressed by the gradients of the primary unknowns ($\nabla T, \nabla P_g, \nabla\widetilde{\rho}_v, \nabla c_b$). The water vapour flux (Eq. (3.11)) is:

$$-\mathbf{J}_v=\frac{\mathbf{K}K_g}{\mu_g}\varepsilon_g\widetilde{\rho}_v\nabla P_g+\varepsilon_g\widetilde{\rho}_g\mathbf{D}_{av}\nabla\left(\frac{\widetilde{\rho}_v}{\widetilde{\rho}_g}\right). \quad (3.37)$$

By applying the chain rule and considering $\widetilde{\rho}_g=\widetilde{\rho}_v+\widetilde{\rho}_a$, the term $\widetilde{\rho}_g\nabla\left(\frac{\widetilde{\rho}_v}{\widetilde{\rho}_g}\right)$ on the right hand side of Eq. (3.37) can be expressed as:

$$\widetilde{\rho}_g\nabla\left(\frac{\widetilde{\rho}_v}{\widetilde{\rho}_g}\right)=\widetilde{\rho}_g\frac{\left(\widetilde{\rho}_a+\widetilde{\rho}_v\right)\nabla\widetilde{\rho}_v-\widetilde{\rho}_v\nabla\left(\widetilde{\rho}_v+\widetilde{\rho}_a\right)}{\left(\widetilde{\rho}_g\right)^2}=\frac{\left(\widetilde{\rho}_a\nabla\widetilde{\rho}_v\right)-\left(\widetilde{\rho}_v\nabla\widetilde{\rho}_a\right)}{\left(\widetilde{\rho}_g\right)}= \\ \left(\frac{\widetilde{\rho}_a\nabla\widetilde{\rho}_v}{\widetilde{\rho}_g}\right)-\left(\frac{\widetilde{\rho}_v\nabla\widetilde{\rho}_a}{\widetilde{\rho}_g}\right). \quad (3.38)$$

Considering (Eq. (3.13)) and $P_a=P_g-P_v$, the gradient $\nabla\widetilde{\rho}_a$ from Eq. (3.38) can be expanded as:

$$\nabla\widetilde{\rho}_a = \nabla\left(\frac{P_a}{R_aT}\right) = \nabla\left(\frac{P_g - P_v}{R_aT}\right) = \nabla\left(\frac{P_g}{R_aT} - \frac{R_v}{R_a}\widetilde{\rho}_v\right) = \frac{T\nabla P_g - P_g\nabla T}{R_aT^2} - \frac{R_v}{R_a}\nabla\widetilde{\rho}_v = \\ = \left(-\frac{P_g}{R_aT^2}\right)\nabla T + \left(\frac{1}{R_aT}\right)\nabla P_g + \left(-\frac{R_v}{R_a}\right)\nabla\widetilde{\rho}_v. \quad (3.39)$$

Inserting Eq. (3.39) into Eq. (3.38), the term $\widetilde{\rho}_g\nabla\left(\frac{\widetilde{\rho}_v}{\widetilde{\rho}_g}\right)$ yields to:

$$\widetilde{\rho}_g\nabla\left(\frac{\widetilde{\rho}_v}{\widetilde{\rho}_g}\right) = \left(\frac{P_g\widetilde{\rho}_v}{R_aT^2\widetilde{\rho}_g}\right)\nabla T + \left(-\frac{\widetilde{\rho}_v}{R_aT\widetilde{\rho}_g}\right)\nabla P_g + \left(\frac{\widetilde{\rho}_a}{\widetilde{\rho}_g} + \frac{R_v\widetilde{\rho}_v}{R_a\widetilde{\rho}_g}\right)\nabla\widetilde{\rho}_v. \quad (3.40)$$

Finally, the water vapour flux expressed by the gradients of the primary unknowns is obtained by inserting Eq. (3.40) into Eq. (3.37):

$$-\mathbf{J}_v = \underbrace{\left(\frac{\mathbf{D}_{av}\varepsilon_g P_g\widetilde{\rho}_v}{R_aT^2\widetilde{\rho}_g}\right)}_{K_{VT}}\nabla T + \underbrace{\varepsilon_g\widetilde{\rho}_v\left(\frac{\mathbf{K}K_g}{\mu_g} - \frac{\mathbf{D}_{av}}{R_aT\widetilde{\rho}_g}\right)}_{K_{VP}}\nabla P_g + \\ + \underbrace{\frac{\mathbf{D}_{va}\varepsilon_g}{\widetilde{\rho}_g}\left(\widetilde{\rho}_a + \frac{R_v}{R_a}\widetilde{\rho}_v\right)}_{K_{VV}}\nabla\widetilde{\rho}_v + (0)\nabla c_b. \quad (3.41)$$

The air flux (Eq. (3.10)) is:

$$-\mathbf{J}_a = \frac{\mathbf{K}K_g}{\mu_g}\varepsilon_g\widetilde{\rho}_a\nabla P_g + \varepsilon_g\widetilde{\rho}_g\mathbf{D}_{av}\nabla\left(\frac{\widetilde{\rho}_a}{\widetilde{\rho}_g}\right). \quad (3.42)$$

The term $\widetilde{\rho}_g\nabla\left(\frac{\widetilde{\rho}_a}{\widetilde{\rho}_g}\right)$ from Eq. (3.42) can be written as:

$$\widetilde{\rho}_g\nabla\left(\frac{\widetilde{\rho}_a}{\widetilde{\rho}_g}\right) = \widetilde{\rho}_g\nabla\left(\frac{\widetilde{\rho}_g - \widetilde{\rho}_v}{\widetilde{\rho}_g}\right) = \widetilde{\rho}_g\nabla\left(1 - \frac{\widetilde{\rho}_v}{\widetilde{\rho}_g}\right) = -\widetilde{\rho}_g\nabla\left(\frac{\widetilde{\rho}_v}{\widetilde{\rho}_g}\right). \quad (3.43)$$

Since the term $\widetilde{\rho}_g\nabla\left(\frac{\widetilde{\rho}_v}{\widetilde{\rho}_g}\right)$ was already derived in Eq. (3.40), the air flux can simply be written as:

$$-\mathbf{J}_a = \underbrace{\left(-\frac{\mathbf{D}_{av}\varepsilon_g P_g\widetilde{\rho}_v}{R_aT^2\widetilde{\rho}_g}\right)}_{K_{AT}}\nabla T + \underbrace{\left(\frac{\mathbf{K}K_g}{\mu_g}\varepsilon_g\widetilde{\rho}_a + \frac{\mathbf{D}_{av}\varepsilon_g\widetilde{\rho}_v}{R_aT\widetilde{\rho}_g}\right)}_{K_{AP}}\nabla P_g + \\ + \underbrace{\frac{\mathbf{D}_{va}\varepsilon_g}{\widetilde{\rho}_g}\left(-\widetilde{\rho}_a - \frac{R_v}{R_a}\widetilde{\rho}_v\right)}_{K_{AV}}\nabla\widetilde{\rho}_v + (0)\nabla c_b. \quad (3.44)$$

The bound water flux is already expressed in the form of gradients of the primary unknowns. Therefore:

$$-\mathbf{J}_b = \underbrace{\mathbf{D}_{bT}}_{K_{BT}}\nabla T + (0)\nabla P_g + (0)\nabla\widetilde{\rho}_v + \underbrace{\mathbf{D}_b}_{K_{BB}}\nabla c_b. \quad (3.45)$$

3.4.2 Time derivatives $\frac{\partial\left(\varepsilon_g\widetilde{\rho}_a\right)}{\partial t}$, $\frac{\partial\left(\varepsilon_g\widetilde{\rho}_v\right)}{\partial t}$ and $\frac{\partial c_b}{\partial t}$

The time derivatives $\frac{\partial(\varepsilon_g\widetilde{\rho}_a)}{\partial t}$, $\frac{\partial(\varepsilon_g\widetilde{\rho}_v)}{\partial t}$ and $\frac{\partial c_b}{\partial t}$ also need to be rearranged in the form of partial derivatives of primary unknowns with respect to time ($\frac{\partial T}{\partial t}$, $\frac{\partial P_g}{\partial t}$, $\frac{\partial\widetilde{\rho}_v}{\partial t}$, $\frac{\partial c_b}{\partial t}$). It is assumed that the porosity of wood remains unchanged during fire. Thus:

$$\varepsilon_g = \text{konst} \longrightarrow \frac{\partial\varepsilon_g}{\partial t} = 0. \tag{3.46}$$

The time derivative $\frac{\partial(\varepsilon_g\widetilde{\rho}_a)}{\partial t}$ can be derived by expressing the air concentration with the water vapour concentration and pressure of the gaseous mixture:

$$\widetilde{\rho}_a = \frac{P_a}{R_aT} = \frac{P_g - P_v}{R_aT} = \frac{P_g - \widetilde{\rho}_v R_v T}{R_aT} = \frac{1}{R_a}\frac{P_g}{T} - \frac{R_a}{R_v}\widetilde{\rho}_v, \tag{3.47}$$

and considering the partial derivative of air concentration with respect to time:

$$\frac{\partial\widetilde{\rho}_a}{\partial t} = \frac{1}{R_a}\frac{T\frac{\partial P_g}{\partial t} - P_g\frac{\partial T}{\partial t}}{T^2} - \frac{R_v}{R_a}\frac{\partial\widetilde{\rho}_v}{\partial t} = \\ = \left(-\frac{P_g}{R_aT^2}\right)\frac{\partial T}{\partial t} + \left(-\frac{1}{R_aT}\right)\frac{\partial P_g}{\partial t} + \left(-\frac{R_v}{R_a}\right)\frac{\partial\widetilde{\rho}_v}{\partial t}. \tag{3.48}$$

Therefore:

$$\frac{\partial\left(\varepsilon_g\widetilde{\rho}_a\right)}{\partial t} = \underbrace{\left(-\frac{\varepsilon_g P_g}{R_aT^2}\right)}_{C_{AT}}\frac{\partial T}{\partial t} + \underbrace{\left(\frac{\varepsilon_g}{R_aT}\right)}_{C_{AP}}\frac{\partial P_g}{\partial t} + \underbrace{\left(-\frac{\varepsilon_g R_v}{R_a}\right)}_{C_{AV}}\frac{\partial\widetilde{\rho}_v}{\partial t} + (0)\frac{\partial c_b}{\partial t}. \tag{3.49}$$

The determination of time derivatives $\frac{\partial(\varepsilon_g\widetilde{\rho}_v)}{\partial t}$ and $\frac{\partial c_b}{\partial t}$ is rather simple:

$$\frac{\partial\left(\varepsilon_g\widetilde{\rho}_v\right)}{\partial t} = (0)\frac{\partial T}{\partial t} + (0)\frac{\partial P_g}{\partial t} + \underbrace{\varepsilon_g}_{C_{VV}}\frac{\partial\widetilde{\rho}_v}{\partial t} + (0)\frac{\partial c_b}{\partial t}, \tag{3.50}$$

and

$$\frac{\partial c_b}{\partial t} = (0)\frac{\partial T}{\partial t} + (0)\frac{\partial P_g}{\partial t} + (0)\frac{\partial\widetilde{\rho}_v}{\partial t} + \underbrace{1}_{C_{BB}}\frac{\partial c_b}{\partial t}. \tag{3.51}$$

3.4.3 Energy conservation equation

The energy conservation equation also needs to be expressed by gradients and the partial derivatives of the primary unknowns with respect to time. The energy conservation equation is (Eq. 3.19):

$$\underline{\left(\rho C\right)}\frac{\partial T}{\partial t} = \nabla\cdot(\mathbf{k}\nabla T) - \underline{\left(\rho C\mathbf{v}\right)}\nabla T - \Delta H_s\dot{c}, \tag{3.52}$$

where sorption rate $\dot{c}$, expressed in Eqs. (3.1) and (3.5), is:

$$\dot{c} = \frac{\partial c_b}{\partial t} - \nabla\cdot\left(\mathbf{D}_b\nabla c_b + \mathbf{D}_{bT}\nabla T\right). \tag{3.53}$$

Energy conservation equation appropriate for the finite element formulation is obtained by inserting Eq. (3.53) into Eq. (3.52):

$$\underbrace{\left(\rho C\right)}_{C_{TT}}\frac{\partial T}{\partial t}+(0)\frac{\partial P_g}{\partial t}+(0)\frac{\partial \widetilde{\rho}_v}{\partial t}+\underbrace{\Delta H_s}_{C_{TB}}\frac{\partial c_b}{\partial t}= \nabla\cdot\left(\underbrace{(\mathbf{k}+\Delta H_s\mathbf{D}_{bT})}_{K_{TT}}\nabla T+(0)\nabla P_g+(0)\nabla\widetilde{\rho}_v+\underbrace{\mathbf{D}_b\Delta H_s}_{K_{TB}}\nabla c_b\right)-\underbrace{\left(\rho C\mathbf{v}\right)}_{K_{TVV}}\nabla T. \quad (3.54)$$

3.4.4 Boundary conditions

The heat flux at the boundary surface is determined by Eq. (3.27) as:

$$\frac{\partial T}{\partial n}=\frac{h_{cr}}{k}. \quad (3.55)$$

Considering $h_{cr}=h_{cr}^{*}\left(T_\infty-T\right)$, then the heat flux in Eq. (3.55) is:

$$\frac{\partial T}{\partial n}=\frac{h_{cr}^{*}}{k}T_\infty-\frac{h_{cr}^{*}}{k}T, \quad (3.56)$$

where h_{cr}^{*} is:

$$h_{cr}^{*}=\alpha_c+\varepsilon_m\varepsilon_f\sigma\left(T_\infty^2+T^2\right)\left(T_\infty+T\right). \quad (3.57)$$

From Eqs. (3.30) and (3.41), the vapour flux through the outer surface or the char layer can be written as:

$$-\mathbf{n}\cdot\mathbf{J}_v=K_{VT}\frac{\partial T}{\partial n}+K_{VP}\frac{\partial P_G}{\partial n}+K_{VV}\frac{\partial\widetilde{\rho}_v}{\partial n}=k_c\left(\widetilde{\rho}_{v,\infty}-\widetilde{\rho}_v\right). \quad (3.58)$$

The pressure in pores at the contact between timber and the surrounding air is equal to the ambient pressure. Therefore $\frac{\partial P_g}{\partial n}=0$. The temperature gradient in the direction of the normal $\frac{\partial T}{\partial n}$ is assumed to have a small impact on the boundary vapour flux and is thus not considered. Together with heat flux at the boundary surface (Eq. (3.56)), the boundary conditions in matrix form are written as:

$$\begin{Bmatrix}\frac{\partial T}{\partial n}\\ \\ \frac{\partial\widetilde{\rho}_v}{\partial n}\end{Bmatrix}=\underbrace{\begin{bmatrix}\frac{h_{cr}^{*}}{k} & 0\\ 0 & \frac{k_c}{K_{VV}}\end{bmatrix}}_{\mathbf{F}_\infty}\begin{Bmatrix}T_\infty\\ \\ \widetilde{\rho}_{v,\infty}\end{Bmatrix}-\underbrace{\begin{bmatrix}\frac{h_{cr}^{*}}{k} & 0\\ 0 & \frac{k_c}{K_{VV}}\end{bmatrix}}_{\mathbf{F}_k}\begin{Bmatrix}T\\ \\ \widetilde{\rho}_v\end{Bmatrix}. \quad (3.59)$$

3.5 Finite element formulation

The system of differential equations (Eqs. (3.33)–(3.36)) that need to be solved is written in matrix form as:

$$\mathbf{C}\dot{\mathbf{u}}-\nabla\cdot\left(\mathbf{K}_{ij}\nabla\mathbf{u}\right)+\mathbf{K}_V\nabla\mathbf{u}=\mathbf{F}_s, \quad (3.60)$$

with the corresponding boundary conditions:

$$\frac{\partial \mathbf{u}}{\partial n} = \mathbf{F}_\infty - \mathbf{F}_k \mathbf{u}, \tag{3.61}$$

and initial conditions:

$$\mathbf{u} = \mathbf{u}_0. \tag{3.62}$$

Here, $\mathbf{u}$ is a vector of the basic unknowns, $\mathbf{u} = \left[T\ P_g\ \widetilde{\rho}_v\ c_b\right]^{\mathrm{T}}$, matrices $\mathbf{C}$ and $\mathbf{K}_{ij}$ contain coefficients C_{ij} and K_{ij} ($i = T, A, V, B, j = T, P, V, B$), matrix $\mathbf{K}_V$ contains coefficient K_{TVV} and $\mathbf{F}_s$ is a vector that contains the sorption rate, $\mathbf{F}_s = [0\ 0\ -\dot{c}\ \dot{c}]^{\mathrm{T}}$. Matrices $\mathbf{F}_\infty$ and $\mathbf{F}_k$ are already presented in Eq. (3.59) and $\mathbf{u}_0 = \left[T_0\ P_{g,0}\ \widetilde{\rho}_{v,0}\ c_{b,0}\right]^{\mathrm{T}}$ is a vector of initial values of the basic unknowns at time $t = 0$.

In the finite element method the domain is divided into finite number of elements. Basic unknowns at time t are approximated across each element as functions of nodal unknowns:

$$\mathbf{u} = \mathbf{N}\mathbf{y}, \tag{3.63}$$

where $\mathbf{y}$ is the vector of discrete nodal unknowns and $\mathbf{N}$ is the matrix of polynomial shape functions for isoparametric four-node finite element:

$$\mathbf{N} = \begin{bmatrix} N_1 & N_2 & N_3 & N_4 & 0 & 0 & 0 & 0 & 0 & 0 & 0 & 0 & 0 & 0 & 0 & 0 \\ 0 & 0 & 0 & 0 & N_1 & N_2 & N_3 & N_4 & 0 & 0 & 0 & 0 & 0 & 0 & 0 & 0 \\ 0 & 0 & 0 & 0 & 0 & 0 & 0 & 0 & N_1 & N_2 & N_3 & N_4 & 0 & 0 & 0 & 0 \\ 0 & 0 & 0 & 0 & 0 & 0 & 0 & 0 & 0 & 0 & 0 & 0 & N_1 & N_2 & N_3 & N_4 \end{bmatrix},$$

$$\mathbf{y} = \begin{bmatrix} T_1 & T_2 & T_3 & T_4 & P_{g,1} & P_{g,2} & P_{g,3} & P_{g,4} & \widetilde{\rho}_{v,1} & \widetilde{\rho}_{v,2} & \widetilde{\rho}_{v,3} & \widetilde{\rho}_{v,4} & c_{b,1} & c_{b,2} & c_{b,3} & c_{b,4} \end{bmatrix}^{\mathrm{T}}.$$

Polynomial shape functions are defined as:

$$\begin{aligned} N_1 &= 1/4(1-\xi)(1-\eta), \quad & N_2 &= 1/4(1+\xi)(1-\eta), \\ N_3 &= 1/4(1+\xi)(1+\eta), \quad & N_4 &= 1/4(1-\xi)(1+\eta), \end{aligned} \tag{3.64}$$

where ξ and η take values on the interval $[-1, 1]$ as presented in Fig. 3.11.

Using the Galerkin method and integration by parts [46], the system of differential equations written in the matrix form (Eq. (3.60)) is transformed into a system of first-order differential equations.

$$\hat{\mathbf{C}}\dot{\mathbf{y}} + \hat{\mathbf{K}}\mathbf{y} = \hat{\mathbf{F}}, \tag{3.65}$$

where

$$\hat{\mathbf{C}} = \sum_{e=1}^{n_{el}} \hat{\mathbf{C}}^e, \quad \hat{\mathbf{K}} = \sum_{e=1}^{n_{el}} \hat{\mathbf{K}}^e + \hat{\mathbf{K}}_V^e + \hat{\mathbf{K}}_F^e, \quad \hat{\mathbf{F}} = \sum_{e=1}^{n_{el}} \hat{\mathbf{F}}^e + \hat{\mathbf{F}}_s^e, \quad \mathbf{u} = \sum_{e=1}^{n_{el}} \mathbf{u}^e,$$

$$\hat{\mathbf{C}}^e = \int_{\Omega_e} \mathbf{N}^T \mathbf{C}^e \mathbf{N} d\Omega, \quad \hat{\mathbf{K}}^e = \int_{\Omega_e} \nabla \mathbf{N}^T \mathbf{K}^e \nabla \mathbf{N} d\Omega, \quad \hat{\mathbf{K}}_V^e = \int_{\Omega_e} \mathbf{N}^T \mathbf{K}_V^e \nabla \mathbf{N} d\Omega,$$

$$\hat{\mathbf{K}}_F^e = \int_{\Gamma_e} \mathbf{N}^T \mathbf{K}^e \mathbf{F}_k^e \mathbf{N} d\Gamma, \quad \hat{\mathbf{F}}^e = \int_{\Gamma_e} \mathbf{N}^T \mathbf{K}^e \mathbf{F}_\infty^e d\Gamma, \quad \hat{\mathbf{F}}_s^e = \int_{\Omega_e} \mathbf{N}^T \mathbf{F}_s^e d\Omega,$$

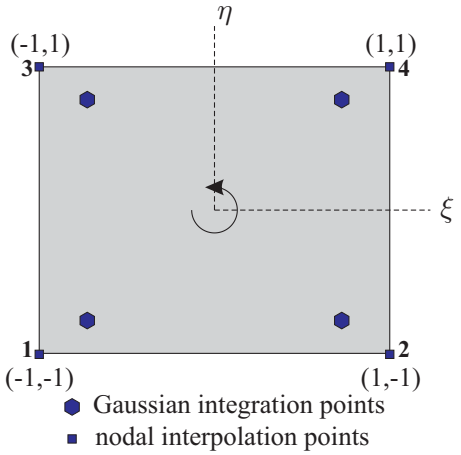

Figure 3.11: Four node isoparametric finite element.
Slika 3.11: Štiri-vozliščni isoparametrični končni element.

$$\mathbf{C}^e = \begin{bmatrix} C_{TT} & 0 & 0 & C_{TB} \\ C_{AT} & C_{AP} & C_{AV} & 0 \\ 0 & 0 & C_{VV} & 0 \\ 0 & 0 & 0 & C_{BB} \end{bmatrix}, \quad \mathbf{K}^e = \begin{bmatrix} K_{TT} & 0 & 0 & K_{TB} \\ K_{AT} & K_{AP} & K_{AV} & 0 \\ K_{VT} & K_{VP} & K_{VV} & 0 \\ K_{BT} & 0 & 0 & K_{BB} \end{bmatrix},$$

$$\mathbf{K}_V^e = \begin{bmatrix} K_{TVV} & 0 & 0 & 0 \\ 0 & 0 & 0 & 0 \\ 0 & 0 & 0 & 0 \\ 0 & 0 & 0 & 0 \end{bmatrix}, \quad \mathbf{F}_s^e = \begin{Bmatrix} 0 \\ 0 \\ -\dot{c} \\ \dot{c} \end{Bmatrix}, \quad \mathbf{u} = \begin{Bmatrix} T \\ P_g \\ \widetilde{\rho}_v \\ c_b \end{Bmatrix},$$

$$\mathbf{F}_\infty^e = \begin{Bmatrix} F_{T,\infty} \\ 0 \\ F_{v,\infty} \\ 0 \end{Bmatrix}, \quad \mathbf{F}_k^e = \begin{bmatrix} \frac{h_{cr}^*}{K_{TT}} & 0 & 0 & 0 \\ 0 & 0 & 0 & 0 \\ 0 & 0 & \frac{k_c}{K_{VV}} & 0 \\ 0 & 0 & 0 & 0 \end{bmatrix}.$$

Above, Ω_e represents the finite element model's domain and Γ_e is its edge with the prescribed boundary conditions. An implicit finite difference scheme is used for time discretisation. Within each time interval $[t^{k-1}, t^k]$ linear variation of nodal quantities is assumed. Eq. (3.65) is solved in each time step, i.e., at the time $t^k = t^{k-1} + \delta t$, where δt is the time increment. After considering the time discretisation, the system (3.65) can be written as follows:

$$\widetilde{\mathbf{C}}^k \mathbf{y}^k = \widetilde{\mathbf{F}}^k, \tag{3.66}$$

where

$$\widetilde{\mathbf{C}}^k = \hat{\mathbf{K}} + \frac{1}{\delta t}\hat{\mathbf{C}}, \tag{3.67}$$

and

$$\widetilde{\mathbf{F}}^k = \frac{1}{\delta t}\hat{\mathbf{C}}\mathbf{y}^{k-1} + \hat{\mathbf{F}}^k. \tag{3.68}$$

3.6 Numerical examples

In this section examples related to the proposed coupled heat and moisture model are presented. The first case analyses the influence of the mesh size on the charring depth. The second and the third case are introduced to validate the coupled heat and moisture transfer model. In the last case, sensitivity analysis is performed with the objective to simplify the proposed heat and moisture transfer model.

3.6.1 Finite element size convergence study

The impact of the mesh size on the charring depth and on the position of the moving boundary surface is investigated in convergence study. The analysis is performed on a timber specimen exposed to standard ISO fire on one side. The length of the specimen is 100 mm, the initial moisture content is m_0 = 12 % and the initial dry wood density is ρ_0 = 400 kg/m^3. The assumed char temperature is 300 °C. In the convergence study, the number of finite elements is varied from 5 to 320. The basic input data and finite element mesh for the case with 10 elements are shown in Fig. 3.12. In the analysis square elements are considered. Therefore, both element's dimensions are labelled as element size.

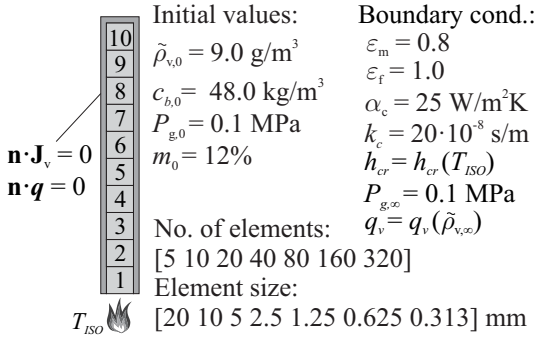

Figure 3.12: Geometry, initial values, boundary conditions and the number of finite elements employed in the convergence study.

Slika 3.12: Geometrija, začetne vrednosti, robni pogoji in število končnih elementov uporabljenih v konvergenčni študiji.

The relative error is defined as:

$$rer = \frac{d_{\text{char,n}} - d_{\text{char,320}}}{d_{\text{char,320}}}, \tag{3.69}$$

where $d_{\text{char,n}}$ is the charring depth calculated with n number of finite elements and $d_{\text{char,320}}$ is the reference charring depth obtained by the analysis with 320 finite elements. The reference value is determined by comparing the result for 160 and 320 finite elements, where the results do not differ by more than 1 ‰.

The development of charring depth as a function of time for 5, 20, 40 and 320 elements is depicted in Fig. 3.13a. The relative errors for the charring depths at different times (30 and 60 min) are illustrated in Fig. 3.13b. The charring depth and relative errors start converging towards the reference solution when 40 elements are used in the analysis. The relative errors for this case are 0.95 % and 0.79 % at 30 and 60 minutes, respectively, and are assumed to be acceptable. Therefore, to adequately predict the charring

depth with the present model, the size of the element depth should be 2.5 mm or less. This finding is employed also to other cases and parametric studies.

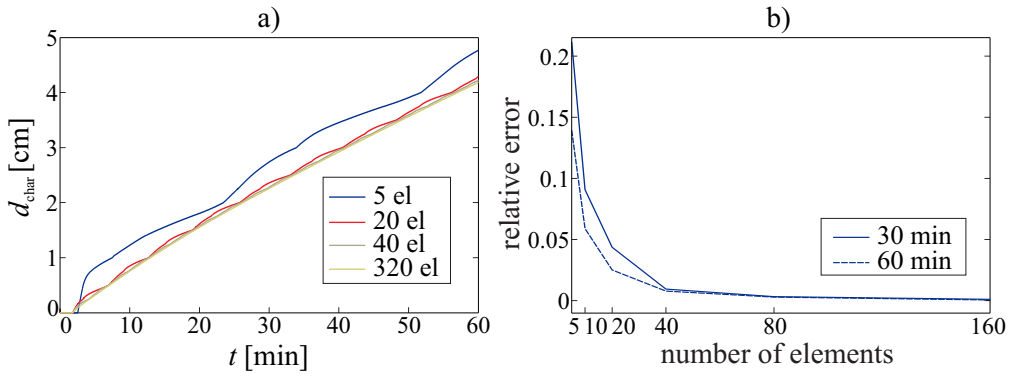

Figure 3.13: a) Charring depth development over time for different number of elements. b) Relative error for the charring depth.

Slika 3.13: a) Razvoj debeline zoglenele plasti s časom pri različnem številu končnih elementov. b) Relativna napaka za debelino zoglenele plasti.

As discussed in section 3.3, the change of the boundary surface position is discrete. The influence of the mesh size on the boundary surface position is presented in Fig. 3.14. Quantity d_{surf} is observed, which represents the distance from the exposed edge to the position of the boundary surface at different simulation times. As expected, the biggest discrete jumps are observed for the analysis with 5 finite elements. On the other hand, small discrete jumps of the boundary surface are observed when 320 elements are used in the analysis. The jumps correspond to the size of the finite elements.

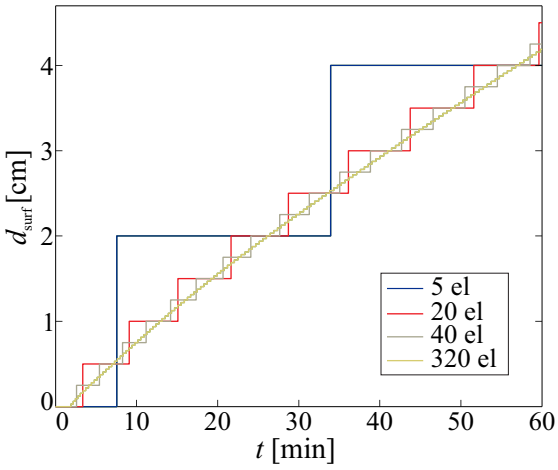

Figure 3.14: The impact of mesh size on the boundary surface position.

Slika 3.14: Vpliv velikosti mreže na položaj ploskve, kjer so predpisani robni pogoji.

At this point, the difference between d_{char} and d_{surf} should be explained. The charring depth d_{char} is determined by the interpolation of nodal temperatures. On the other hand, the boundary surface position is determined on the basis of the average finite element temperature ($T_{\text{av,el}}$), as described in section 3.3. When the average temperature reaches 300 °C, the position discretely moves by the finite element size.

3.6.2 Validation of coupled heat and moisture transfer model - temperatures

In the sequel the validation of the developed heat and moisture transfer model is presented. Numerical results are validated against the experimental results given by König and Walleij [77]. The experiment was conducted on unprotected spruce timber members exposed to ISO fire on one side with initial moisture content of 12 %. Temperatures were measured at the depths of 6, 18, 30 and 42 mm from the surface exposed to fire. Similar tests were carried out by Lache [78], where, in comparison to [77], specimens with initial moisture content of 20 % were investigated. In this case, the temperatures were measured at the depths of 10, 20, 30, 40 and 50 mm. The same type of wood as in [77] was used.

Geometry of the specimen and basic input data for the numerical analyses are presented in Fig. 3.15. Graph on the right-hand side of Fig. 3.15 shows vapour concentration in the surroundings, needed to determine the vapour flux through the outer surface or the char layer. Additional data required for the numerical analyses are given in Table 3.1. The cross-section of timber specimen is modelled with 40 finite elements. Temperature dependent thermal conductivity, specific heat and density of wood were obtained from [17].

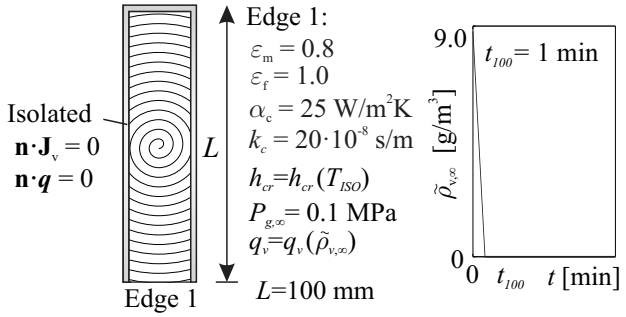

Figure 3.15: Geometry and boundary conditions accounted for in the temperature validation analysis.
Slika 3.15: Geometrija in robni pogoji upoštevani v primeru temperaturne validacije.

As observed from the results (Fig. 3.16), good agreement is obtained for the analysis with the initial moisture content of 12 %. More discrepancies in the distribution of temperatures are observed for the case with 20 % initial moisture content (Fig. 3.16b). One reason for this variation can be the energy release rate during the evaporation of moisture above the boiling point. Although the total energies of the evaporation from the experiment and simulation should be equal, there is, however, a difference in the release rate. In the experiment the evaporation is immediate, seen as extended plateau at around 100 °C. In the model, the energy of evaporation follows the desorption of bound water above the boiling temperature. For this reason the calculated and the measured temperatures agree better for times $t > 45$ min. It should be mentioned that the experimentally measured temperatures shown in Fig. 3.16b at 30 mm, after 40 minutes of fire exposure, are questionable, since the temperatures are higher compared to the measured temperatures in the case with the lower initial moisture content (Fig. 3.16a). Based on the validation analysis results it can be concluded that the coupled heat and moisture transfer model is capable of reproducing an accurate temperature field for timber members exposed to fire.

Table 3.1: Input data for temperature–moisture analysis.
Preglednica 3.1: Vhodni podatki za toplotno–vlažnostno analizo.

Material parameters	Used value	Unit
Universal gas constant	$R = 8.3144$	J/molK
Gas constant for water vapour	$R_v = 461.5$	J/kgK
Gas constant for air	$R_a = 287$	J/kgK
Diffusion coefficient tangential dir.	$D_T^0 = 7 \cdot 10^{-6}$	m^2/s
Specific permeability of dry wood	$K = 5 \cdot 10^{-16}$	m^2
Relative permeability of gaseous mixture	$K_g = 1$	
Direction dependent reduction factor	$\zeta = 0.03$	
Specific heat of water	$C_w = 4200$	J/kgK
Specific heat of water vapour	$C_v = 1800$	J/kgK
Specific heat of air	$C_a = 1000$	J/kgK
Heat of sorption	$\Delta H_s = 2500$	kJ/kg
Initial dry density of timber	$\rho_0 = 445$	kg/m^3
Initial moisture content	$m_0 = [12\ 20]$	%
Initial bound water concentration	$c_{b0} = [53.4\ 89]$	kg/m^3
Initial water vapour concentration in lumens	$\widetilde{\rho}_{v,0} = [9\ 15]$	g/m^3
Initial gas pressure	$P_{g,0} = 100$	kPa
Initial temperature	$T_0 = 20$	°C
Sorption parameters		
$b_{10}^d = 16.3,\ b_{11}^d = -0.0367,\ b_{20}^d = 2.13,\ b_{21}^d = 0.0535$		
$C_1 = 2.7 \cdot 10^{-4},\ C_{21} = 2.74 \cdot 10^{-5},\ C_{22} = 19,\ C_3 = 60,\ C_4 = 1 \cdot 10^{-7}$		

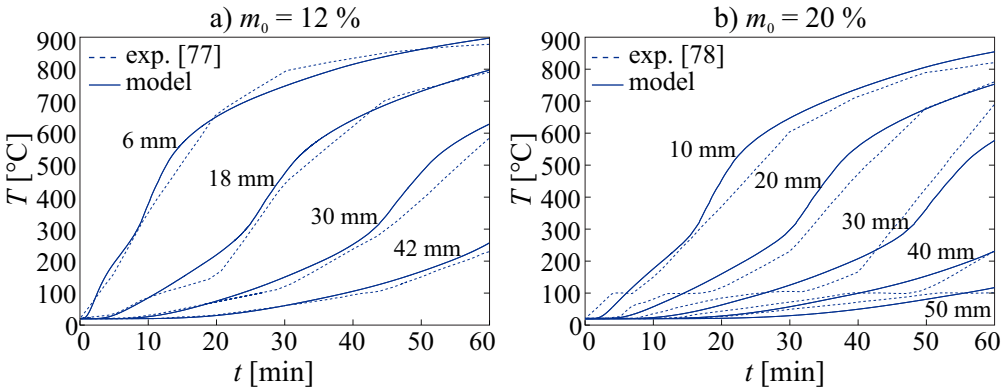

Figure 3.16: Comparison of experimentally measured and numerically calculated temperatures.
Slika 3.16: Primerjava izmerjenih in numerično določenih temperatur.

3.6.2.1 Development of basic unknowns m, $\widetilde{\rho}_v$ and P_g

Additionally, the development of other three basic unknowns that the coupled heat and moisture transfer model predicts, i.e. moisture content, water vapour and gas pressure, as well as post processed bound water and water vapour flux, are presented. Note that moisture content m is a quantity directly correlated to the bound water concentration, determined as $m = c_b/\rho_0$, and is therefore considered as the basic unknown. Fig. 3.17 presents the distribution of the three basic unknowns at chosen times and at different locations. The results for the specimen with the initial moisture content 12 % are presented.

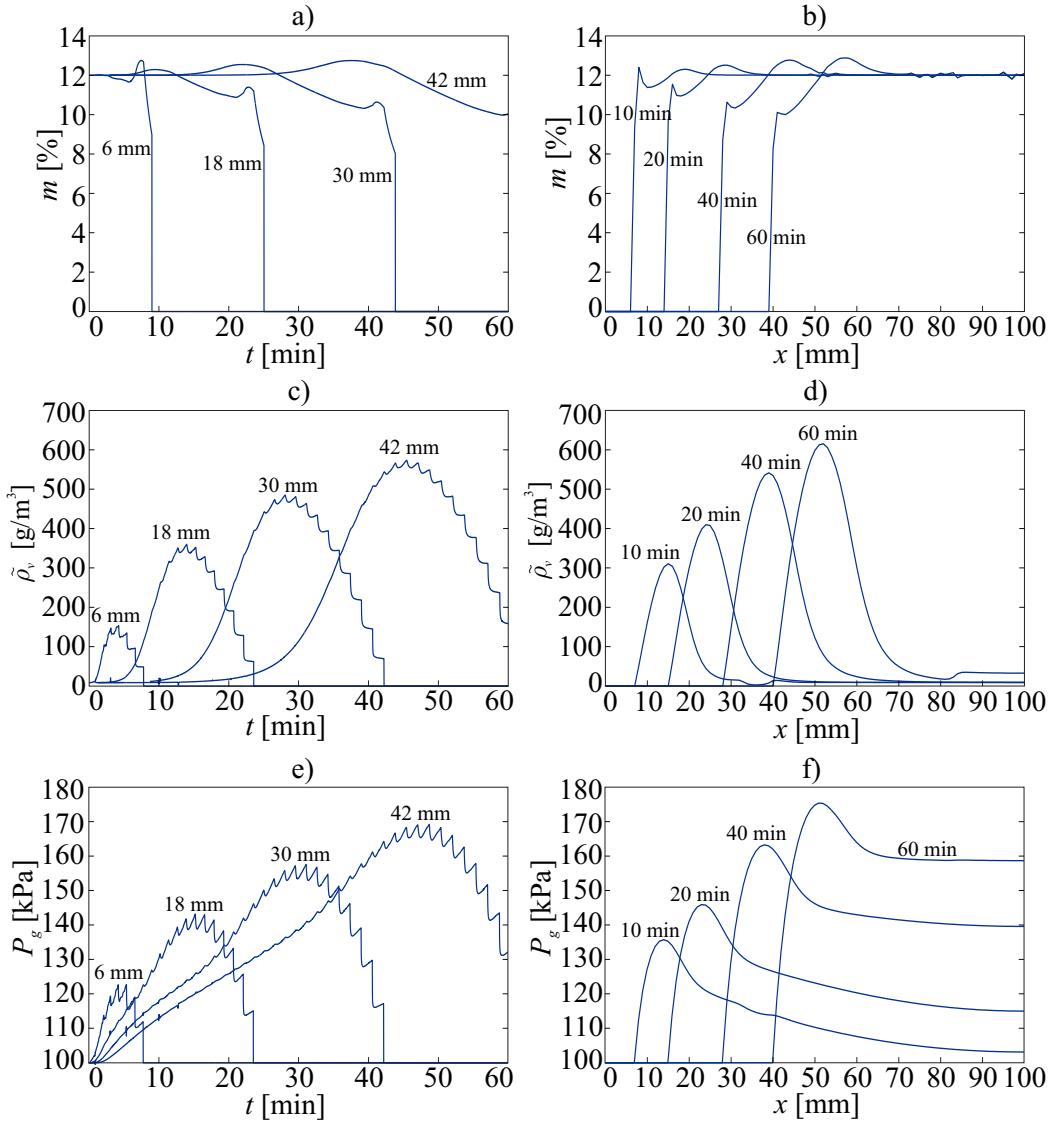

Figure 3.17: Development of moisture content m, vapour concentrarion $\widetilde{\rho}_v$ and gas pressure P_g over time at given location (a, c, e) and along the specimen length at chosen times (b, d, f).

Slika 3.17: Razvoj vsebnosti vlage m, koncentracije vodne pare $\widetilde{\rho}_v$ in pritiska P_g s časom v različnih točkah lesenega vzorca (a, c, e) in vzdolž vzorca pri izbranih časih (b, d, f).

The charring occurrence is clearly indicated in Fig. 3.17 by abrupt drops of the moisture content, vapour concentration and gas pressure. Jagged curves in pore pressure and water vapour time development

(Figs. 3.17c and e) are the consequence of the moving boundary surface when charring occurs. When the charring criterion is met ($T_{\mathrm{av,el}} > T_{\mathrm{char}}$) the boundary surface position changes discretely by the step size of the finite element mesh. Consequently, the water vapour flux towards the boundary surface suddenly increases, which leads to the abrupt decrease of water vapour, seen as the jagged curve in Fig. 3.17c. Partial pressure of the gaseous mixture is approximated by the ideal gas law, and therefore directly correlated to the water vapour concentration. For this reason, curve in Fig. 3.17e is jagged as well. The rapid increase of water vapour concentration is shown in Fig. 3.17c and d. Desorption and heat driven vapour diffusion increases the concentration of water vapour locally behind the char layer. In turn, this causes adsorption further in the specimen, which can be observed as peaks in moisture content (Figs. 3.17a and b). On the other hand, peaks in the moisture content observed immediately behind the char layer (Fig. 3.17a) are a consequence of desorption and slow bound water diffusion. Further on, Fig. 3.17f shows the internal pressure increase with time as expected with the current boundary conditions.

Interesting are also the following two quantities, i.e. bound water flux $\mathbf{J}_{\mathrm{b}}$, and water vapour flux $\mathbf{J}_{\mathrm{v}}$, that can be post processed from Eqs. (3.5) and (3.11). Their development along the specimen at chosen times is presented in Fig. 3.18. Firstly, the location in the specimen when a change in the sign of the fluxes is observed is the location where bound water and water vapour transfer change direction. Negative sign of the fluxes indicates that bound water and water vapour move toward the boundary surface. On the other hand, positive sign represents that both water phases move into the interior of the specimen. Furthermore, a significant difference in the magnitude of both fluxes is evident ($\mathbf{J}_b \ll \mathbf{J}_v$) confirming the findings of Svensson and Hozjan [72].

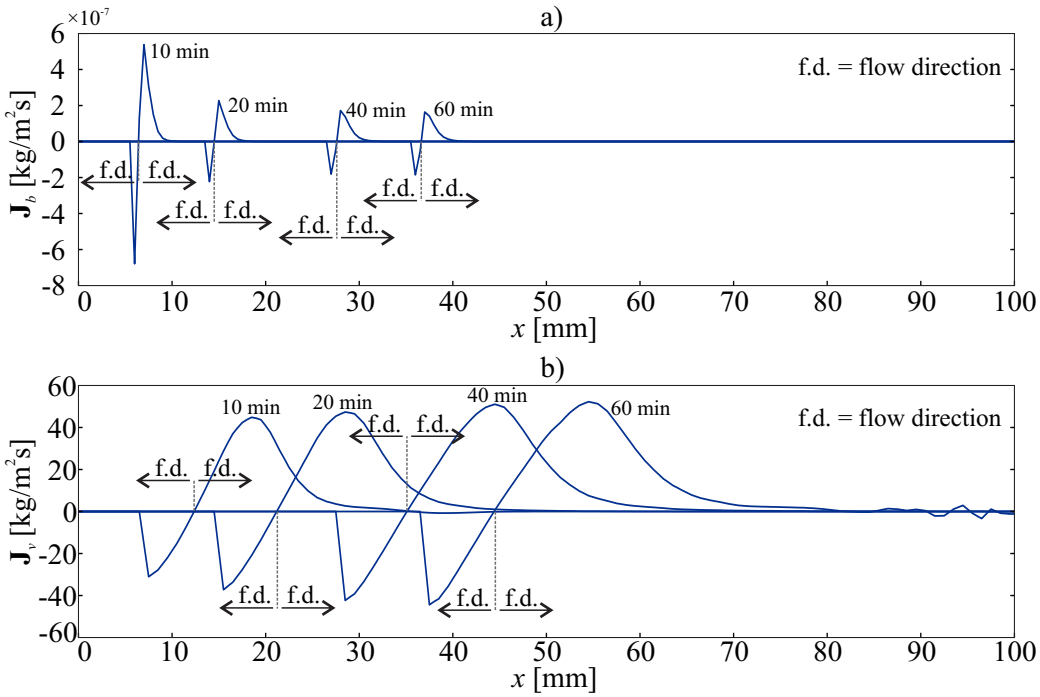

Figure 3.18: The development of bound water flux $\mathbf{J}_b$ and water vapour flux $\mathbf{J}_v$ along the specimen.
Slika 3.18: Razvoj toka vezane vode $\mathbf{J}_b$ in vodne pare $\mathbf{J}_v$ vzdolž vzorca.

3.6.2.2 Development of basic unknowns - different heating regime

As a supplement to section 3.6.2, the specimen with initial moisture content 12 %, but exposed to a different heating regime is considered here. Linear heating regime is applied (Fig. 3.19), where the maximum ambient temperatures remain below the char front temperature ($T_\infty < 300$ °C), and reach 250 °C after 10 minutes of exposure. After that, plateau lasting 110 minutes is considered. The cooling phase begins after 120 minutes of the simulation. It is assumed that the material properties of wood are the same in the cooling and the heating phase. The objective here is to present the development of basic unknowns of the coupled heat and moisture transfer model. All the quantities are measured at depths of 6, 18, 30 and 42 mm from the surface exposed to elevated temperatures. The depths are hereinafter referred to as points $P_1 - P_4$.

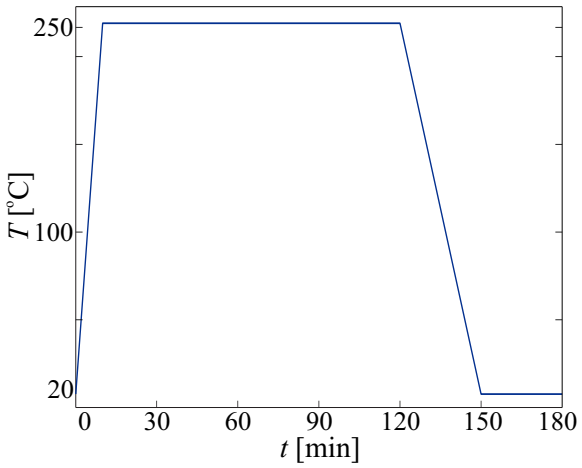

Figure 3.19: Linear heating regime combined with the cooling phase.
Slika 3.19: Linearni režim ogrevanja skupaj z fazo ohlajanja.

Fig. 3.20 presents the development of the basic unknowns. Maximum observed temperatures at points $P_1 - P_4$ are 208 °C, 158 °C, 120 °C and 100 °C (Fig. 3.20a). The temperature increase is the fastest in point P_1 since it is closest to the exposed edge. For the same reason, also the temperature decrease in this point is the most rapid and starts at about the same time as the cooling phase of the surrounding environment (t = 121 min). The temperature decrease in other points ($P_2 - P_4$) is slightly delayed. This occurs because the temperature in these points is still lower compared to the temperatures in points closer to the exposed edge. Since thermal equilibrium in the specimen is not reached, temperatures in points $P_2 - P_4$ are still increasing, despite the fact that ambient temperature is decreasing.

Figs. 3.20c and d represent the development of moisture content with time and along the specimen. Due to the temperature increase, the specimen at the location of points P_1 and P_2 is subjected to bound water desorption seen as the decrease of moisture content during the simulation. In points P_3 and P_4 the reverse process, i.e. adsorption, occurs, since the increase of moisture content during the simulation is observed. This means that the part of the specimen closer to the exposed edge dries while the inner core is gaining moisture content throughout the simulation. This phenomenon is recognized as moisture front progression. To describe it, the developments of temperature, moisture content and water vapour concentration at the time 40 minutes (Figs. 3.20b, d and f) are observed. At $x \in [0\ 17]$ mm the temperatures are above

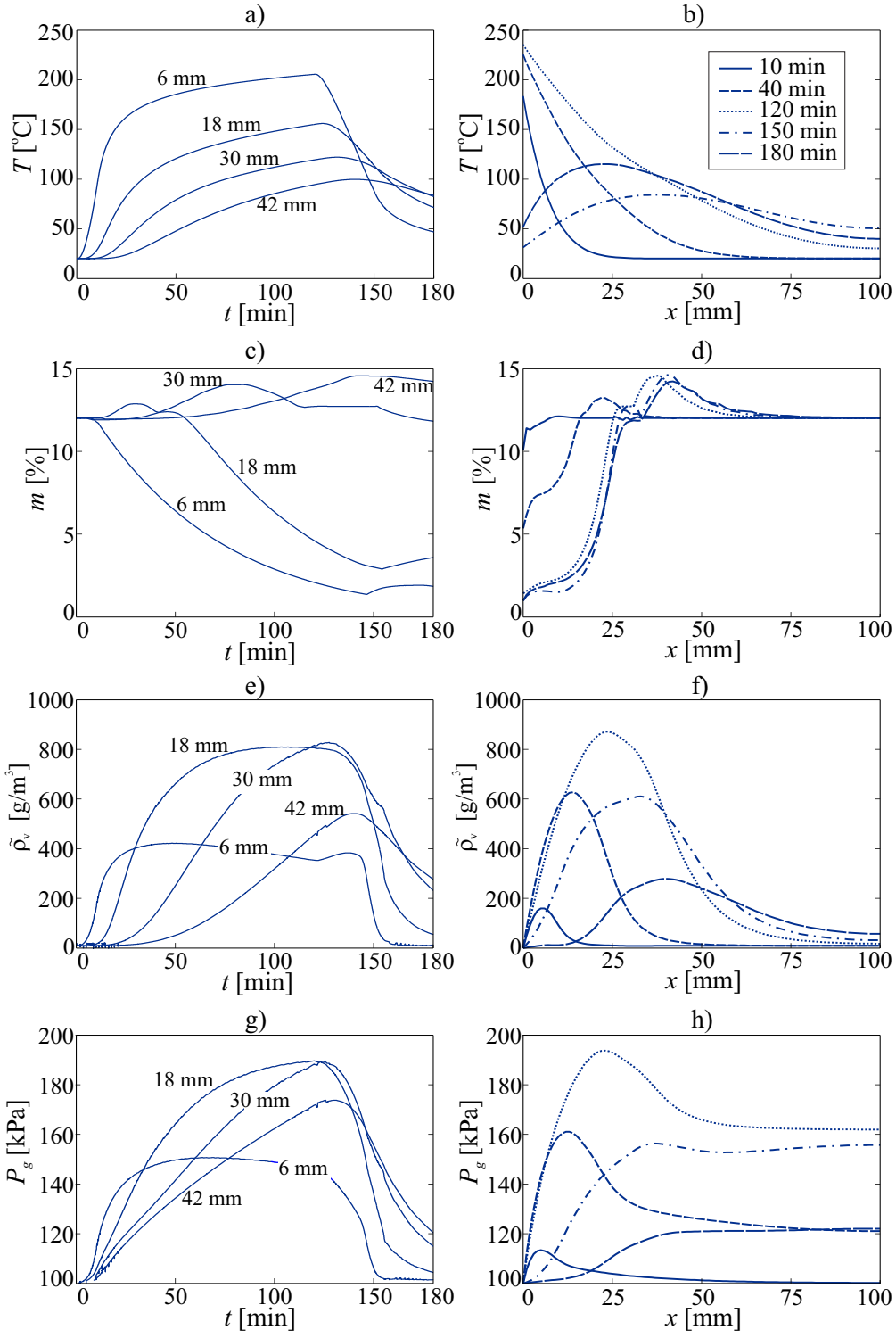

Figure 3.20: Temperature, moisture content, water vapour and pore pressures distribution over time in points $P_1 - P_4$ (a, c, e, g) and along the specimen for the chosen times (b, d, f, h).

Slika 3.20: Razvoj temperature, vlage, vodne pare in pritiskov s časom v točkah $P_1 - P_4$ (a, c, e, g) in vzdolž vzorca za izbrane čase (b, d, f, h).

the boiling temperature ($T \geqslant T_{boil}$). For this reason wood dries, which leads to increased water vapour concentration. Due to the concentration gradient of water vapour and thermally driven water vapour flux,

the water vapour moves in the interior of the specimen at $x \in [17\ 50]$ mm. In turn, high water vapour concentration is present in the part of the specimen with lower temperatures ($T < 100$ °C). The water vapour potential in this part of the specimen is higher than the bound water potential. Therefore, adsorption of water vapour into bound water occurs. This can be seen in Fig. 3.20d as increase of the moisture content at $x \in [17\ 50]$ mm.

Partial pressure of the gaseous mixture is approximated by the ideal gas law, and therefore directly correlated to the temperature and to the water vapour concentration. This correlation is reciprocal and obvious when comparing Figs. 3.20a, e and g with each other. The increase of temperature and water vapour concentration leads to the increase of pressure and vice versa.

Compared to the case presented in section 3.6.2.1, where the specimen was exposed to standard ISO fire curve and charring occured, in this study, the charring did not occur, since the ambient temperature remained under 300 °C. By comparing the results of both analyses (Figs. 3.17 and 3.20), the influence of charring and moving boundary surface on the development of basic unknowns can be identified. Two major differences are discovered. In the case without charring, there are no abrupt drops of the moisture content (Fig. 3.20c and d). Secondly, the development of water vapour and gas pressure is smooth (Figs. 3.20e and g), and not jagged as seen in Figs. 3.17c and e.

3.6.3 Validation of coupled heat and moisture transfer model - charring depth

The objective of this study is to validate the heat and moisture transfer model by comparing the numerically and experimentally determined charring depths. The experiment was performed by Yang et al. [79, 80], where charring depths of glued laminated timber subjected to the standard fire ISO curve from three sides were measured. The glulam beams were made from seven Douglas fir lamellas, each with a size of 38 mm (thickness) × 140 mm (width), with total cross-section height of 266 mm. In the experiment, the charring depth was determined by comparing the unburned cross-section dimensions at the end of the experiment with the initial cross-section dimensions.

In Fig. 3.21, the basic input data, finite element mesh and geometry of the cross-section for the numerical analysis are presented. The cross-section is discretized into 2968 four-node quadrilateral finite elements, giving the size of one finite element 2.5×2.5 mm. Due to the different timber used in the experiment, the following model parameters differ from those given in section 3.6.2: ρ_0 = 511 kg/m^3, c_{b0} = 51.6 kg/m^3 and $\widetilde{\rho}_{v,0}$ = 6.9 g/m^3. The char front temperature in the model is set to 300°C [17].

Experimentally and numerically determined charring depths are presented in Table 3.2. The measured charring depths represent the average from five cut slices, where the values in the parentheses denote standard deviations. As observed, good agreement is obtained between the measured and the calculated charring depths. All numerical values are within the range defined by the average value and standard deviation determined experimentally. Therefore, the assumption with char front temperature at 300°C for fires with heating regime similar to ISO curve seems to be reasonable.

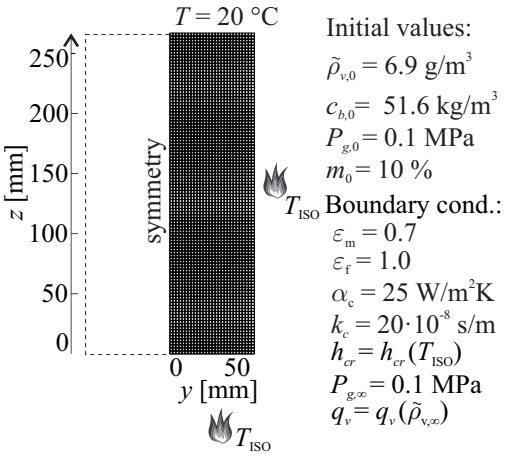

Figure 3.21: Basic input data, geometry of the cross-section and finite element mesh for the charring depth validation analysis.

Slika 3.21: Osnovni podatki, geometrija prečnega prereza in mreža končnih elementov za analizo validacije debeline zoglenele plasti.

Table 3.2: Charring depths in mm.

Preglednica 3.2: Debeline zoglenele plasti v mm.

	Experiment [79, 80]		Numerical model	
	Lateral side	Bottom side	Lateral side	Bottom side
30 min	18.8 (2.7)	20.8 (2.0)	18.8	19.2
45 min	26.4 (2.8)	30.3 (2.4)	27.2	28.2
60 min	37.4 (4.2)	37.9 (1.6)	35.3	38.4

3.6.4 Sensitivity analysis of coupled heat and moisture model

When solving a highly precise mathematical model, certain costs are expected, especially in terms of computational time. Therefore, one can seek for model simplifications, provided that their impact on the model precision is insignificant. A strong tool to evaluate the impact of input variables on the selected output variables of the numerical model is sensitivity analysis [81, 82]. One of the possible approaches to carry out the sensitivity analysis is to vary the input values in order to determine the effect of these changes on the examined outputs. This approach is convenient for simplifying complex models as well as model verification and validation.

Due to the simplicity and easy interpretation of the results, the sensitivity analysis is performed by standardized regression coefficient method (SRC). Having a sample of n independent observations, the multiple linear regression model is obtained as:

$$\mathbf{Y} = \beta_0 + \mathbf{X}\boldsymbol{\beta} + \boldsymbol{\varepsilon}. \tag{3.70}$$

Here, $\mathbf{Y} = (Y_1, Y_2, ..., Y_n)^T$ denotes a $1 \times n$ column vector of output variables, $\boldsymbol{\beta} = (\beta_1, \beta_2, ..., \beta_m)^T$ is

a vector of the unknown unstandardised regression coefficients, where m is a total number of input parameters, β_0 is the regression intercept, $\boldsymbol{\varepsilon} = (\varepsilon_1, \varepsilon_2, ..., \varepsilon_n)^T$ is the residual error of the model which is assumed to be normally distributed with a mean equal to zero and variance σ^2 and $\mathbf{X} = (X_{i1}, X_{i2}, ..., X_{im})$ for $i = 1, 2, ..., n$ is the $n \times m$ matrix representing the input parameter space. In order to determine the standardized regression coefficients, the regression model (Eq. (3.70)) needs to be re-parametrized. In turn, $\mathbf{X}$ and $\mathbf{Y}$ are centred by their average values $\overline{X}$ and $\overline{Y}$ and normalized by their standard deviations σ_X and σ_Y:

$$\frac{\mathbf{Y} - \overline{Y}}{\sigma_Y} = \boldsymbol{\beta}^* \frac{\mathbf{X} - \overline{X}}{\sigma_X} + \boldsymbol{\varepsilon}, \tag{3.71}$$

where $\boldsymbol{\beta}^*$ is a vector of standardized regression coefficients which are computed with the least square method by minimizing the residual error. The SRC method can be applied if the coefficient of determination R^2 is above the recommended value 0.7 [83, 84]. More detailed description of standardized regression coefficient method can be found in [85–87].

The importance of accurately predicted outcomes from the coupled heat and moisture model can be seen in the next phase of the fire analysis, where mechanical response of timber elements exposed to fire is performed [88–90]. The mechanical behaviour is influenced mainly by the reduced mechanical characteristics of timber correlated with charring [91]. In addition, it is also influenced by the coupled effect of stress and changing moisture state, called mechano-sorptive effect [41, 92]. Therefore, the outcomes identified as interesting are charring depth d_{char} and total moisture content m_{tot} in the specimen.

Furthermore, it is known that the thermal conductivity, specific heat and density of material have a dominant role in heat transfer through a solid body [76]. The same may apply for the heat transfer through porous material such as wood. However, the aim of this case is to identify the influence of the moisture transfer in the coupled heat and moisture transfer model on output parameters d_{char} and m_{tot}. Hence, it is reasonable to vary parameters directly related to the moisture transfer. These are specific permeability of dry wood K, bound water diffusion coefficient D_0, vapour diffusion coefficient ζ and heat of sorption ΔH_s. Their values and variations are presented in Table 3.3. The basic fixed input data and geometry of the wooden specimen are shown in Fig. 3.22.

Fig. 3.23 presents the magnitude of SRC, indicating the influence of input parameters on the selected output quantities, i.e on the total moisture content (Fig. 3.23a) and on the charring depth (Fig. 3.23b). The SRC are examined at t = 50 minutes of fire simulation and at different initial moisture contents, i.e. $m_{0,i}$ = [8 12 20] %, and may take values between -1 and 1. The sign of the SRC expresses the correlation between the input and the output. For instance, a positive SRC demonstrates that increase in input parameter results in increased output parameter [84]. Figs. 3.23a and b show that heat of sorption dominates in all cases. At higher heat of sorption more energy is required for heating the specimen. Therefore, slower temperature increase in timber and smaller charring depth are expected. For this reason, negative correlation of $\Delta H_s \sim d_{char}$ is observed. Results also reveal that the effect of bound water diffusion (D_0) is always significant, especially on the total moisture content (SRC ≈ 0.8). On the other hand, Hozjan and Svensson [72] reported that bound water diffusion had the least influence on the model outcomes. Nonetheless, they investigated moisture transport in wood at room temperature and the diffusivity was assumed to follow the Arrhenius law [93]. Here, the diffusivity equation is also supplemented by the Soret effect, which was proven to be the dominating driving force at elevated

temperatures [94].

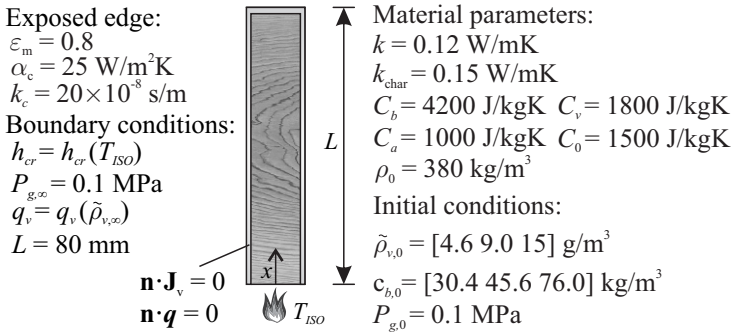

Figure 3.22: Material parameters, initial and boundary conditions and geometry of the wooden specimen for the sensitivity analysis. Different initial vapour and bound water concentrations correspond to the different initial moisture contents of the specimen.

Slika 3.22: Materialni parametri, začetni in robni pogoji in geometrija lesenega vzorca za analizo občutljivosti. Različne začetne koncentracije vodne pare in vezane vode ustrezajo različni začetni vsebnosti vlage vzorca.

Table 3.3: Varying parameters for sensitivity analysis.
Preglednica 3.3: Spreminjajoči parametri za analizo občutljivosti.

Parameter	Nominal value	Unit	Range	
			Minimum	Maximum
K^*	$1\cdot10^{-16}$	m^2	$9\cdot10^{-17}$	$1.1\cdot10^{-16}$
D_0^*	$7\cdot10^{-6}$	m^2/s	$6.3\cdot10^{-6}$	$7.7\cdot10^{-6}$
ζ^*	0.03		0.027	0.033
ΔH_s^*	2500	kJ/kg	2250	2750

* ± 10 % of the nominal value with the step of 5 %

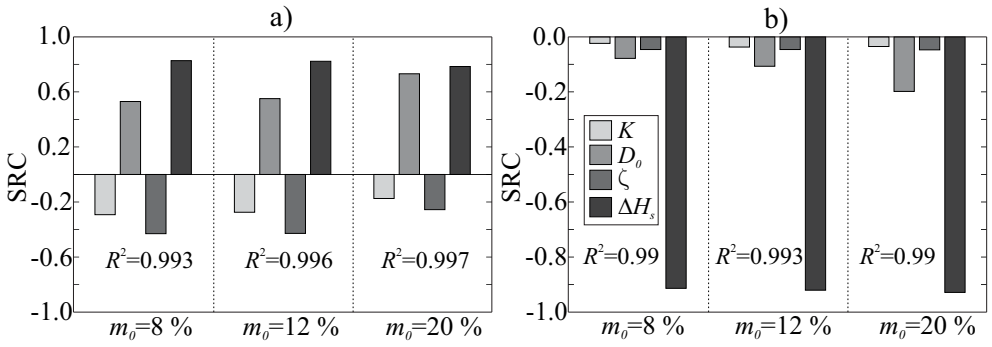

Figure 3.23: SRC's for: a) Total moisture content. b) Charring depth.

Slika 3.23: SRC-ji za: a) Skupno vsebnost vlage. b) Debelino zoglenele plasti.

The input parameters specific permeability of dry wood K and vapour diffusion coefficient ζ are important to predict the total moisture content. However, their effect on the charring depth is negligible. To introduce model simplifications, a step forward would be to investigate if there exists a link between the charring depth and these two input parameters. In the presented model, charring is temperature dependent and for this reason mainly governed by the energy equation (Eq. (3.19)). An obvious step is to find the effect of parameters K and ζ on the heat transfer. This connection arises through the relationship $\underline{\rho C \mathbf{v}} = \left(\varepsilon_g \widetilde{\rho}_a C_a + \varepsilon_g \widetilde{\rho}_v C_v\right) \mathbf{v}_g$, where the velocity of gas mixture $\mathbf{v}_g$ is a function of specific permeability of dry wood: $\mathbf{v}_g = \dfrac{K}{\mu_g} \nabla P_g$. Since it was shown that the influence of K on the charring depth is negligible, it can be further assumed that the heat transfer by convection($\underline{\rho C \mathbf{v}}$) has minor impact as well. Therefore, the energy conservation equation (Eq. (3.19)) can be simplified into:

$$\left(\underline{\rho C}\right) \frac{\partial T}{\partial t} = \nabla \cdot (\mathbf{k} \nabla T) - \Delta H_s \dot{c} \tag{3.72}$$

The results from analyses with full term energy equation (full line, Eq. (3.19)) and simplified energy equation (dashed line, Eq. (3.72)) are presented in Fig. 3.24. As can be observed, the convective heat transfer has an insignificant impact on temperature distribution and the simplification of the energy equation seems reasonable. Therefore, in the further cases and in the parametric studies, the coupled heat and moisture model with simplified energy equation (Eq. (3.72)) is employed.

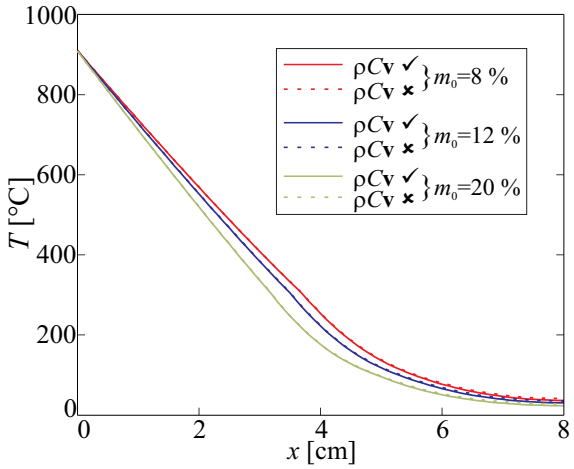

Figure 3.24: Distribution of temperatures along the specimen at time t = 50 min, for different initial moisture contents and for different energy equations considered.

Slika 3.24: Razpored temperatur po lesenem vzorcu pri času t = 50 min, za različne začetne vsebnosti vlage in ob različno upoštevani energijski enačbi.

"Blank page"

4 BASIC EQUATIONS FOR TAPERED AND CURVED TIMBER BEAMS

In this chapter, the last phase of the fire analysis is presented, where the mechanical response of tapered and curved timber beam simultaneously exposed to mechanical and fire load is determined. Temperature and moisture field determined in section 3 are used as input data for the mechanical analysis.

Mathematical model to describe beam deformation is based on the Reissner's kinematically exact beam model [48]. The model accounts for the membrane, shear and flexural deformations of the beam. Timoshenko hypothesis is adopted, assuming that the beam cross-section remains straight, but no longer perpendicular to the reference axis of the beam in the deformed state. In addition, it is considered that the shape and size of the cross-section remain the same during deformation. According to the Reissner model, stress and strain state of the beam is described by solving the system of kinematic, equilibrium and constitutive equations with the corresponding boundary conditions. The governing equations are discretized by the Galerkin finite element method and solved within each time step $\left[t^{i-1}, t^{i}\right]$ by the Newton's incremental-iterative procedure.

4.1 Kinematic equations

The deformation of the planar curved beam with initial length L is observed in the (X,Z) plane of the Euclidean space with the Cartesian coordinate system (X,Y,Z) and orthonormal base vectors $\mathbf{E}_X, \mathbf{E}_Z$ and $\mathbf{E}_Y = \mathbf{E}_X \times \mathbf{E}_Z$. Undeformed and deformed configurations of the beam are presented in Fig. 4.1. Vector $\mathbf{r}_0 = (X(s), 0, Z(s))$ represents the centroid of the beam, where s is an arc-length parameter. Material points of the beam are determined by the curvilinear material coordinates (ξ, η, ζ), where the material coordinate axis $\mathbf{r}_0 = (\xi(s), 0, 0)$ coincides with the centroid axis of the beam in undeformed state. Material base in the deformed state is defined by vectors $\mathbf{e}_\eta$ and $\mathbf{e}_\zeta$, that lie in the plane of the deformed cross-section, and vector $\mathbf{e}_\xi$, which is perpendicular to it. Unit vectors perpendicular and parallel to the deformed centroid axis are labelled as $\mathbf{e}_t$ and $\mathbf{e}_n$. Vector pairs $\mathbf{e}_\xi$, $\mathbf{e}_t$ and $\mathbf{e}_\zeta$, $\mathbf{e}_n$ do not coincide. They differ by the rotation caused by the influence of shear deformation. The arbitrary point of the deformed reference axis is described with the local vector (Fig. 4.1) as:

$$\mathbf{r}_c(s) = \mathbf{r}_0(s) + \mathbf{u}(s) = (X(s) + u(s))\,\mathbf{E}_X + (Z(s) + w(s))\,\mathbf{E}_Z, \tag{4.1}$$

where $u(s)$ and $w(s)$ represent the displacements of the centroid axis in X and Z direction, respectively. The arbitrary point of the deformed beam is determined by vector:

$$\mathbf{r}(s) = \mathbf{r}_c(s) + \zeta \mathbf{e}_\zeta(s). \tag{4.2}$$

Reissner's kinematic equations connect strain quantities $(\varepsilon, \gamma, \kappa)$ with kinematic quantities (u, w, φ), and are written as [48]:

$$X' + u' - (1+\varepsilon)\cos\varphi - \gamma \sin\varphi = 0, \tag{4.3}$$

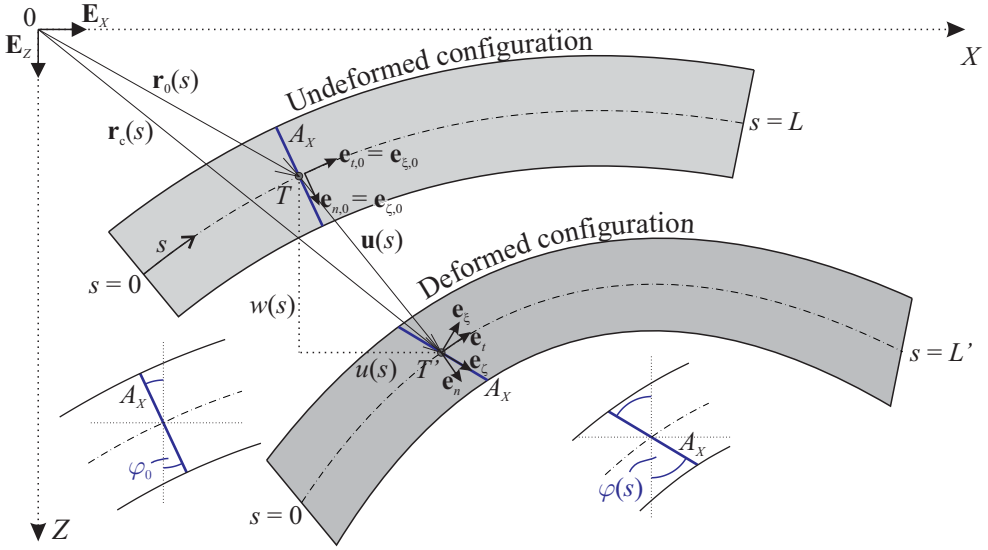

Figure 4.1: Undeformed and deformed configurations of the curved beam.
Slika 4.1: Nedeformirana in deformirana lega ukrivljenega nosilca.

$$Z' + w' + (1+\varepsilon)\sin\varphi - \gamma\cos\varphi = 0, \tag{4.4}$$

$$\varphi' - \kappa_0 - \kappa = 0. \tag{4.5}$$

Here, $()'$ denotes the derivative with respect to s, ε is the extensional strain of the reference axis, φ is the rotation of the cross-section, γ is the shear strain, κ is the pseudo-curvature of the reference axis and κ_0 is the initial curvature of the reference axis.

The kinematic equations for the tapered timber beam are similar to the equation for the curved beam. The initial pseudo-curvature of the reference axis is equal to zero ($\kappa_0 = 0$). The reference axis of the tapered beam is placed at the bottom side of the beam, as seen in Fig. 4.2.

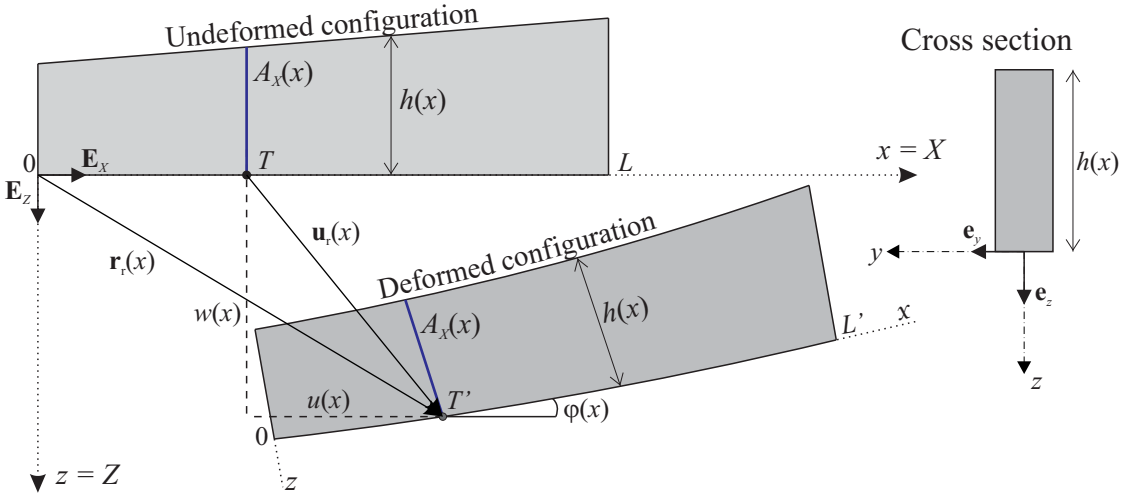

Figure 4.2: Undeformed and deformed configuration of the tapered beam.
Slika 4.2: Nedeformirana in deformirana lega nosilca s spremenljivo višino.

4.2 Equilibrium equations

The equilibrium equations connect the equilibrium generalized internal forces with an external load. Conservative force ($\mathbf{p} = p_X\mathbf{E}_X + p_Z\mathbf{E}_Z$) and moment tractions ($\mathbf{m} = m_Y\mathbf{E}_Y$) are applied along the reference axis. The equilibrium equations are:

$$R'_X + p_X = 0, \tag{4.6}$$

$$R'_Z + p_Z = 0, \tag{4.7}$$

$$M'_Y - (1+\varepsilon)Q + \gamma N + m_Y = 0, \tag{4.8}$$

where R_X and R_Z are the components of the axial and shear force in X and Z direction, respectively, M_Y is equilibrium moment. The equilibrium axial and shear forces, N and Q, are determined as:

$$N = R_X \cos\varphi - R_Z \sin\varphi, \tag{4.9}$$

$$Q = R_X \sin\varphi + R_Z \cos\varphi. \tag{4.10}$$

4.3 Constitutive equations

The last set of equations is needed to connect equilibrium internal forces (N, Q, M_Y) with the deformation quantities $(\varepsilon, \gamma, \kappa)$. The constitutive equations are:

$$N_\mathrm{c} - N = 0, \tag{4.11}$$

$$Q_\mathrm{c} - Q = 0, \tag{4.12}$$

$$M_\mathrm{c} - M_Y = 0, \tag{4.13}$$

where N_c and Q_c are constitutive axial and shear force and M_c is constitutive bending moment. Constitutive quantities $N_\mathrm{c}, Q_\mathrm{c}, M_\mathrm{c}$ are expressed by the normal and shear stress, σ and τ, respectively.

$$N_\mathrm{c} = \int_{A(s)} \sigma\,(s,\eta,\zeta)\,dA, \tag{4.14}$$

$$Q_\mathrm{c} = \int_{A(s)} \tau\,(s,\eta,\zeta)\,dA, \tag{4.15}$$

$$M_\mathrm{c} = \int_{A(s)} \zeta\sigma\,(s,\eta,\zeta)\,dA. \tag{4.16}$$

Here, A denotes the cross-section of the beam. N_c, Q_c and M_c follow the chosen material model defined by the relationships between the longitudinal normal stress σ and mechanical extensional strain D_σ and between shear stress τ and shear strain γ. In general, material models can be defined by the following functions:

$$\sigma(s,\eta,\zeta) = \mathscr{F}\left(D_\sigma(s,\eta,\zeta), T(s,\eta,\zeta), m(s,\eta,\zeta)\right), \tag{4.17}$$

$$\tau(s,\eta,\zeta) = \mathscr{G}\big(\gamma(s,\eta,\zeta), T(s,\eta,\zeta), m(s,\eta,\zeta)\big). \tag{4.18}$$

Usually, functions $\mathscr{F}$ and $\mathscr{G}$ are determined experimentally. With these functions, different material models can be described, for instance, elastic, elasto-plastic, hyper-elastic, visco-elastic, etc. By assuming parabolic distribution of shear stress in a rectangular cross-section and linear shear material model, the calculation of the constitutive shear force yields [47, 95]:

$$Q_{\mathrm{c}}(\gamma(s)) = G(T) A_{\mathrm{s}} \gamma(s), \tag{4.19}$$

where $G(T)$ is the shear modulus and A_{s} is the shear section. Note that the influence of moisture on the shear modulus is neglected and the shear strain is assumed constant over cross-section.

4.3.1 Constitutive law for timber

In the thesis, stress-strain relationship for timber at elevated temperatures is based on the proposal given by Eurocode [17] and Pischl [49]. Eurocode [17] proposes linear relationship in tension and compresion between normal stress σ and mechanical extensional strain D_σ of a longitudinal fibre. Pischl's model [49] additionally considers the plastic hardening in compression. Here, the stress-strain relationship is further modified to also account for the plastic hardening in tension, seen as the dotted line in Fig. 4.3. By doing so, the redistribution od stresses in wood is considered [96–98].

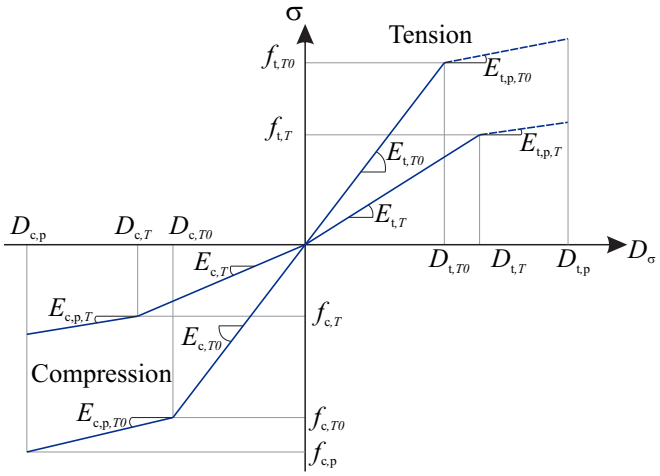

Figure 4.3: Stress-strain relationship for timber at ambient and elevated temperatures.
Slika 4.3: Konstitucijski zakon lesa pri sobni in povišanih temperaturah.

In Fig. 4.3, $D_{i,j}$, $E_{i,j}$ and $f_{i,j}$ ($i = \mathrm{c,t}; j = T, T0$) are the limit elastic strains, the Young's modulus and the strengths of timber in compression (c) and tension (t) at room ($T0$) and elevated temperatures (T), respectively. Similarly, $E_{i,\mathrm{p},j}$ and $f_{i,\mathrm{p},j}$ ($i = \mathrm{c,t}; j = T, T0$) denote the plastic hardening modulus and limit plastic stress, respectively. Temperature dependency of all described parameters is determined by the following rule:

$$X_T = k_T X_{T0}, \tag{4.20}$$

where X_T represents the parameter value at elevated temperature, X_{T0} is the value at room temperature and k_T is temperature dependent reduction factor. Reduction factors $k_{\mathrm{fc},T}, k_{\mathrm{ft},T}, k_{\mathrm{Ec},T}, k_{\mathrm{Et},T}$ for parameters $f_{\mathrm{c},T}, f_{\mathrm{t},T}, E_{\mathrm{c},T}$, $E_{\mathrm{t},T}$ are given in EN 1995-1-2 [17]. Limit strains $D_{\mathrm{c},T}$, $D_{\mathrm{t},T}$ are calculated by the ratios $D_{\mathrm{c},T} = f_{\mathrm{c},T}/E_{\mathrm{c},T}$ and $D_{\mathrm{t},T} = f_{\mathrm{t},T}/E_{\mathrm{t},T}$. To the best of author's knowledge, there are no reduction factors found in the literature for parameters $E_{\mathrm{c,p,T}}$ and $E_{\mathrm{t,p,T}}$. Therefore, the same reduction factors as for modulus of elasticity ($k_{\mathrm{Ec},T}$ and $k_{\mathrm{Et},T}$) are presumed. The limit plastic strain is temperature independent; in compression $D_{\mathrm{c,p}}$ is 3.6 % [99, 100], in tension $D_{\mathrm{t,p}}$ is assumed 1.8%. Reduction factors $k_{\mathrm{fc},T}, k_{\mathrm{ft},T}, k_{\mathrm{Ec},T}, k_{\mathrm{Et},T}$ are shown in Fig. 4.4. At the temperature 300°C, the formation of charcoal occurs and consequently, reductions factors above this temperatures are equal to zero. This means that a layer with temperature above 300°C does not contribute to the load bearing capacity of the cross-section.

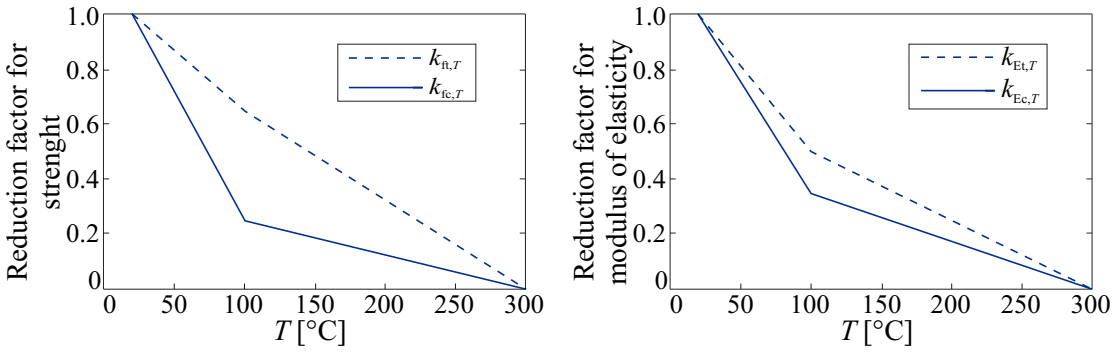

Figure 4.4: Reduction factors for strength and modulus of elasticity of softwood parallel to the grain [17].

Slika 4.4: Redukcijski koeficienti za trdnost in modul elastičnosti za mehki les vzdolžno z vlakni [17].

4.3.2 Additive decomposition of the geometrical strain

When a timber beam is exposed to elevated temperatures and changing humidity, different impacts on the material occur, such as the temperature strain, mechano-sorptive strain and thermal creep strain. In order to implement these impacts in the mechanical model, additive decomposition of geometrical strain increment is introduced [35, 101, 102]. Therefore, the increment of geometrical strain in a random point of the beam $\Delta D(s, \eta, \zeta)$ can be defined as the sum of different increments as:

$$\Delta D = \Delta D_{\mathrm{th}} + \Delta D_{\sigma} + \Delta D_{\mathrm{ms}} + \Delta D_{\mathrm{cr,th}}. \tag{4.21}$$

where ΔD_{th}, ΔD_{σ}, ΔD_{ms} and $\Delta D_{\mathrm{cr,th}}$ are the thermal induced, mechanical, mechano-sorptive and thermal creep strain, respectively. Note that the influence of the increments of these strains on the increment of shear strain is disregarded.

Constitutive relationships to describe different strain increments are presented below.

4.3.2.1 Increment of mechanical strain

The increment of mechanical strain for elasto-plastic materials is equal to the sum of the increments of the elastic and plastic strain: $\Delta D_\sigma = \Delta D_\mathrm{e} + \Delta D_\mathrm{p}$. Considering the additive principle (Eq. (4.21)), the increment of mechanical strain in time step $\left[t^{i-1}, t^i\right]$ can be calculated as:

$$\Delta D_\sigma = \Delta D - \Delta D_\mathrm{th} - \Delta D_\mathrm{ms}. \tag{4.22}$$

Note, that the effects of thermal creep are already implicitly included, if the material model given in EN 1995-1-2 [17] is considered. Therefore, explicit consideration of $\Delta D_\mathrm{cr,th}$ is neglected in Eq. (4.22).

To determine stress and strain state of random extensional fibre at the end of time step $\left[t^{i-1}, t^i\right]$, the auxiliary elastic state $\sigma^{(i)\mathrm{trial}}$ is considered, which does not necessarily correspond to the actual state. The expressions for auxiliary state of bi-linear stress-strain relationship are given in [103, 104]:

$$\sigma^{(i)\mathrm{trial}} = E^i \left(D_\sigma^i - D_\mathrm{p}^{i-1}\right), \tag{4.23}$$

$$D_p^{(i)\mathrm{trial}} = D_p^{(i-1)}, \tag{4.24}$$

$$\alpha^{(i)\mathrm{trial}} = \alpha^{(i-1)}, \tag{4.25}$$

$$f^{(i)\mathrm{trial}} = \left|\sigma^{(i)\mathrm{trial}}\right| - \left[\sigma_\mathrm{Y} + E_\mathrm{p}\alpha^{(i-1)}\right]. \tag{4.26}$$

Above, E is elastic modulus of timber in longitudinal direction, D_p^{i-1} and $\alpha^{(i-1)}$ are the plastic strain and accumulated plastic strain at the beginning of time increment, $f^{(i)\mathrm{trial}}$ is an auxiliary function, σ_Y is the yield stress and E_p is plastic hardening modulus.

If the condition $f^{(i)\mathrm{trial}} \leq 0$ is satisfied, then the auxiliary state corresponds to the actual stress and strain state at the end of time increment $\left[t^{i-1}, t^i\right]$. In this situation, only elastic strains occur. Hence:

$$\sigma^{(i)} = \sigma^{(i)\mathrm{trial}}, \tag{4.27}$$

$$D_\mathrm{p}^{(i)} = D_\mathrm{p}^{(i)\mathrm{trial}}, \tag{4.28}$$

$$\alpha^{(i)} = \alpha^{(i)\mathrm{trial}}. \tag{4.29}$$

Plastic step occurs when $f^{(i)\mathrm{trial}} > 0$. In this case plastic strain increment $\Delta\alpha$ is introduced and calculated as:

$$\Delta\alpha = \frac{f^{(i)\mathrm{trial}}}{E + E_\mathrm{p}}. \tag{4.30}$$

Stress-strain state in the plastic step is determined with the following equations:

$$\sigma^{(i)} = \sigma^{(i)\mathrm{trial}} - \Delta\alpha\ E\ \mathrm{sign}\left(\sigma^{(i)\mathrm{trial}}\right), \tag{4.31}$$

$$D_\mathrm{p}^{(i)} = D_\mathrm{p}^{(i)\mathrm{trial}} + \Delta\alpha\ \mathrm{sign}\left(\sigma^{(i)\mathrm{trial}}\right), \tag{4.32}$$

$$\alpha^{(i)} = \alpha^{(i)\mathrm{trial}} + \Delta\alpha. \tag{4.33}$$

4.3.2.2 Thermal strain

The thermal induced strain of timber can be calculated by the linear relationship between the coefficient of thermal expansion α_T and temperature [105] as:

$$D_{\text{th}} = \alpha_T T = 5 \cdot 10^{-6} T. \tag{4.34}$$

The increment of thermal strain in time step $\left[t^{i-1}, t^i\right]$ is calculated from the difference between thermal strains from the current and the previous time step as:

$$\Delta D_{\text{th}} = D_{\text{th}}^i(T^i) - D_{\text{th}}^{i-1}(T^{i-1}). \tag{4.35}$$

4.3.2.3 Mechano-sorptive strain

The increment of mechano-sorptive strain is expressed as [41]:

$$\Delta D_{\text{ms}} = \sigma^{(i)} \Phi^{\infty} \left(1 - e^{-c|\Delta m|}\right), \tag{4.36}$$

where c is a parameter different for sorption and desorption ($c^+ \neq c^-$), Φ^{∞} is the reference compliance. Variable Δm describes the change in moisture content and is within time step $\left[t^{i-1}, t^i\right]$ determined as:

$$\Delta m = m^i - m^{i-1}. \tag{4.37}$$

In general, larger variation of moisture content in wood is observed in wood exposed to changing environmental humidity compared to wood exposed to fire. Consequently, the influence of mechano-sorptive strain on the mechanical behaviour of timber members is more significant in changing environmental humidity than in fire. For this reason, the impact of mechano-sorptive strain is disregarded in the thesis.

4.3.3 Boundary conditions

Kinematic (Eqs. (4.3)-(4.5)), equilibrium (Eqs. (4.6)-(4.8)) and constitutive equations (Eqs. (4.11)-(4.13)) represent a system of 6 linear first order differential equations and 3 algebraic equations. To determine the solution of the differential equations, boundary conditions need to be given. Boundary conditions are divided in natural or Neumann and essential or Dirichlet boundary conditions. Natural boundary conditions are represented by the generalized boundary point forces, while the essential boundary conditions consist of the generalized boundary displacements.

$s = 0$:

$$S_1 + R_X(0) = 0 \qquad \text{or} \qquad u(0) = u_1, \tag{4.38}$$

$$S_2 + R_Z(0) = 0 \qquad \text{or} \qquad w(0) = u_2, \tag{4.39}$$

$$S_3 + M_Y(0) = 0 \qquad \text{or} \qquad \varphi(0) = u_3, \tag{4.40}$$

$s = L$:

$$S_4 - R_X(L) = 0 \qquad \text{or} \qquad u(L) = u_4, \tag{4.41}$$

$$S_5 - R_Z(L) = 0 \qquad \text{or} \qquad w(L) = u_5, \tag{4.42}$$

$$S_6 - M_Y(L) = 0 \qquad \text{or} \qquad \varphi(L) = u_6, \tag{4.43}$$

where u_j, $j = 1, 2, ..., 6$, denotes the prescribed generalized boundary displacement and S_j, $j = 1, 2, ..., 6$, are the generalized boundary forces. The governing equations for the curved timber beam are presented in Box 4.1.

Box 4.1.: Governing equations for curved timber beam

Kinematic equations:

$$X' + u' - (1+\varepsilon)\cos\varphi - \gamma\sin\varphi = 0, \tag{4.44}$$

$$Z' + w' + (1+\varepsilon)\sin\varphi - \gamma\cos\varphi = 0, \tag{4.45}$$

$$\varphi' - \kappa_0 - \kappa = 0. \tag{4.46}$$

Equilibrium equations:

$$R'_X + p_X = 0, \tag{4.47}$$

$$R'_Z + p_Z = 0, \tag{4.48}$$

$$M'_Y - (1+\varepsilon)Q + \gamma N + m_Y = 0, \tag{4.49}$$

$$N = R_X\cos\varphi - R_Z\sin\varphi, \tag{4.50}$$

$$Q = R_X\sin\varphi + R_Z\cos\varphi. \tag{4.51}$$

Constitutive equations:

$$N_\mathrm{c} - N = 0, \tag{4.52}$$

$$Q_\mathrm{c} - Q = 0, \tag{4.53}$$

$$M_\mathrm{c} - M_Y = 0. \tag{4.54}$$

Boundary conditions:

$s = 0$:

$$S_1 + R_X(0) = 0 \quad \text{or} \quad u(0) = u_1, \tag{4.55}$$

$$S_2 + R_Z(0) = 0 \quad \text{or} \quad w(0) = u_2, \tag{4.56}$$

$$S_3 + M_Y(0) = 0 \quad \text{or} \quad \varphi(0) = u_3, \tag{4.57}$$

$s = L$:

$$S_4 - R_X(L) = 0 \quad \text{or} \quad u(L) = u_4, \tag{4.58}$$

$$S_5 - R_Z(L) = 0 \quad \text{or} \quad w(L) = u_5, \tag{4.59}$$

$$S_6 - M_Y(L) = 0 \quad \text{or} \quad \varphi(L) = u_6, \tag{4.60}$$

Basic unknowns: $\varepsilon, \kappa, \gamma, u, w, \varphi, R_X, R_Z, M_Y$.

4.4 Numerical solution of the system

The system of algebraic-differential equations presented in Box 4.1 can be solved analytically only for special cases at room temperatures. In the presented mechanical model, geometrical and material non-linearity is encountered. Consequently, the analytical solution cannot be obtained. Instead, the system of equations is solved numerically with the finite element method (FEM). Strain based finite element [39] is embedded, its formulation is built on the interpolation of the deformation quantities. The derivation of strain based finite element for curved beam was introduced in the PhD thesis of Čas [47]. The Galerkin finite element method was used. The same method is used in the present work. Since the basic equations here are similar to those given in [47], only basic steps of the finite element formulation are presented below. Basic equations for the finite element method are derived from the principle of virtual work [47], written as:

$$\begin{aligned}\delta W = \int_0^L N_c \delta\varepsilon \, ds + \int_0^L Q_c \delta\gamma \, ds + \int_0^L M_c \delta\kappa \, ds - \\ \int_0^L p_X \delta u \, ds - \int_0^L p_Z \delta w \, ds - \int_0^L m_Y \delta\varphi \, ds - \sum_{k=1}^{6} S_k \delta u_k = 0,\end{aligned} \tag{4.61}$$

where $\delta u, \delta w$ are virtual displacements, $\delta\varphi$ is virtual rotation, $\delta\varepsilon, \delta\gamma, \delta\kappa$ are virtual strains and δu_k are the virtual generalized boundary displacements at end points of the beam [50]:

$$\delta u_1 = \delta u(0), \;\; \delta u_2 = \delta w(0), \;\; \delta u_3 = \delta\varphi(0), \;\; \delta u_4 = \delta u(L), \;\; \delta u_5 = \delta w(L), \;\; \delta u_6 = \delta\varphi(L). \tag{4.62}$$

By integrating Eqs.(4.3)–(4.7) and evaluating them at $s = L$, the kinematic boundary quantities $u(0), w(0), \varphi(0), u(L), w(L), \varphi(L)$ and generalized boundary forces $R_X(0), R_Z(0), M_Y(0), R_X(L), R_Z(L), M_Y(L)$ are linked together. The modified principle of virtual work is obtained by inserting these constraints into the principle of virtual work (Eq.(4.61)) [47]:

$$\begin{aligned}\delta W^* = \int_0^L \Big((N_c - N)\,\delta\varepsilon + (Q_c - Q)\,\delta\gamma + (M_c - M_Y)\,\delta\kappa \Big) ds + \\ + \left(u(L) - u(0) + \Delta X_L - \int_0^L \Big((1+\varepsilon)\cos\varphi + \gamma\sin\varphi \Big) ds \right) \delta R_X(0) + \\ + \left(w(L) - w(0) + \Delta Z_L - \int_0^L \Big((1+\varepsilon)\sin\varphi - \gamma\cos\varphi \Big) ds \right) \delta R_Z(0) + \\ + \left(\varphi(L) - \varphi(0) - \int_0^L (\kappa + \kappa_0)\, ds \right) \delta M_Y(0) + \\ + (S_1 + R_X(0))\,\delta u_1 + (S_2 + R_Z(0))\,\delta u_2 + (S_3 + M_Y(0))\,\delta u_3 + \\ + (S_4 - R_X(L))\,\delta u_4 + (S_5 - R_Z(L))\,\delta u_5 + (S_6 - M_Y(L))\,\delta u_6 = 0.\end{aligned} \tag{4.63}$$

Deformation quantities $\varepsilon, \gamma, \kappa$, generalized boundary forces $R_X(0), R_Z(0), M_Y(0)$ and boundary kinematic quantities $u(0), w(0), \varphi(0), u(L), w(L), \varphi(L)$ are the basic unknowns of the problem. The deformation quantities $\varepsilon, \gamma, \kappa$ depend on arc-length parameter s and are interpolated over finite element length. Lagrangian interpolation through equidistant nodes is used:

$$\varepsilon(s) = \sum_{m=1}^{M} P_m(s)\varepsilon_m, \tag{4.64}$$

$$\gamma(s) = \sum_{m=1}^{M} P_m(s)\gamma_m, \tag{4.65}$$

$$\kappa(s) = \sum_{m=1}^{M} P_m(s)\kappa_m, \tag{4.66}$$

where $\varepsilon_m, \gamma_m, \kappa_m$ are unknown nodal values of extensional strain, shear strain and pseudo-curvature, respectively. $P_m (m = 1, 2, ..., M)$ are the Lagrangian polynomials of order $(M - 1)$. The variations of Eqs. (4.64)–(4.66) give:

$$\delta\varepsilon(s) = \sum_{m=1}^{M} P_m(s)\delta\varepsilon_m, \tag{4.67}$$

$$\delta\gamma(s) = \sum_{m=1}^{M} P_m(s)\delta\gamma_m, \tag{4.68}$$

$$\delta\kappa(s) = \sum_{m=1}^{M} P_m(s)\delta\kappa_m. \tag{4.69}$$

The Euler-Lagrange equations of the finite element are obtained by inserting Eqs. (4.64)-(4.69) in the functional (4.63) and setting the coefficients of the independent nodal variations $\delta\varepsilon_m, \delta\gamma_m, \delta\kappa_m, \delta R_X(0)$, $\delta R_Z(0), \delta M_Y(0)$ and δu_i $(i = 1, 2, ..., 6)$ to zero [47, 50]:

$$g_m = \int_0^L (N_c - N)\, P_m ds = 0, \tag{4.70}$$

$$g_{M+m} = \int_0^L (Q_c - Q)\, P_m ds = 0, \tag{4.71}$$

$$g_{2M+m} = \int_0^L (M_c - M_Y)\, P_m ds = 0, \tag{4.72}$$

$$g_{3M+1} = u(L) - u(0) + \Delta X_L - \int_0^L ((1+\varepsilon)\cos\varphi + \gamma\sin\varphi)\, ds = 0, \tag{4.73}$$

$$g_{3M+2} = w(L) - w(0) + \Delta Z_L - \int_0^L ((1+\varepsilon)\sin\varphi - \gamma\cos\varphi)\, ds = 0, \tag{4.74}$$

$$g_{3M+3} = \varphi(L) - \varphi(0) - \int_0^L (\kappa + \kappa_0)\, ds = 0, \tag{4.75}$$

$$g_{3M+4} = S_1 + R_X(0) = 0, \tag{4.76}$$

$$g_{3M+5} = S_2 + R_Z(0) = 0, \tag{4.77}$$

$$g_{3M+6} = S_3 + M_Y(0) = 0, \tag{4.78}$$

$$g_{3M+7} = S_4 - R_X(0) + \int_0^L p_X ds = 0, \tag{4.79}$$

$$g_{3M+8} = S_5 - R_Z(0) + \int_0^L p_Z ds = 0, \tag{4.80}$$

$$g_{3M+9} = S_6 - M_Y(0) - \int_0^L ((1+\varepsilon)Q - \gamma N - m_Y)\, ds = 0. \tag{4.81}$$

Eqs(4.70)–(4.81) constitute a system of $3M+9$ non-linear algebraic equations for $3M+9$ unknowns. There are $3M+3$ internal degrees of freedom $\varepsilon_m(m=1,...,M), \gamma_m(m=1,...,M), \kappa_m(m=1,...,M)$, $R_X(0), R_Z(0), M_Y(0)$ and six external degrees of freedom $u(0), w(0), \varphi(0), u(L), w(L), \varphi(L)$ of the finite element. Integrals in Eqs. (4.70)-(4.81) are calculated with the Gauss or Lobatto numerical integration scheme. Due to more efficient numerical calculation, the internal degrees of freedom are condensed, while the external degrees are combined in a structure equation.

$$\mathbf{G}(\mathbf{x}^i, \lambda^i, T^i, m^i) = 0, \tag{4.82}$$

where $\mathbf{x}^i$ is a vector of generalized displacements at time t^i and is composed of nodal displacements and rotations of curved beam, λ^i is the loading factor, T^i is the temperature field and m^i the moisture field. The algebraic system of non-linear equations is solved by the Newton increment-iterative method. The iterative corrections of generalized nodal displacements $\delta\mathbf{x}^i$, for $h = 1, 2, ...$ to the desired precision, are determined within time step $\left[t^{i-1}, t^i\right]$ at known temperature field T^i, moisture field m^i and loading factor λ^i.

$$\Delta_x\mathbf{G}(\mathbf{x}^{i-1} + \Delta\mathbf{x}_h^i, \lambda^i, T^i, m^i) = -\mathbf{G}(\mathbf{x}^{i-1} + \Delta\mathbf{x}_h^i, \lambda^i, T^i, m^i), \tag{4.83}$$

$$\Delta\mathbf{x}_{h+1}^i = \Delta\mathbf{x}_h^i + \delta\mathbf{x}_{h+1}^i, \tag{4.84}$$

The failure of the structure (fire resistance) is determined when the tangent stiffness matrix of the structure $\Delta_x\mathbf{G} = \mathbf{K}_{T,h}^i$ becomes singular during the iterative procedure. The corresponding time is recognized as critical time t_{cr}. In the context of the presented mechanical model, the material failure, which occurs when the determinant of the tangent constitutive matrix of the beam cross-section becomes zero [50], does not automatically imply the singularity of the tangent stiffness matrix of the structure. For this reason, the material failure is examined separately. As well known, the double criterion to determine the fire resistance can be avoided by the proper selection of integration and interpolation points [39].

4.5 Post processing - stresses perpendicular to grain

In curved timber beams considerable stresses perpendicular to the grain may occur, which can result in the possible failure of the beam. In the thesis, one dimensional finite element model is employed, meaning that only longitudinal stresses are directly incorporated in the calculation. Therefore, the stresses perpendicular to the grain are post processed from the longitudinal stresses via known mechanical relationships. In the following subsection the equations for the normal stress perpendicular to the grain (radial stress) for curved beam are presented. The derivation of equations is given in [95, 106].

To derive the expression for the radial stress in a curved beam, a slice of beam with section A' is examined (Fig. 4.5). The tensile forces of magnitude $\overline{N}$ are determined by the integration of the longitudinal normal stresses over A':

$$\overline{N} = \int_{A'} \sigma_{\xi\xi} dA. \tag{4.85}$$

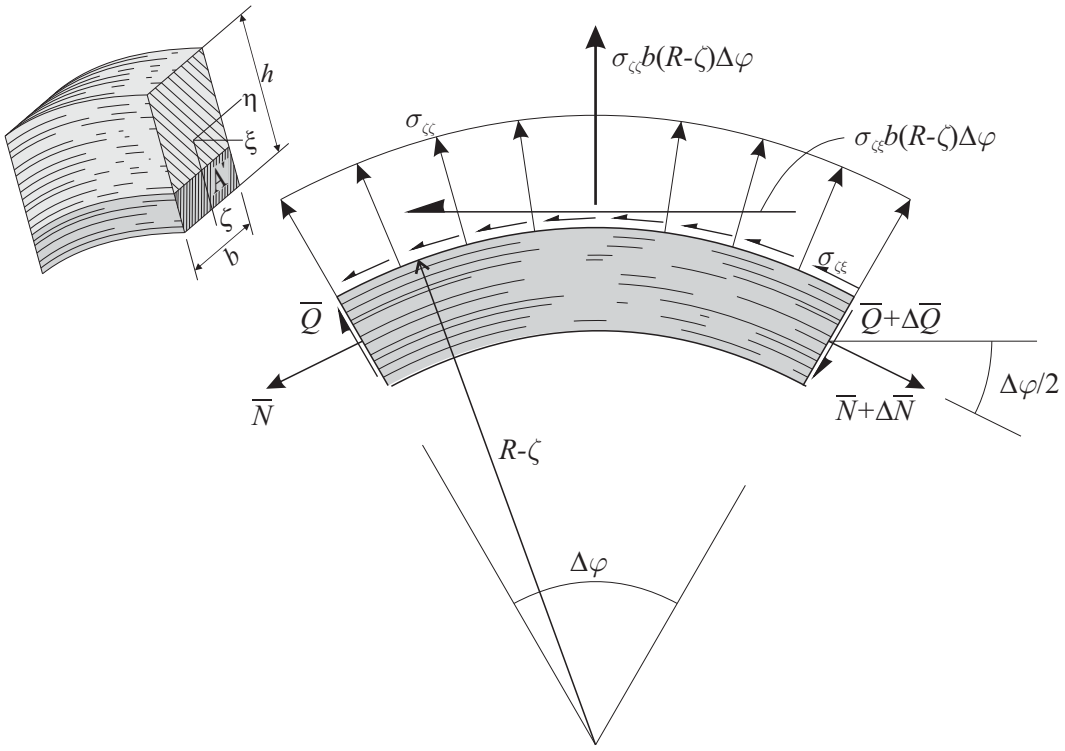

Figure 4.5: Forces working on the part of the beam with cross-sectional area A' [95].
Slika 4.5: Sile, ki delujejo na delu nosilca s prečnim prerezom A' [95].

Likewise, the shear stresses developed on A' generate a force $\overline{Q}$ parallel to the cross-section:

$$\overline{Q} = \int_{A'} \sigma_{\xi\zeta} dA. \tag{4.86}$$

It is clear that $\overline{N}$ and $\overline{Q}$ yield to N and Q, if the integration is performed on the entire cross-section. As seen from Fig. 4.5, a resulting force $\sigma_{\zeta\zeta} b(R-\zeta)\Delta\varphi$ must act on the surface at $R-\zeta$ to balance the vertical components of $\overline{N}$ and $\overline{Q}$. Here, $\sigma_{\zeta\zeta}$ is considered as the average radial stress on the element. It is determined by the equilibrium of forces in vertical direction:

$$\left(2\overline{N} + \Delta\overline{N}\right) \sin\frac{\Delta\varphi}{2} - \sigma_{\zeta\zeta} b(R-\zeta)\Delta\varphi + \left(\overline{Q} + \Delta\overline{Q} - \overline{Q}\right) \cos\frac{\Delta\varphi}{2} = 0. \tag{4.87}$$

In the limit, where $\Delta\varphi$ approaches zero, this leads to:

$$\frac{\overline{N}}{R} + \frac{\partial\overline{Q}}{\partial\xi} - \sigma_{\zeta\zeta} b\left(1 - \frac{\zeta}{R}\right) = 0. \tag{4.88}$$

Therefore,

$$\sigma_{\zeta\zeta} = \frac{1}{b\left(1 - \frac{\zeta}{R}\right)} \left(\frac{\overline{N}}{R} + \frac{\partial\overline{Q}}{\partial\xi}\right), \tag{4.89}$$

where the following approximation can be introduced:

$$\overline{Q} = Q\frac{A'}{A}. \tag{4.90}$$

Finally, the term for the radial stress can be written as:

$$\sigma_{\zeta\zeta}(\zeta) = \frac{1}{b\left(1-\frac{\zeta}{R}\right)}\left(\frac{\overline{N}}{R}+\frac{\partial Q}{\partial \xi}\frac{A'}{A}\right). \tag{4.91}$$

4.6 Validation and verification of the mechanical model

Several cases are demonstrated in this section with the purpose to validate and verify the proposed mechanical model. Firstly, the mechanical formulation of the tapered beam is verified with the numerical results given by [106]. Moreover, the convergence of the presented strain-based finite element is investigated. In the second case, verification of the mechanical model for curved timber beam is performed, where also post-processed radial stresses in the beam are determined. In the last case, validation of the mechanical model at elevated temperatures is carried out.

4.6.1 Verification of tapered beam

In this study, the verification of mechanical formulation for tapered beam is conducted. The results carried out with the presented mechanical model are compared to the numerical results given by Stanek and Turk [106]. Vertical displacements at the free end of the tapered cantilever beam (Fig. 4.6) are compared. The beam is subjected to the point load F = 4 kN at the free end. Beam length is L = 10 m. Cross-section is rectangular, the height is following square function $h(x) = 1-0.15x+0.0075x^2$, the width is constant b = 200 mm. The beam height at the restrained end is $h(x = 0)$ = 1000 mm and at the free end $h(x = 10)$ = 250 mm. The elastic modulus of material is E = 2000 kN/cm^2, the shear modulus is G = 500 kN/cm^2.

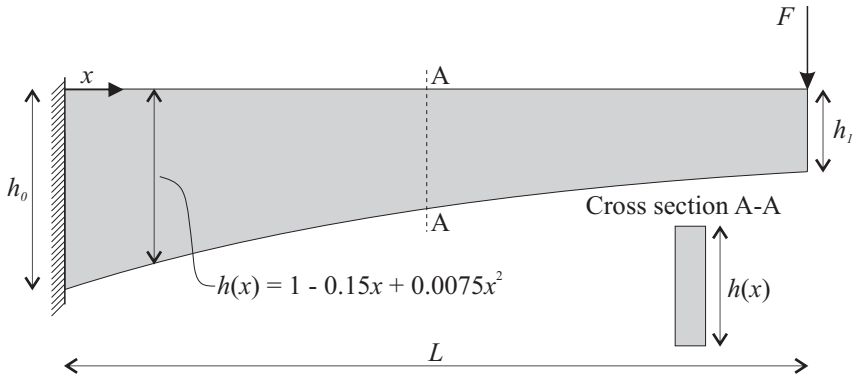

Figure 4.6: Tapered beam with the height following the square function.
Slika 4.6: Nosilec s spremenljivo višino, ki se spreminja po kvadratni paraboli.

Firstly, the convergence of the presented strain-based finite elements is examined. The number of interpolation and integration points as well as the number of finite elements is varied. The number of interpolation points is equal to the number of integration points ($n_g = n$). Gaussian type of numerical integration is applied. Finite elements with different number of interpolation points (i = 3, 4, 5) are

denoted as E_i. The beam is divided in 2, 4, 8 and 16 finite elements of equal length. Relative error *rer* is introduced to evaluate the convergence of numerical solutions. As reference solution, the results with sixteen finite elements interpolated with 4$^{\text{th}}$ order of Lagrangian polynomials (E_5^{16}) are taken. Relative error is defined as:

$$rer = \frac{x_{E_i^j} - x_{E_5^{16}}}{x_{E_5^{16}}}, \tag{4.92}$$

where $x_{E_i^j}$ denotes the result for an observed quantity obtained with the current number of finite elements, $j = n_{\text{el}}$, and with the n^{th} degree polynomial interpolation, $i = n + 1$. Reference value $x_{E_5^{16}}$ is determined by comparing the result for the analysis with 8 and 16 finite elements type E_5, where the results do not differ by more than 1 ‰.

Relative errors as a function of different types and numbers of finite elements are presented in Fig. 4.7. The variables of interest are the vertical and horizontal displacement at the free end of the cantilever beam, w_{END} and u_{END}, respectively. As seen, the relative errors are small for all cases. The maximum value does not exceed 0.2 %. The relative error decreases by increasing the number of finite elements and interpolation/integration points. The error stabilizes using 4 elements type E_3 or higher, meaning that using this type of element E_3^4 already gives satisfactory results. However, the difference in the computational time when using 2$^{\text{nd}}$ (E_3) or 4$^{\text{th}}$order (E_5) of Lagrangian polynomials is not significant. Therefore, the finite element type E_5 will be employed in further analyses and parametric studies.

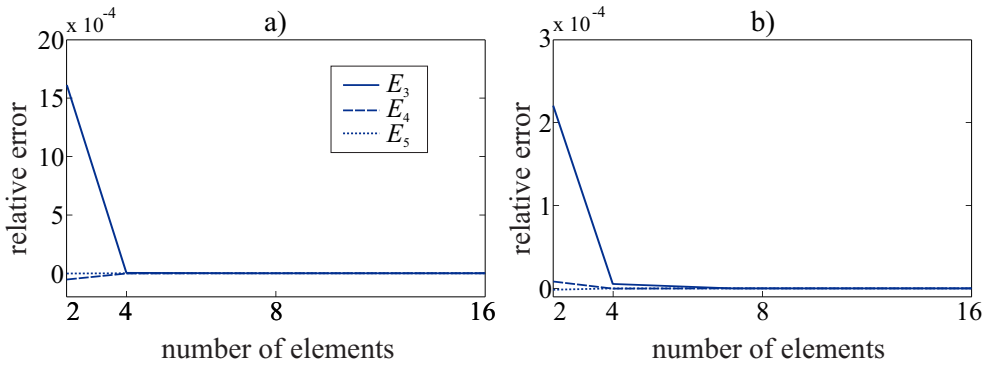

Figure 4.7: a) Relative error for vertical displacement w_{END}. b) Relative error for horizontal displacement u_{END}.

Slika 4.7: a) Relativna napaka za vertikalni pomik w_{END}. b) Relativna napaka za horizontalni pomik u_{END}.

Next, the solution for the vertical displacement at the free end of the cantilever beam ($w_{E_5^4}$) with the displacement calculated by Stanek and Turk [106] is compared. For their exact solution, a two-dimensional finite element mesh was applied where isotropic plane finite elements were employed. The analysis was conducted in computer software Lusas [107]. The comparison is presented in Table 4.1. The presented one-dimensional beam model almost perfectly approximates two-dimensional model, since minimal difference of 0.06 % is observed. Therefore, the presented mechanical model is suitable for the analysis of tapered beam at room temperature.

Table 4.1: Vertical displacements calculated with the presented model and the 2D plane stress FEM model [106].

Preglednica 4.1: Vertikalni pomiki izračunani s predstavljenim modelom in dvodimenzijskim modelom končnih elementov, ki temelji na ravninskem napetostnem stanju [106].

Model	Present	2D model
Displacement [mm]	23.45	23.44
Deviation [%]	0.06	\

4.6.2 Verification of curved beam

The verification of the mechanical model formulation for curved beam is presented in this section. Verification is done by comparing the results calculated with the presented mechanical model with the results from the 2D FEM model, conducted in Comsol software [108], where isotropic and orthotropic material is considered. The compared quantities are mid-span displacement, longitudinal stresses and post processed stress perpendicular to the grain. The span of the considered curved beam is 15 m, the radius is R = 7.5 m and on both ends the beam is supported by pinned supports. The cross-section is b/h = 200/800 mm. The beam is loaded with uniform load q = 50 kN/m acting in global Z direction as seen in Fig. 4.8. Further on, the beam is composed of glulam class GL28c. The parameters for the presented mechanical model and 2D FEM model with isotropic material are: the characteristic bending strength $f_{\mathrm{m,k}}$ = 2.8 kN/cm^2, the elastic modulus $E_{0,\mathrm{mean}}$ = 1260kN/cm^2, the characteristic strength perpendicular to the grain $f_{\mathrm{t,90,k}}$ = 0.04 kN/cm^2, Poisson's ratio ν = 0.25 and shear modulus G = 504 kN/cm^2. The parameters for 2D FEM model with orthotropic material are [109]: E_L = 1260 kN/cm^2, E_T = 54 kN/cm^2, E_R = 100 kN/cm^2, G_{TL} = 80 kN/cm^2, G_{LR} = 76 kN/cm^2, G_{TR} = 4 kN/cm^2, ν_{TL} = 0.03, ν_{LR} = 0.422, ν_{TR} = 0.25, where L, T, R represent the wood material directions (L – longitudinal, T – tangential, R – radial).

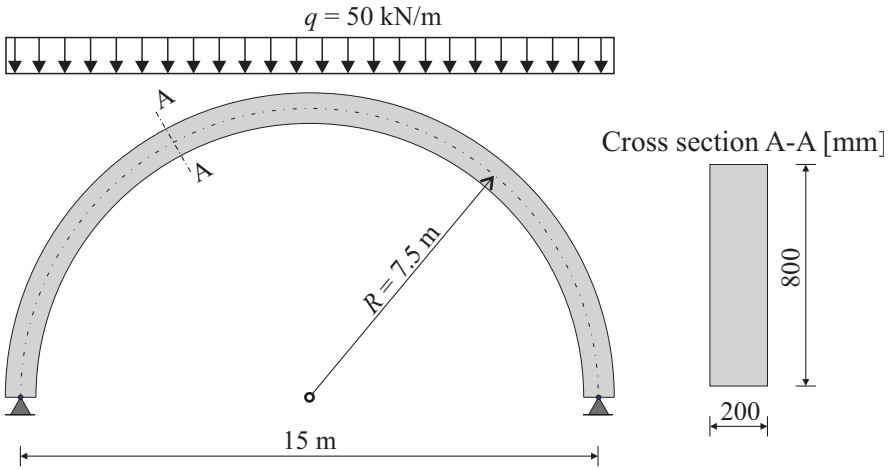

Figure 4.8: Geometry and load for curved beam.

Slika 4.8: Geometrija in obtežba za ukrivljen nosilec.

For the 2D analysis the entire beam domain is discretized into 5763 quadrilateral isoparametric plane stress finite elements as presented in Fig. 4.9. For the analysis with the presented mechanical model the beam is modelled with 16 one-dimensional finite elements.

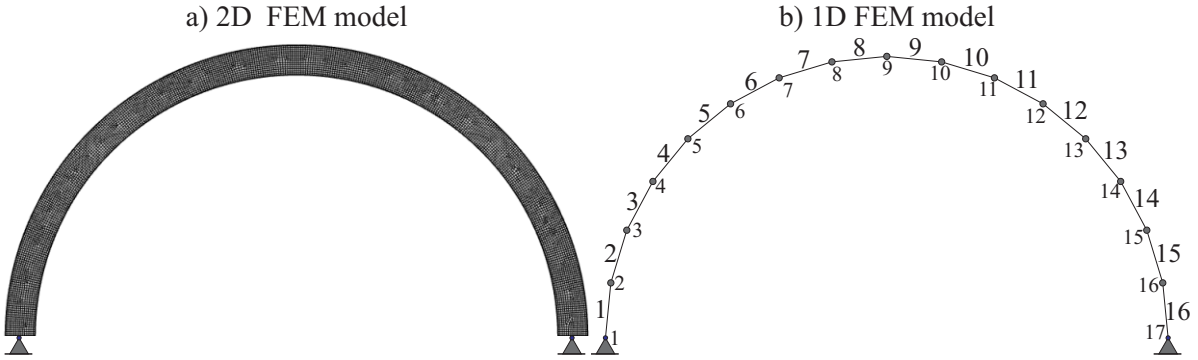

Figure 4.9: Beam discretisation for: a) analysis with 2D finite elements. b) analysis with 1D finite elements.

Slika 4.9: Diskretizacija nosilca za: a) analizo z 2D končnimi elementi. b) analizo z 1D končnimi elementi.

The calculated mid-span displacements with all three models are presented in Table 4.2. As observed, results conducted with the presented mechanical model and 2D FEM model with isotropic material agree well. However, they both distinguish from the mid-span displacement calculated with 2D FEM model (orthotropic material) by more than 6 %. When timber is modelled as isotropic material, a certain error is expected, since the influence of the orthotropic nature of timber on the beam deformation is considered only with the shear modulus or Poisson's ratio for one material direction.

Table 4.2: Mid-span displacements calculated with the presented mechanical model and Comsol software.

Preglednica 4.2: Vertikalni pomiki na sredini razpona, izračunani s predstavljenim mehanskim modelom in programskim orodjem Comsol.

Model	Present 1D model	2D isotropic	2D orthotropic
Mid-span displacement [mm]	24.31	24.33	26.06
Deviation [%]	6.7	6.6	\

In Fig. 4.10 the distribution of stresses at the mid-span of the beam is shown. The distribution of the longitudinal normal stress $\sigma_{\xi\xi}$ is practically identical for all three models used in the analysis (Fig. 4.10a). The distribution of the post-processed normal stress perpendicular to the grain is slightly different from the distribution of normal stress perpendicular to the grain obtained with the 2D FEM model with isotropic and orthotropic material (Fig. 4.10b). However, the magnitude is the same and reaches 0.026 $\mathrm{kN/cm^2}$. This means that the failure criterion due to the exceeded tension stresses perpendicular to the grain is not jeopardized ($f_{\mathrm{t,90,k}} = 0.04\ \mathrm{kN/cm^2} \geq 0.026\ \mathrm{kN/cm^2}$). Therefore, the post-processed normal stresses perpendicular to the grain can sufficiently describe the normal stresses perpendicular to the grain calculated

with the 2D FEM model.

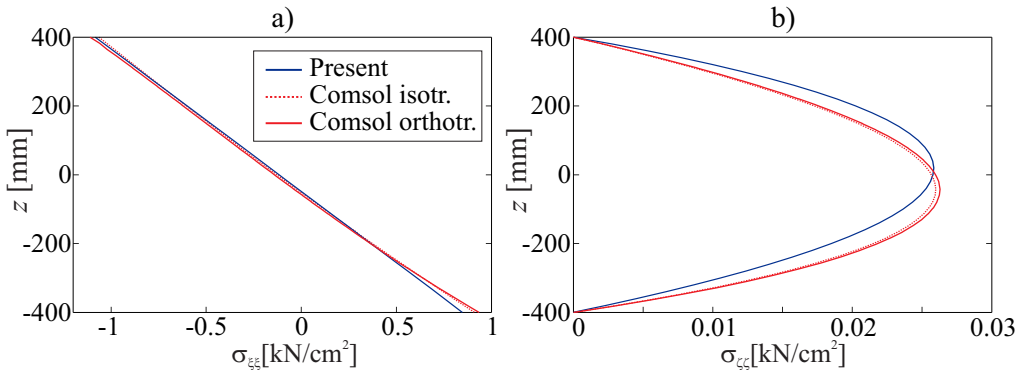

Figure 4.10: a) Distribution of normal longitudinal stress $\sigma_{\xi\xi}$. b) Distribution of normal stress perpendicular to grain $\sigma_{\zeta\zeta}$.
Slika 4.10: a) Razpored normalne vzdolžne napetosti $\sigma_{\xi\xi}$. b) Razpored normalne napetosti pravokotno na vlakna $\sigma_{\zeta\zeta}$.

4.6.3 Validation of the mechanical model at elevated temperatures

Validation of the presented mechanical model at elevated temperatures is done by comparing numerical results to experimental results given by Zhang et al. [29]. In the experiment, fire resistance on straight simply supported timber beam exposed to standard ISO fire from three sides was investigated. Douglas fir was used as wood material. The cross-section of the beam was $b/h = 100\times200$ mm, the span was 3.6 m. Two point loads $F = 8.25$ kN were applied on the beam as seen in Fig. 4.11.

Firstly, the heat and moisture analysis was conducted to determine temperature and moisture field of the considered beam during fire. The basic input data for the thermal analysis are presented on the right hand side of Fig. 4.11. The cross-section was discretized into 1600 finite elements, giving the element size of 2.5×2.5 mm. The calculated and measured temperatures are shown in Fig. 4.12, where the temperature development in point P1 is presented. The comparison reveals good agreement. Minor discrepancies are observed at the end of the simulation, where the calculated temperatures are around 7 °C lower. However, this is a negligible deviation.

In the mechanical analysis, the beam is modelled with six finite elements type E_5. The measured data for the modulus of elasticity at room temperature was $E_{\mathrm{t},T0} = E_{\mathrm{c},T0} = 1321$ kN/cm^2 [29]. According to Eurocode [110], this modulus corresponds to timber class C35 for softwoods. Characteristic tension and compression strengths for this timber class are $f_{\mathrm{t},T0} = 2.1$ kN/cm^2 and $f_{\mathrm{c},T0} = 2.5$ kN/cm^2, respectively. Other parameters for the stress-strain relationship are: $D_{\mathrm{t},T0} = 0.0016$, $D_{\mathrm{c},T0} = 0.0019$, $D_{\mathrm{t,p}} = 0.018$, $D_{\mathrm{c,p}} = 0.035$, $E_{\mathrm{c,p},T0} = E_{\mathrm{t,p},T0} = 100$ kN/cm^2.

Fig. 4.13 demonstrates the result of the mechanical analysis. Calculated mid-span displacements are compared to the measured one. Failure time in the simulation occurs at 27.04 min where the mid-span displacement is 115.7 mm. In the experiment, failure time takes place at 26.9 min and the mid-span displacement is 117 mm. As observed, the results at failure time are almost identical. Small differences (±7 mm) are noticed in the time area $t \in [1\ 24]$ min. Still, the numerical results correspond well to

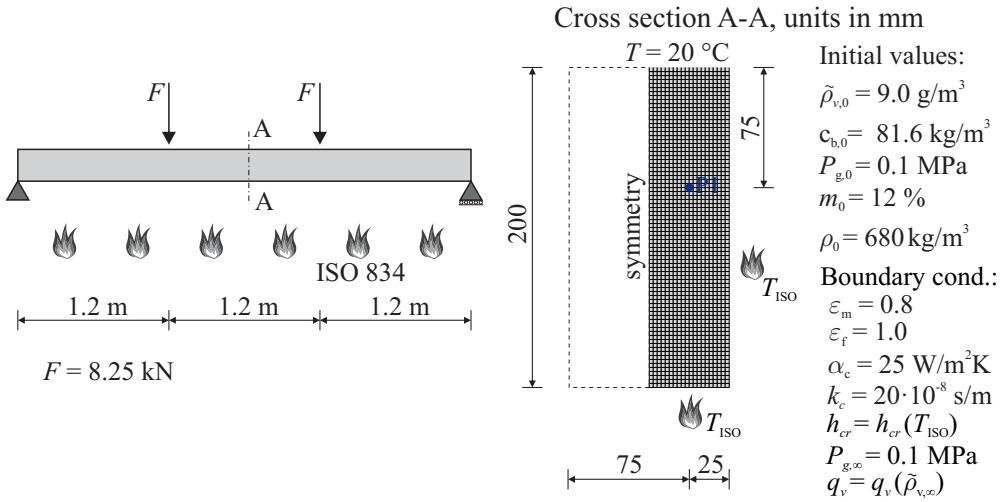

Figure 4.11: Presentation of the considered beam, cross-section, initial values, boundary conditions and 2D finite element mesh for the heat and moisture analysis.

Slika 4.11: Predstavitev obravnavanega nosilca, prečni prerez, začetni in robni pogoji ter mreža končnih elementov.

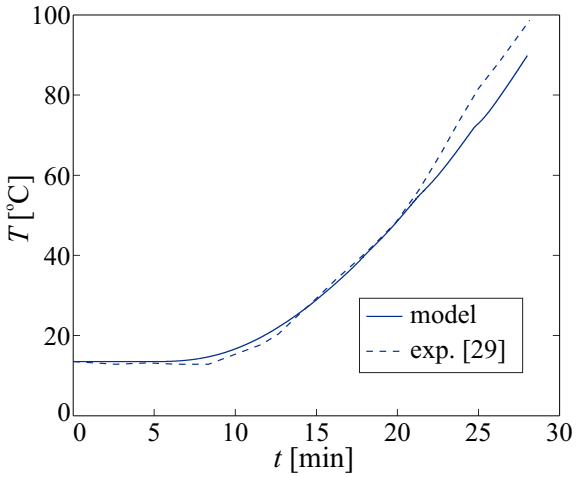

Figure 4.12: Comparison between calculated and measured temperature development in point P1.

Slika 4.12: Primerjava izračunanega in izmerjenega razvoja temperature v točki P1.

the measured displacements. Therefore, the mechanical model is capable to accurately determine the behaviour of timber beam exposed to fire.

In addition to this case, the distribution of stresses at different times at beam mid-span (x = 1.8 m) are presented (Fig. 4.14). The highest stresses are observed at the failure time t = 27 min. In tension, the maximum stress is 2.57 kN/cm^2, in compression it is 3.12 kN/cm^2. At the beginning of the simulation, the stresses are uniformly distributed along the cross-section width. At higher times the redistribution of stresses can be observed. This occurs due to the increased wood temperatures and charring of wood at the exposed edge of the cross-section, which results in reduced material strength. This is particularly apparent at failure time, where, in the cross-section area close to the exposed edge, the stresses are equal

to zero. For this reason, the cross-section of the intact wood which provides load bearing capacity is reduced. In order to satisfy the equilibrium between internal forces and external load (Eqs.(4.6)-(4.8)), the area of higher tension and compression stresses is formed in the less heated part of the cross-section.

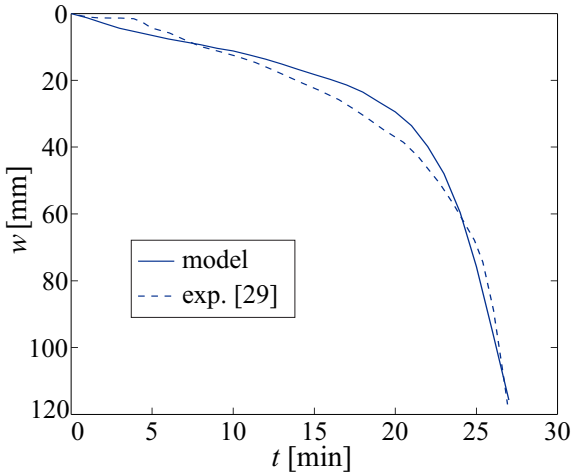

Figure 4.13: Development of calculated and measured mid-span displacement during fire exposure.
Slika 4.13: Razvoj izračunanega in izmerjenega pomika na sredini nosilca med požarno izpostavljenostjo.

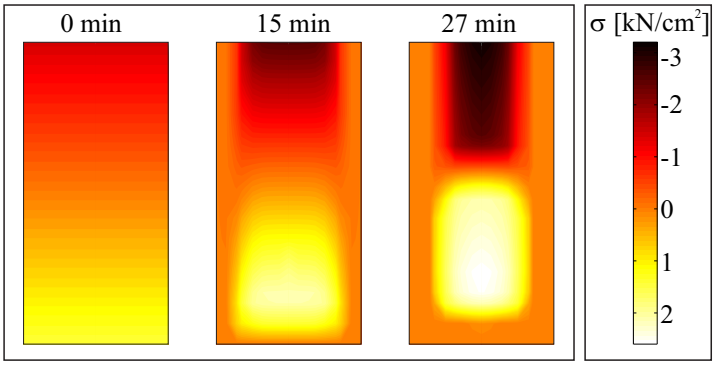

Figure 4.14: Distribution of stresses over the cross-section at mid-span for chosen times.
Slika 4.14: Razpored napetosti po prečnem prerezu na sredini razpona pri izbranih časih.

5 RELIABILITY

5.1 Introduction

The primary objective of structural design is the verification that a system resistance (R) exceeds load demand (S), expressed with inequality as: $S < R$. However, random nature of fire, thermal and mechanical properties of material and mechanical load lead to considerable amount of uncertainties both in system resistance and load. The traditional engineering practice to determine fire safety follows the prescriptive code requirements [111]. This approach does not directly consider the random nature of most parameters. Instead, characteristic values and partial safety factors are taken into account in order to control the level of fire safety (Fig. 5.1). According to Eurocode [111], the partial safety factors are calibrated so that the target probability of failure for structure exposed to fire is lower than $p_f = 7.23 \cdot 10^{-5}$, which corresponds to the reliability index $\beta = 3.8$.

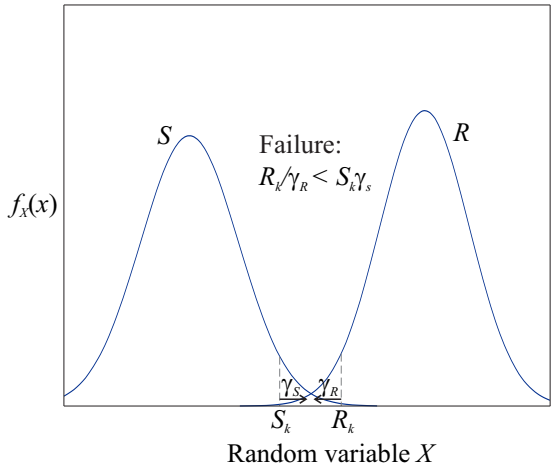

Figure 5.1: Deterministic effect of load demand S and resistance R.
Slika 5.1: Deterministični vpliv obtežbe S in odpornosti R.

Even though the prescriptive methods are usually conservative and easy to carry out, it is impossible to quantify the degree of conservatism and to evaluate the reliability of the system. For this reason, the prescriptive codes are lately being replaced by the performance based methods. These methods provide improved understanding of structural fire design and enable thorough research of structural reliability in fire [112]. Eurocode [111] proposes level 2 and level 3 methods to determine the structural reliability in fire. In level 2 methods, each uncertain variable is described by two parameters, its mean value and variance, and supplemented by the correlation between the variables. To determine the structural reliability in fire, an analytical expression for the limit state function has to be known when using level 2 methods. Therefore, the main drawback of these methods is that only simple problems can be treated. Typical level 2 methods are first and second order reliability methods (FORM, SORM). Level 3 methods use joint probability distribution of all uncertain variables to describe each uncertain variable [113], meaning

that parameters associated with system resistance and load can be described as random variables with corresponding statistical distribution in order to determine the system reliability. The most commonly used level 3 method is the Monte Carlo method.

There are many recent reliability studies on timber and also other structural materials exposed to fire. Torrati et al. [114] presented the reliability analysis of a tapered glulam beam that was part of a real structure. Probability of failure for normal design (ultimate limit state) and under a fire situation was assessed. Due to the simplicity of the problem, i.e., the analytical description of the limit state, different methods (FORM, SORM, Monte Carlo) gave almost identical results. In the research by Hietaniemi [115], probabilistic fire simulator was introduced, enabling to account for the uncertain fire behaviour in the Fire Dynamics Simulator. Further on, new charring rate model was proposed, accounting for external heat flux and uncertainties of the influential factors such as wood density, ambient oxygen concentration and moisture content of wood. Pieniak et al. [116] studied the influence of increased temperatures on the wood composites, where the probability of failure of these elements was estimated. An interesting work from this field, but for different structural material, was conceived by Guo et al. [112]. Fire resistance of a protected steel beam was evaluated, giving the uncertainties in the fire load and structural resistance parameters. The Monte Carlo simulation was used with integrated finite element calculations.

5.2 Monte Carlo Simulation Method

The Monte Carlo Simulation method (MCS) is an important tool to perform reliability analysis, especially for complex problems. The concept of the method is to implement a large number of simulations, where random input variables are generated in each step. In each simulation the structural response in fire is determined and also failure occurrence is examined. By doing so, the probability of failure is determined as:

$$p_f = \frac{N_f}{N}. \tag{5.1}$$

Here, N_f is the number of simulations where failure occurred and N is the total number of simulations. The MSC can be applied to many practical problems and allows any type of probability distribution for a random variable. It is easy to implement and enables computing the probability of failure with the desired precision. However, the method can become time consuming in cases of very low failure probability, where high number of simulations is needed to accurately predict the probability of failure. In these cases, variance reduction methods offer a way to decrease the required number of simulations. For the purposes of this thesis, Latin hypercube sampling is employed.

5.2.1 Latin Hypercube Sampling

Latin Hypercube Sampling (LHS) is a stratified sampling technique first developed by Iman and Conover [117, 118]. The LHS provides effective procedure of sampling variables from their distributions. In this thesis the approach proposed by Vořechovský and Novák [119] is applied. The approach combines the LHS with the stochastic optimization algorithm.

In the LHS, the distribution for each random variable is subdivided into N_{sim} equal disjunct probability intervals. In each interval, only one value is chosen as:

$$x_{i,k} = F_i^{-1}\left(\frac{k-U_m}{N_{sim}}\right), \qquad k = 1,2,...,N_{sim} \tag{5.2}$$

where U_m is the random number of uniform distribution between 0 and 1, $x_{i,k}$ is k^{th} value of random variable X_i and F_i^{-1} is the inverse cumulative distribution function for X_i. Fig. 5.2 presents the basic concept for the general LHS method.

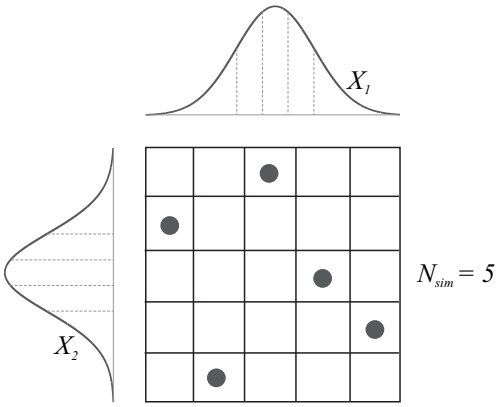

Figure 5.2: Basic concept of LHS for two random variables and number of intervals N_{sim} = 5 [120].
Slika 5.2: Osnovni koncept LHS metode za dve naključni spremenljivki in število območij N_{sim} = 5 [120].

Due to the biased sample, undesired correlation between random variables may occur. For this reason, optimisation algorithm is introduced, seeking for the minimum of the difference between the generated correlation matrix **S** and the prescribed correlation matrix **P**. The difference is calculated with norm E.

$$E = \frac{2}{N_{var}(N_{var}-1)}\sqrt{\sum_{i=1}^{N_{var}-1}\sum_{i=1}^{N_{var}}\left(S_{i,j}-P_{i,j}\right)^2}, \tag{5.3}$$

where N_{var} is the total number of random variables, $S_{i,j}$ represents the correlation coefficient of the generated sample and $P_{i,j}$ is the target correlation coefficient between random variables X_i and X_j. Norm E is minimized with random permutations of random variable sample. The permutation is achieved by shifting the values of randomly selected variables for two randomly chosen simulations. After each permutation, norm difference is examined. Random permutation resulting in reduced norm is directly accepted. On the other hand, permutation leading to increased norm is accepted only if the value of random variable Z is greater than zero:

$$Z = e^{\frac{-\Delta E}{B}} - U_m. \tag{5.4}$$

Here, ΔE is the difference between norm E before and after permutation and B is the model parameter determined in [119]. The final outcome of the procedure is a sample of random variables with the sample correlation matrix **S**, which, within the required accuracy, corresponds to the target correlation matrix **P**.

5.2.2 Distribution of variables

In the reliability analysis uncertainties are embedded through the input data which are considered as random variables with the corresponding statistical distributions. The uncertainties are introduced in each level of the fire analysis, as seen in Fig. 5.3. Columns on the left side of the figure present the input data for each phase, while the output data are given in the right columns. For instance, uncertainties in compartment geometry, fire load and ventilation conditions result in uncertain fire compartment temperatures, which have an influence on the temperature field of the structure and eventually on the mechanical response. Uncertainties introduced in the 2^{nd} and 3^{rd} phase of the analysis have further effect on the uncertain mechanical behaviour of the structure.

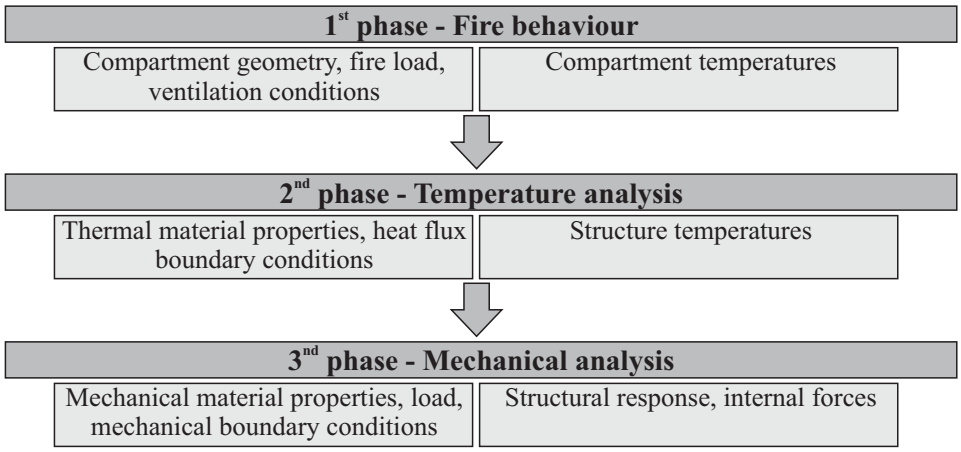

Figure 5.3: Scheme of uncertainties in structural fire analysis [112].
Slika 5.3: Shema negotovosti pri požarni analizi konstrukcije [112].

Statistical distributions and the corresponding coefficients of variation for the uncertain model parameters considered in the reliability analysis are presented in Table 5.1. The distribution and variance of input variables were collected from three main sources. The data for strength, modulus of elasticity, density and dead load are found in the probabilistic model code [99, 121]. The data describing the fire behaviour, i.e., fire load and opening factor, are acquired from [122, 123]. For the remaining inputs, to the best of author's knowledge, no data can be found in the literature to describe their statistical distributions. However, it is know that these variables are not constants. For instance, paint on a timber beam may cause different surface emissivity or increased air flow during fire leads to increased convective heat transfer coefficient. Further on, moisture content in timber depends on the relative humidity of the environment. Since the relative humidity of the environment is in general changing, the moisture content is subjected to variations as well. Furthermore, already within the same tree species, the thermal conductivity of wood varies [124] and can thus be regarded as random variable as well.

As seen from Table 5.1 input parameters are described with three different statistical distributions, which are presented below.

Table 5.1: Statistical distributions and coefficients of variations for different model parameters.
Preglednica 5.1: Statistične porazdelitve in koeficienti variacij za različne parametre modela.

Parameter	Coefficient of variation	Distribution	Reference
Fire load q_f	0.62	Gumbel	[122, 123]
Opening factor O	0.05	Normal	[123]
Convective coefficient α_c	0.15	Normal	
Surface emissivity ε_m	0.15	Normal	
Moisture content m_0	0.4	Normal	
Density of wood ρ	0.1	Normal	[99]
Thermal conductivity k	0.1	Normal	
Modulus of elasticity	0.13	Log-Normal	[99]
Strength	0.15	Log-Normal	[99]
Dead load	0.05	Normal	[121]

5.2.2.1 Normal distribution

Normal distribution is the most commonly used distribution in statistics. The probability density function (PDF) for the normally distributed random variable X is defined as:

$$f_X(x) = \frac{1}{\sqrt{2\pi}\sigma_X} e^{-\frac{1}{2}\left(\frac{x-m_X}{\sigma_X}\right)^2}, \qquad -\infty < x < \infty. \tag{5.5}$$

Cumulative distribution function (CDF) is determined by integrating the PDF:

$$F_X(x) = \int_{-\infty}^{x} \frac{1}{\sqrt{2\pi}\sigma_X} e^{-\frac{1}{2}\left(\frac{\tilde{x}-m_X}{\sigma_X}\right)^2} d\tilde{x}. \tag{5.6}$$

The two parameters describing the PDF and CDF for the normal distribution are the expected value m_X and standard deviation σ_X. The first specifies the location of the center of the variable and the second provides the information about the dispersion of the variable. Fig. 5.4 presents PDFs and CDFs for a few normally distributed random variables with different parameters m_X and σ_X. Normal distribution, with expected value 0 and standard deviation 1, is known as standardized normal distribution.

Often, the parameters of the normal distribution are not know. However, they can be estimated from a sample (x_1, x_2,..., x_n) with the method of moments. The estimators are:

$$\hat{m}_X = \overline{x} = \frac{1}{n}\sum_{i=1}^{n} x_i, \tag{5.7}$$

$$\hat{\sigma}_X = \sqrt{\frac{1}{n-1}\sum_{i=1}^{n}(x_i - \overline{x})^2}. \tag{5.8}$$

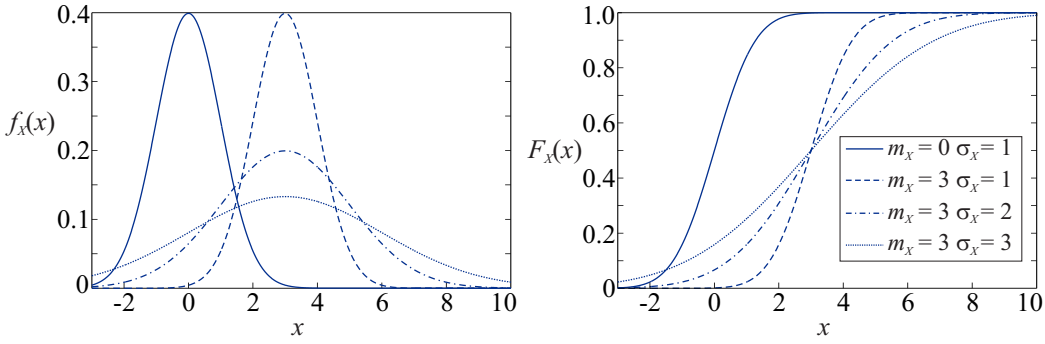

Figure 5.4: Probability density function and cumulative distribution function of normally distributed random variables for different parameters m_X and σ_X.
Slika 5.4: Gostota verjetnosti ter porazdelitvena funkcija normalno porazdeljenih slučajnih spremenljivk pri različnih parametrih m_X in σ_X.

5.2.2.2 Lognormal distribution

Random variable Y is log-normally distributed if there exists a relationship $\ln Y = X$, where X is normally distributed random variable. For variable Y, only positive values are possible and the distribution is inclined to the left. The probability density function $f_Y(y)$ of log-normally distributed random variable Y has the following form:

$$f_Y(y) = \frac{1}{\sqrt{2\pi}\sigma_{\ln Y} y} e^{-\frac{1}{2}\left(\frac{\ln y - \ln \tilde{m}_Y}{\sigma_{\ln Y}}\right)^2}, \qquad 0 < x < \infty. \tag{5.9}$$

Here, $\tilde{m}_Y$ is a median of random variable *Y*, where the following relation can be applied:

$$\ln \tilde{m}_Y = m_X. \tag{5.10}$$

The expected value m_Y and standard deviation σ_Y are:

$$m_Y = \tilde{m}_Y e^{-\frac{1}{2}\sigma^2_{\ln Y}}, \qquad \sigma_Y = \sqrt{m_Y^2\left(e^{\sigma^2_{\ln Y}} - 1\right)}. \tag{5.11}$$

Generally, it is more convenient to use inverse relationships, where parameters $\tilde{m}_Y$ and $\sigma_{\ln Y}$ are calculated from m_X and σ_Y:

$$\tilde{m}_Y = \frac{m_Y}{\sqrt{V_Y^2 + 1}}, \qquad \sigma_{\ln Y} = \sqrt{\ln\left(V_Y^2 + 1\right)}, \tag{5.12}$$

where V_Y denotes coefficient of variation determined as: $V_Y = \sigma_Y / m_Y$. In Fig. 5.5 probability density function for different parameters $\tilde{m}_Y$ and $\sigma_{\ln Y}$ is presented.

When considering certain variables, usually only their characteristic values are known. For example, timber class C30 corresponds to the characteristic value for strength determined at the 5$^{\text{th}}$ percentile $f_k = y_{0.05} = 3$ kN/cm^2. Therefore, parameter $\tilde{m}_Y$ needs to be evaluated from the characteristic value as:

$$0.05 = F_U\left(\frac{\ln y_{0.05} - \ln \tilde{m}_Y}{\sigma_{\ln Y}}\right), \tag{5.13}$$

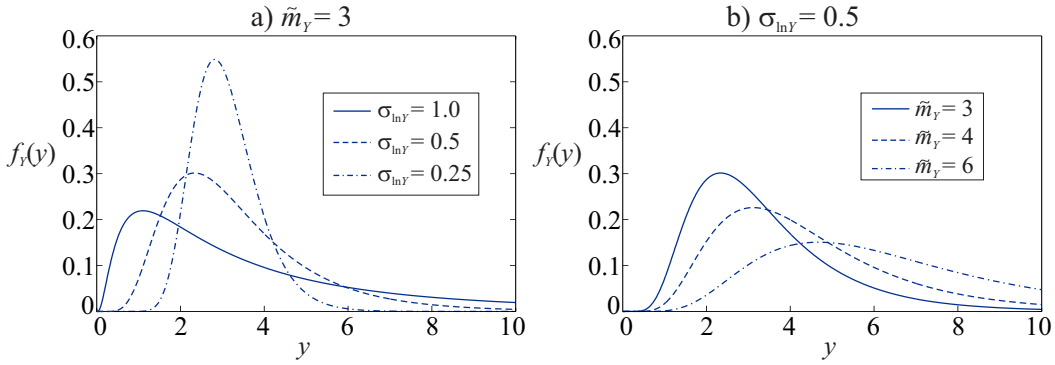

Figure 5.5: Probability density functions of log-normally distributed random variables for: a) $\tilde{m}_Y = 3$. b) $\sigma_{\ln Y} = 0.5$.

Slika 5.5: Gostota verjetnosti logaritemsko normalno porazdeljenih slučajnih spremenljivk pri: a) $\tilde{m}_Y = 3$. b) $\sigma_{\ln Y} = 0.5$.

and

$$\tilde{m}_Y = y_{0.05}\, e^{\sigma_{\ln Y} F_U^{-1}(0.05)}. \tag{5.14}$$

Above, F_U denotes the cumulative distribution function of the standardized normal distribution and F_U^{-1} is its inverse.

5.2.2.3 Gumbel distribution

Often, only extreme values of a certain variable are important. For instance, the failure of a structure occurs due to excessive fire load. Hence, it is reasonable to know the distribution of maximum fire load rather than the distribution of fire load at random time. The distribution of extreme values depends on the distribution of the initial random variable X, meaning that the distribution of the maximum or minimum is influenced by the distribution of the initial random variable on the upper or lower tail. The distribution of extreme values can be appropriately described by the Gumbel distribution. Here, only the distribution of the maximum is presented, with the following probability density function and cumulative distribution function:

$$f_Y(y) = \alpha e^{-\alpha(y-u)-e^{-\alpha(y-u)}}, \tag{5.15}$$

$$F_Y(y) = e^{-e^{-\alpha(y-u)}}, \qquad -\infty < y < \infty. \tag{5.16}$$

Parameters α and u can be derived from the moments of the random variable Y, i.e., m_Y and σ_Y:

$$\alpha = \frac{\pi}{\sqrt{6}\sigma_Y}, \tag{5.17}$$

$$u = m_Y - \frac{\gamma}{\alpha}, \tag{5.18}$$

where γ is Euler constant (0.577216). The inverse relationship is:

$$\sigma_Y = \frac{\pi}{\sqrt{6}\alpha}, \qquad m_Y = u + \frac{\gamma}{\alpha}. \tag{5.19}$$

Fig. 5.6 presents PDF of the maximum Gumbel distribution for different parameters α and u.

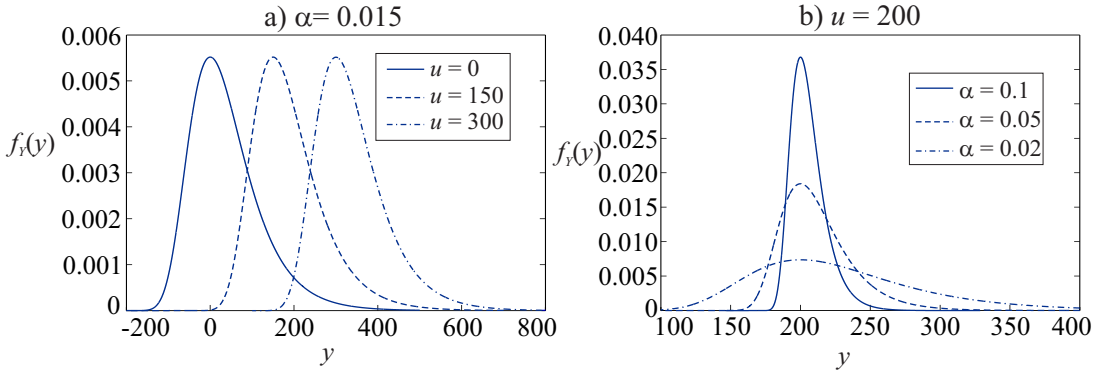

Figure 5.6: Probability density functions of the maximum Gumbel distribution for:
a) α = 0.0015. b) u = 200.

Slika 5.6: Gostote verjetnosti Gumbelove porazdelitve maksimuma pri: a) α = 0.0015. b) u = 200.

5.2.2.4 Temperature dependency of the variables

So far section 5.2 has not described how the effect of temperatures are regarded in the reliability analysis. It is known, that thermal and mechanical properties of timber change at elevated temperatures [17]. Therefore, the initial random value ($x_{0,\text{rand}}$) of the random variable X (Table 5.1) needs to be reduced by the temperature dependent reduction factor for the same random variable ($k_{X,T}$).

$$x_T = x_{0,\text{stoch}}\, k_{X,T} \tag{5.20}$$

Temperature dependent variables are thermal conductivity, density, strength and modulus of elasticity of timber, k, ρ, f, E, respectively. The reduction factors are given in sections 3.2.2.5 and 4.3.1. Temperature dependency of random variable is presented on the case of thermal conductivity of wood (Fig. 5.7). It can be seen from the figure that the curves are offset by the initial value of conductivity, which is taken as random variable. In general, the number of curves is equal to the number of Monte Carlo simulations. To make the figure more transparent, only seven different curves are presented.

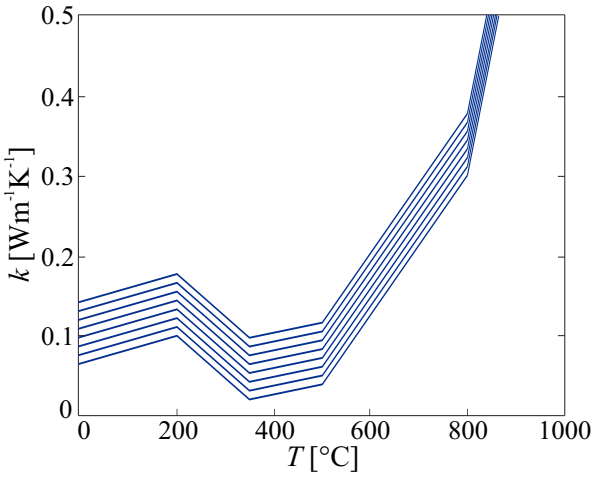

Figure 5.7: Family of curves describing timber conductivity as a function of temperature.

Slika 5.7: Družina krivulj, s katerimi opišemo vpliv temperature na toplotno prevodnost lesa.

"Blank page"

6 PARAMETRIC STUDIES AND NUMERICAL EXAMPLES

In this section the efficiency and applicability of the presented computational models is demonstrated. In the first parametric study, the influence of the initial moisture content on the mechanical behaviour of timber beam exposed to fire is investigated. The results with the simple heat transfer model embedded in the fire analysis are shown and compared to the results with the advanced coupled heat and moisture transfer model.

The second study presents the performance based approach for the fire analysis of a tapered glulam beam. Advanced computational models are used in all three steps of the fire analysis. Firstly, the FDS software [45] is used to determine the development of fire gas temperatures, secondly, the coupled heat and moisture transfer model is used to determine the distribution of temperatures in a beam and finally, the advanced mechanical formulation of the tapered beam presented in section 4 is employed to determine the mechanical behaviour of a tapered glulam beam exposed to natural fire.

In the last study, the reliability analysis of the curved timber beam exposed to fire is presented. Two different fire scenarios are considered, i.e. ISO and parametric fire curve according to Eurocode [54]. The uncertainties are applied through the parameters for the thermal and mechanical analysis and parameters describing parametric fire curve.

6.1 Influence of the initial moisture content

This parametric study presents the continuation of the analysis carried out in section 4.6.3. Focus of the study is to investigate the influence of the initial moisture content on the mechanical behaviour of simply supported timber beam exposed to ISO fire. Basic input data for the analysis are given in Fig. 6.1.

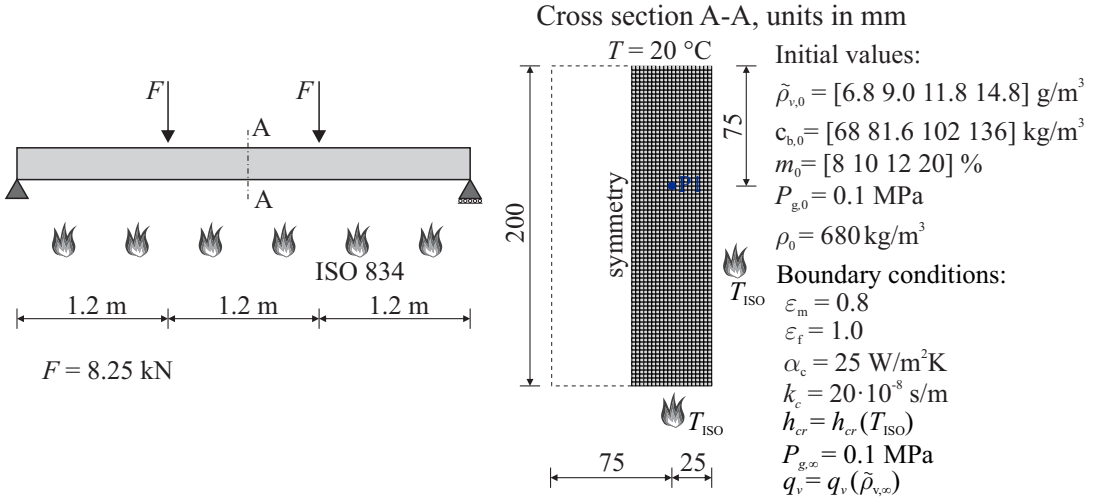

Figure 6.1: Considered beam for the mechanical analysis and basic input data for the thermal analysis.
Slika 6.1: Prikaz nosilca za mehansko analizo in osnovni vhodni podatki za toplotno analizo.

Beams with different levels of the initial moisture content, m_0 = [10 12 15 20] %, are investigated. For the determination of the temperature field (second phase), two different thermal models are used. The first one is the advanced coupled heat and moisture transfer model ("*Heat&Moisture*" model), extensively presented in section 3. The second model, hereinafter referred to as the "*Heat*" model, considers only the heat transfer using the well known Fourier partial differential equation [76]:

$$\underline{\left(\rho C\right)} \frac{\partial T}{\partial t} = \nabla \cdot (\mathbf{k} \nabla T) \,. \tag{6.1}$$

In the *Heat* model, the energy released or required from the phase change for bound water to water vapour or vice versa, is indirectly considered with the increase of the specific heat of timber [17], as presented in Fig. 3.8 (dotted line). Different levels of the inital moisture content are considered in the timber density reduction factor for temperatures below 100 °C [17], as presented in Table 6.1.

Table 6.1: Influence of initial moisture content on the timber density reduction factor for $T < 100$ °C .
Preglednica 6.1: Vpliv začetne vlažnosti na redukcijski faktor za gostoto lesa pri $T < 100$ °C.

T [°C]	k_ρ
20	1+m_0
99	1+m_0
100	1+m_0
120	1
⋮	⋮

The development of temperatures in point P1 (Fig. 6.2), determined with both thermal models, are compared with the experimental results given by Zhang et al. [29]. The results are shown up to time t = 27 min, which corresponds to the considered time in the experiment. The temperatures determined by the *Heat&Moisture* model correspond well to the measurements and the impact of the different levels of the initial moisture content is evident. As expected, higher initial moisture content results in slower development of temperatures. Temperature difference at time t = 27 min, when comparing the results with m_0 = 10% and m_0 = 20%, is more than 25 °C, which is not negligible. In the case when the *Heat* model is used in the analysis, considerable deviations can be observed when comparing the calculated and the measured temperatures. In addition, different levels of the initial moisture content have minor influence on the temperature development, since the temperature difference is only 4 °C, when comparing the results between m_0 = 10% and m_0 = 20%. This implies that the simplified *Heat* model can account for only one moisture state of timber. In order to determine this moisture state, the temperatures calculated with both thermal models are compared to each other (Fig. 6.3). The temperature developments for the points in the middle of cross-section width and 10, 20 and 30 mm from the bottom exposed edge are compared. The *Heat&Moisture* model gives higher temperatures in case when m_0 = 10 % and lower temperatures in cases when m_0 = 15 % and m_0 = 20 %, compared to the results obtained with the *Heat* model. The temperatures from both thermal models agree best at m_0 = 12 %, meaning that m_0 = 12 % is the moisture state of timber when the *Heat* model gives satisfactory results. For other moisture states of timber, major discrepancies can be observed, and thus the usage of the *Heat* model is limited.

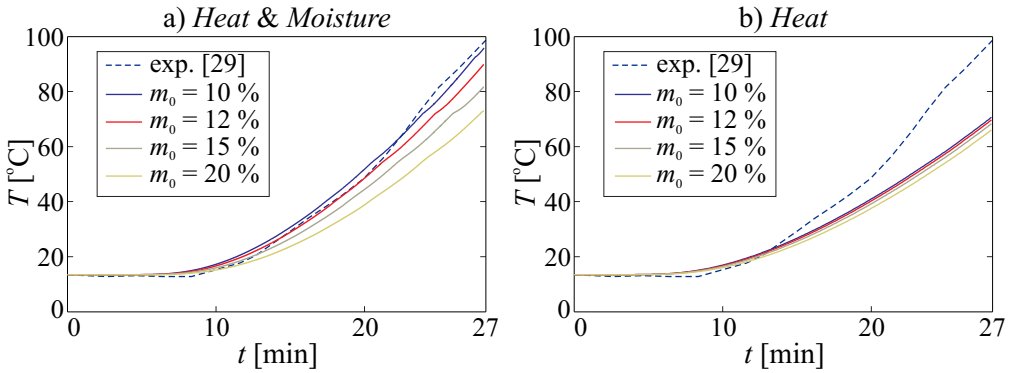

Figure 6.2: Temperature determined by [29] and: a) *Heat&Moisture* model. b) *Heat* model.
Slika 6.2: Temperature določene na podlagi [29] in: a) *Heat&Moisture* model. b) *Heat* model.

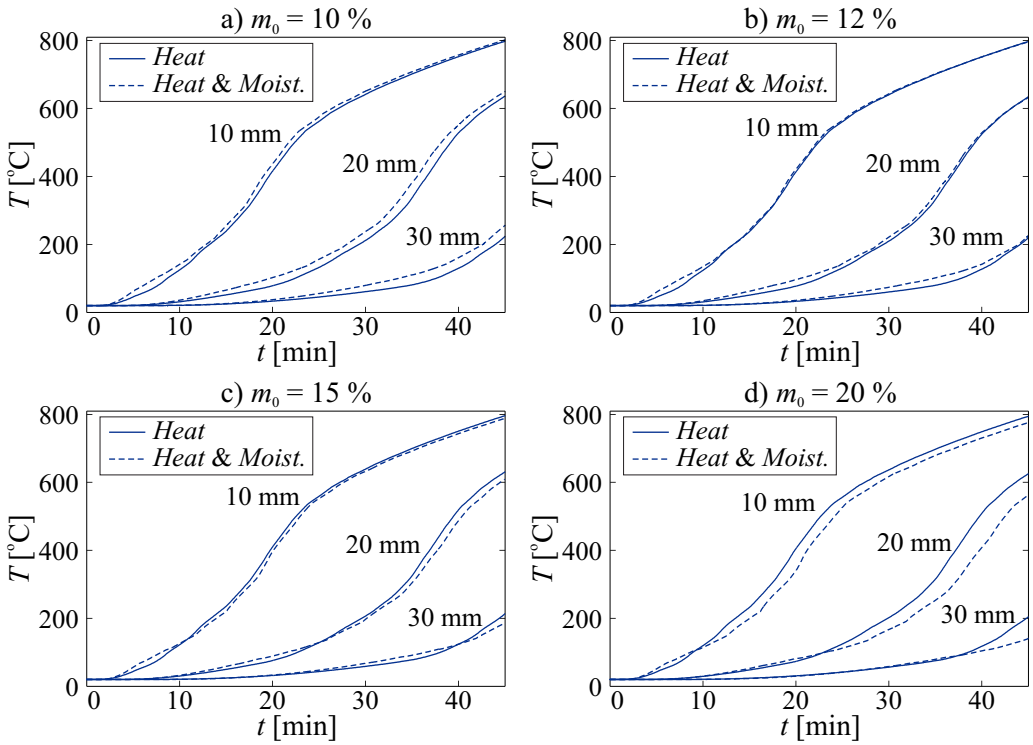

Figure 6.3: Comparison of temperatures determined by the *Heat&Moisture* and the *Heat* model at different inital moisture contents.
Slika 6.3: Primerjava temperatur določenih z modeloma *Heat&Moisture* and *Heat* pri različnih začetnih vsebnostih vlage.

In Fig. 6.4 moisture fields determined with the *Heat&Moisture* model for different initial moisture contents and simulation times 10, 20 and 30 min are presented. The difference in moisture content magnitude can be well observed when different levels of the initial moisture content are considered in the analysis. As anticipated, the moisture contents vary around m_0 for each case separately. Further on, moisture content is equal to zero closer to the exposed edge, which means that charring has occurred. The charring depths are also given in Fig. 6.4. As determined before, higher initial moisture content in the analysis

results in slower development of temperatures within a timber member. Since charring is temperature dependent, it is expected that the charring depth is smaller at higher initial moisture content considered in the analysis.

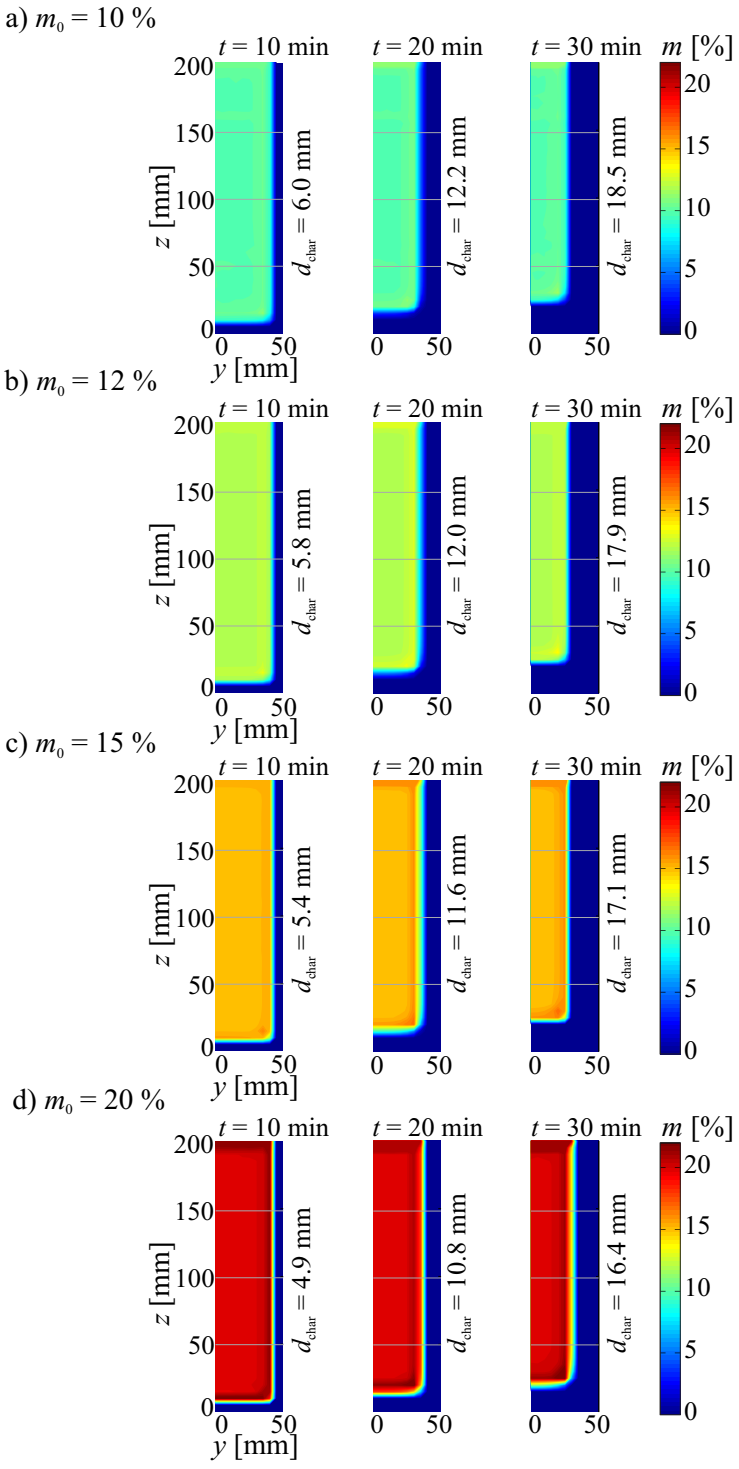

Figure 6.4: Distribution of moisture content over the cross-section at chosen times for different levels of the initial mosture content: a) m_0 = 10%. b) m_0 = 12%. c) m_0 = 15%. d) m_0 = 20%.

Slika 6.4: Razporeditev vlage po prečnem prerezu za izbrane čase v primeru različne začetne vsebnosti vlage: a) m_0 = 10%. b) m_0 = 12%. c) m_0 = 15%. d) m_0 = 20%.

Finally, the results from the mechanical analysis are demonstrated in Fig. 6.5. Here, the influence of initial moisture content on the development of the mid-span displacement is investigated. The results with both thermal models embedded are presented. The developments of mid-span displacements when the *Heat* model was implemented (Fig. 6.5b) are, as expected, more or less the same regarding the different levels of the initial moisture contents, since already small differences in the temperature development were observed before (Fig. 6.2b). In addition, the calculated mid-span displacements are overestimated compared to the experimental results. On the other hand, the development of mid-span displacements when the *Heat&Moisture* model was used in the analysis agree better to the measured mid-span displacement and the influence of the different levels of the inital moisture content is obvious. The difference in failure time for m_0 = 10 % and m_0 = 20 % is almost 5 minutes. This further justifies the usage of the advanced *Heat&Moisture* model, since it enables to account for the influence of the different initial moisture content on the mechanical response of timber beam in fire conditions.

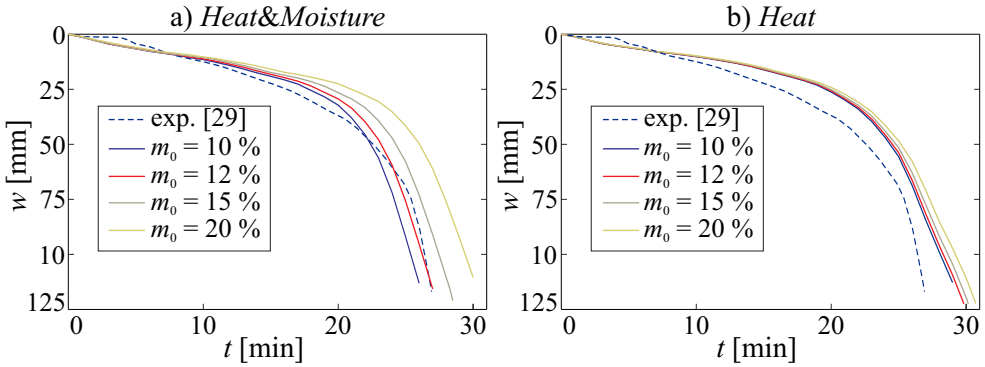

Figure 6.5: Development of mid-span displacement at different initial moisture contents when considering: a) *Heat&Moisture* model. b) *Heat* model.
Slika 6.5: Razvoj pomika na sredini nosilca pri različnih začetnih vsebnostih vlage in ob upoštevanju: a) *Heat&Moisture* modela. b) *Heat* modela.

6.2 A comprehensive study of the tapered timber beam

This study presents a performance based fire analysis of a tapered glulam beam. The beam is part of the roof structure in a sport hall located in Dravograd [125]. The fire analysis is divided in three phases. Firstly, the advanced computational software Fire Dynamics Simulator is used to determine the development of gas temperatures in the vicinity of the beams during the fire. These temperatures are then embedded as boundary conditions for the second phase, heat and moisture transfer analysis, where the temperature field over the beam cross-section is determined. The last phase presents the mechanical response of the glulam beam exposed to mechanical and fire load in the form of temperature field determined in the previous phase.

6.2.1 First phase - fire behaviour prediction with the FDS software

The geometry of the analysed sport hall is presented in Fig. 6.6. The hall is modelled as one fire compartment, with dimensions: width/length/height= 29.7×44.7×9.05 m. Since FDS enables parallel com-

puting, the calculation domain is modelled with six meshes. In order to obtain better accuracy of the results, the mesh cell dimensions in the area of the hall where fire load is prescribed are $0.3 \times 0.3 \times 0.3$ m. In the remaining area of the sport hall, the cell dimensions are $0.6 \times 0.6 \times 0.6$ m. The total number of computational cells is around 200,000.

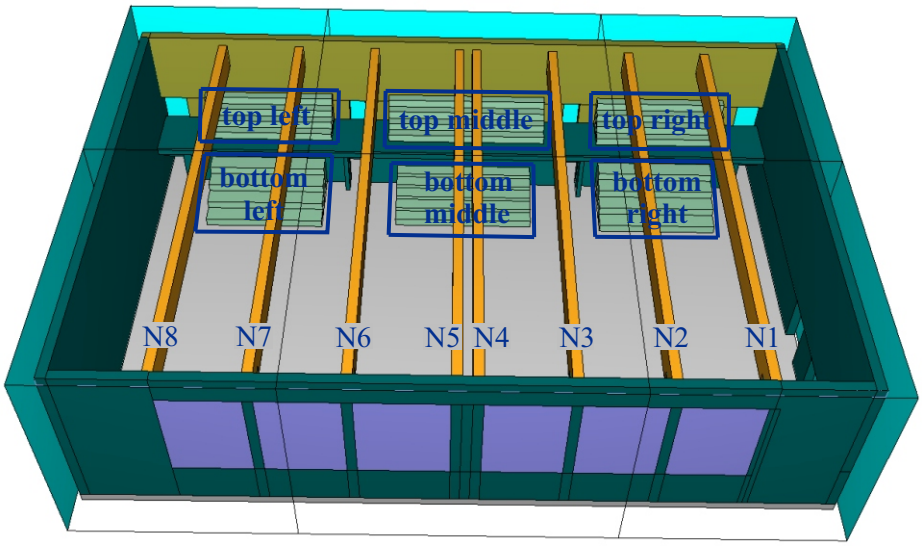

Figure 6.6: Model of the sport hall in FDS together with tribune and glulam beam labelling [61].
Slika 6.6: Model športne dvorane in prikaz označevanja tribun ter lepljenih nosilcev [61].

The hall is composed of different materials. The materials defined for the simulation are given in Table 6.2. Some of the materials can be directly imported from the FDS library [45], while parameters for other materials are obtained from literature [51, 126].

In order to obtain temperatures in the vicinity of the glulam beams, measuring devices have to be defined in the FDS model. For this reason, sensors measuring adiabatic surface temperature (AST) are virtually installed along the entire beam length. The AST represents a surface temperature of a perfect insulator, meaning that the total net heat flux to this surface is zero. The idea of the AST is to pass information to more detailed heat transfer models with the purpose to get a better prediction of solid temperature than the FDS can provide [127]. In the presented coupled heat and moisture model, this quantity corresponds to ambient temperature T_∞, when determining the boundary condition (Eq. (3.27)).

6.2.1.1 Modelling fire and fire scenarios

In general, proper knowledge and experiences are needed to adequately predict the fire scenario. The most important are the source of ignition and the amount of heat released during fire. The source of ignition is located in the tribunes, since they represent the biggest fire load within the sport hall. Between two adjacent tribunes large distances are found ($\approx$ 2-3 m). Therefore, it is assumed that the fire is localized on only one tribune and does not spread to the neighbouring one. In total, six fire scenarios with localized fire on each tribune are considered. The fire load is modelled with the prescribed *HRR* applied on five surfaces ("vent" elements) placed on the seating areas of the tribune. According to [54], fast fire growth rate (t_α = 150 s) and maximum heat release rate of RHR_f = 500 kW/m^2 are considered. The

Table 6.2: Materials used in the FDS analysis.
Preglednica 6.2: Materiali uporabljeni v analizi z FDS.

Element	Material	Thickness [mm]	Reference
Walls	Concrete	300	[45]
Floor	Concrete	300	[45]
	Yellow Pine	20	[45]
Roof	Foam	220	[45]
	Yellow Pine	20	[45]
Tribune	Polypropylene $\rho = 1100$ kg/m^3 $c = 1.6$ kJ/(kgK) $\lambda = 0.3$ W/(mK)	10	[126]
Window	Glass $\rho = 2700$ kg/m^3 $c = 0.84$ kJ/(kgK) $\lambda = 0.76$ W/(mK)	5	[51]

calculated design fire load is $q_{f,d} = 255$ MJ/m^2 [61]. The specified *HRR* is different for each fire scenario and depends on the surface area of the individual tribune A_{fi}(m^2). In Table 6.3 names of the fire scenarios, surface area of each tribune as well as maximum possible heat release rate ($HRR_{max} = RHR_f \times A_{fi}$) are given.

Table 6.3: Fire scenarios with corresponding surface areas of each tribune and maximum *HRR*.
Preglednica 6.3: Požarni scenariji s pripadajočimi površinami posameznih tribun in maksimalnim *HRR*.

Fire scenario	A_{fi} [m^2]	HRR_{max} [MW]
S1 - bottom right	37.80	18.9
S2 - bottom middle	44.55	22.3
S3 - bottom left	37.80	18.9
S4 - top right	22.32	11.2
S5 - top middle	27.36	13.7
S6 - top left	22.30	11.2

Complementary to the first six fire scenarios S1-S6, two more fire scenarios with a different technique are considered [61]. The modelling is carried out in a way allowing fire spread on the tribune. Thus, the combustible tribunes are characterized by the adequate thickness and material properties of the polypropylene. Criterion for the fire spread is represented by the ignition temperature of the burning surface $T_{ign} = 200$ °C [128]. The *HRR* development on the burning surface is similar as for previous six fire scenarios. The only difference is the area of the burning surface which is now equal to the surface area of all "active" cells involved in burning. The cell becomes active when the cell temperature on the tribune

surface exceeds the ignition temperature T_{ign}. This means that the burning surface area is determined as: $A_{\text{fi}} = n_{\text{a}} \times 0.09$ m^2, where n_{a} is the number of "active" cells and 0.09 m^2 corresponds to the surface area of the mesh cell in the area of the hall where fire load is prescribed. The source of ignition was determined from the two most unfavourable fire scenarios of the first six cases (S1-S6), selected on the basis of the maximum adiabatic temperature development on the glulam beams. For this reason, the source of ignition is placed in the bottom middle and top middle tribune, and the two additional fire scenarios are labelled as "bottom middle mat" (S7) and "top middle mat" (S8) [61]. To start the ignition, small burning surface ($A_{\text{fi}} = 0.52$ m^2) is defined with uniformly distributed heat release rate ($RHR_{\text{f}} = 1852\text{MW}/\text{m}^2$) lasting up to time $t = 300$ s.

6.2.1.2 Results of the first phase

The calculated *HRR*s for different fire scenarios are shown in Fig. 6.7. Since the developments for S1 and S3, and S4 and S6 are very similar, only one result of the pair is presented. As observed, for fire scenarios S1–S6 the fire is fuel controlled, which means that the amount of oxygen in the room is sufficient and thus enable the *HRR* to develop according to the prescribed regime. The *HRR* development for fire scenarios S7 and S8 differs significantly compared to the previous six scenarios. This occurs due to the slower fire spread on the tribune. The maximum *HRR* is 10 MW and 6 MW for the cases S7 and S8, respectively. From the maximum *HRR* the number of active cells on the burning surface in the phase of fully developed fire can be estimated $\left(n_{\text{a}} = HRR_{\max}/(0.09\text{m}^2 RHR_{\text{f}})\right)$. The number is around 222 (S7) and 133 (S8), meaning that the burning surface areas are around 20 m^2 and 12 m^2.

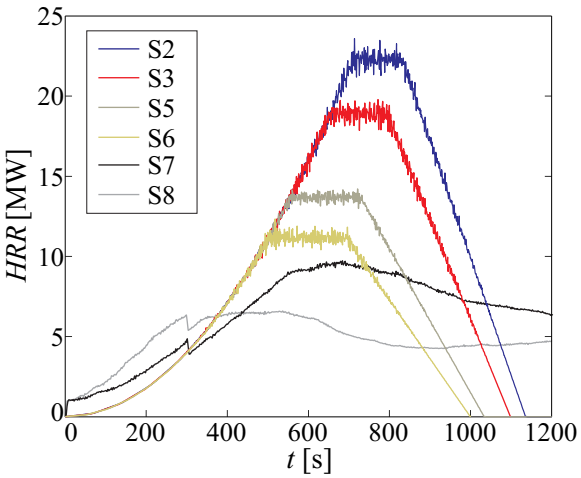

Figure 6.7: Calculated *HRR* in FDS for different fire scenarios.
Slika 6.7: Izračunan *HRR* s programom FDS za različne požarne scenarije.

Fig. 6.8 presents the development of the maximum adiabatic temperature on the surface of glulam beams. Among first six fire scenarios, the maximum adiabatic temperatures are observed on the surface of beams N4 and N5 in case when fire is modelled on the bottom middle (S2) and top middle (S5) tribunes. On average, the maximum adiabatic temperatures reach around 900 °C. Additionally, the development of the maximum adiabatic temperature for fire scenarios S7 and S8 are shown. Despite the fact that the maximum *HRR* for the fire scenario S7 is around 4 MW higher compared to scenario S8, the maximum

adiabatic temperatures are observed in the latter case (1100 °C) and are approximately 700 °C higher than in scenario S7. This is a consequence of the shorter distance between the burning surface and the beams in fire scenario S8 compared to scenario S7.

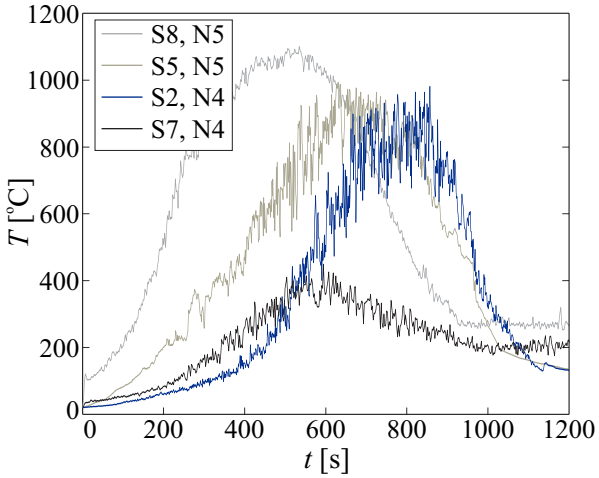

Figure 6.8: Development of the maximum adiabatic temperature on the surface of glulam beams N4 and N5 for different fire scenarios.

Slika 6.8: Razvoj največje adiabatne temperature na površini lepljenih nosilcev N4 in N5 za različne požarne scenarije.

The envelopes of the calculated maximum adiabatic temperatures on the N4 and N5 beams surfaces for different fire scenarios are demonstrated in Fig. 6.9. The envelopes are measured for every 0.30 m along the beam and are shown only up to x = 9 m, since the temperature variation onwards is insignificant. As expected, the maximum adiabatic temperatures occur above the tribune where fire load is prescribed.

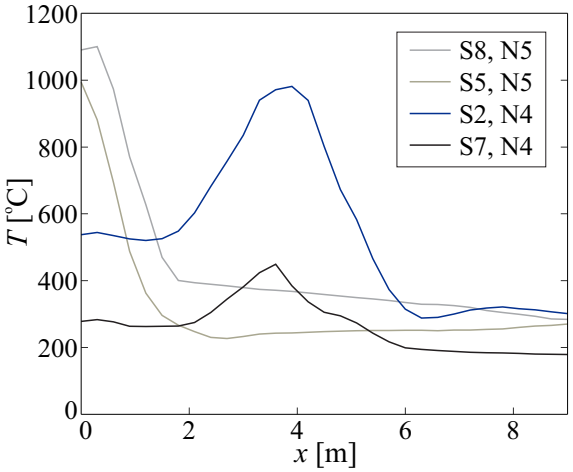

Figure 6.9: Envelopes of the maximum adiabatic temperatures on the surface of beams N4 and N5 for different fire scenarios.

Slika 6.9: Ovojnice maksimalnih adiabatnih temperatur na površini nosilcev N4 in N5 za različne požarne scenarije.

The temperatures decrease with the distance from fire. In terms of fire resistance of the beam, the most

critical are two fire scenarios. Up to the distance x = 1.5 m, the maximum adibatic temperatures are obtained with fire scenario S8, along the rest of the beam's length, the most critical is scenario S2. These two scenarios will be employed in the further steps of the fire analysis. Namely, for timber beam N4 the most critical fire scenario is S2 and for beam N5 the most critical is scenario S8.

6.2.2 Heat and moisture transfer analysis

In the previous section of this case, the adiabatic temperatures on the beam surface were determined. As observed from Fig. 6.9 the temperatures vary along the beam. Therefore, several temperature fields are introduced (Fig. 6.10) as a boundary condition for the heat and moisture transfer analysis. In total, 11 and 6 heat and moisture analyses are needed for beams N4 and N5, respectively, in order to account for the different adiabatic temperatures along the beams.

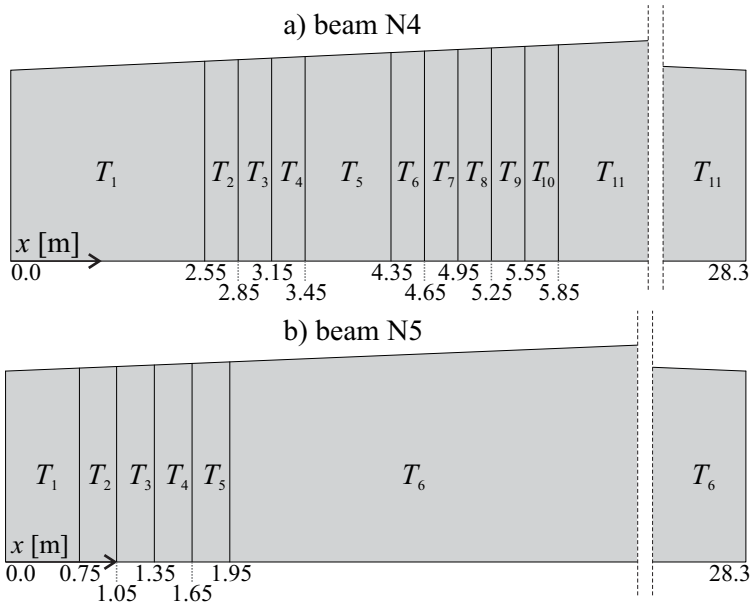

Figure 6.10: Distribution of temperature fields along beams N4 and N5 for the most critical fire scenarios.

Slika 6.10: Razpored temperaturnih polj vzdolž nosilcev N4 in N5 za najbolj kritične požarne scenarije.

In Fig. 6.11 the development of adiabatic temperatures on the beams surfaces is presented. For beam N5 all six temperature developments are shown (Fig. 6.11b). To increase the transparency of the results, only five different temperature fields are demonstrated for beam N4 (Fig. 6.11a).

For heat and moisture transfer analysis, thermal properties of timber are taken according to [17] and presented in section 3.2.2.5. Basic model input parameters are presented in Fig. 6.12. Note that for natural fires, Eurocode [54] suggests higher coefficient of heat transfer by convection than for ISO fire curve. Due to the symmetry only half of the cross-section (100 mm) is considered in the analysis. Further on, with the aim to reduce calculation time, the cross-section height in the analysis is smaller than the real one. It will be shown in the following that this assumption does not have any influence on the results. The considered height for the calculation is 200 mm. Cross-section is divided into 40 and 80 divisions in y and z direction (Fig. 6.12). The modelled section is discretized into 3200 four-node quadrilateral

finite elements. In accordance with the findings in section 3.6.1 the dimensions of the finite elements are 2.5×2.5 mm.

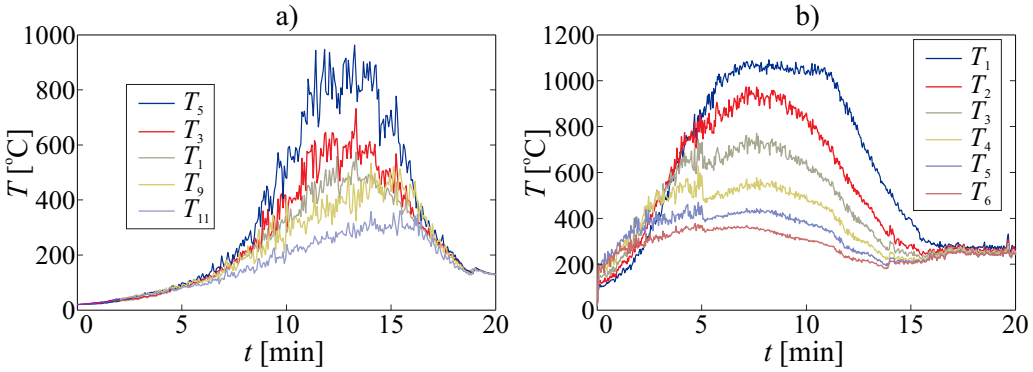

Figure 6.11: Development of adiabatic beam surface temperatures for different temperature fields along the beam: a) N4. b) N5.

Slika 6.11: Razvoj adiabatnih temperatur na površini nosilca, ki pripadajo posameznemu temperaturnemu polju vzdolž nosilca: a) N4. b) N5.

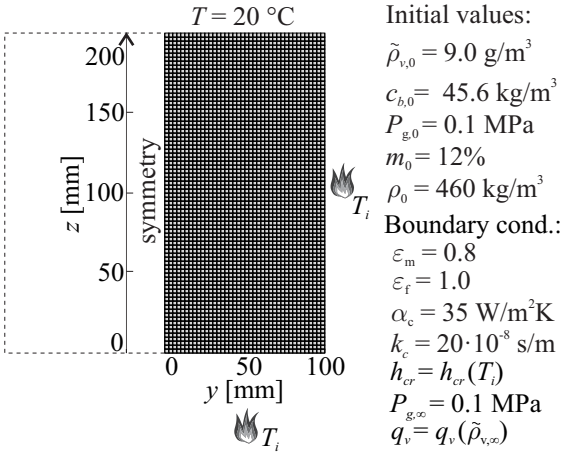

Figure 6.12: Cross-section discretisation and input data for the heat and moisture analysis of tapered timber beam.

Slika 6.12: Diskretizacija prečnega prereza in vhodni podatki za toplotno-vlažnostno analizo lesenega nosilca s spremeljivo višino.

Two dimensional distributions of the basic unknowns of the coupled heat and moisture model at chosen times are presented in Fig. 6.13. The results are shown for beam N4 at $x = 4.35$ m, where temperature field T_5 is considered as a boundary condition ($h_{cr} = h_{cr}(T_5)$). As mentioned, the considered section height for the calculation is 200 mm. This does not have any impact on the results, since temperatures, moisture content, vapour concentration and pressures do not change in z direction in the area between $z \in [100\ 200]$ mm and $y \in [0\ 100]$ mm (Fig. 6.13). Therefore, the results with the cross-section height $h = 200$ mm can be extrapolated to the cross-section with larger height. The temperature legend in Fig. 6.13a is limited by 300 °C in order to determine the charring depth. Charring starts at $t = 9.5$ min and the maximum charring depth 10.5 mm is observed at $t = 15.5$ min. Since charring is irreversible

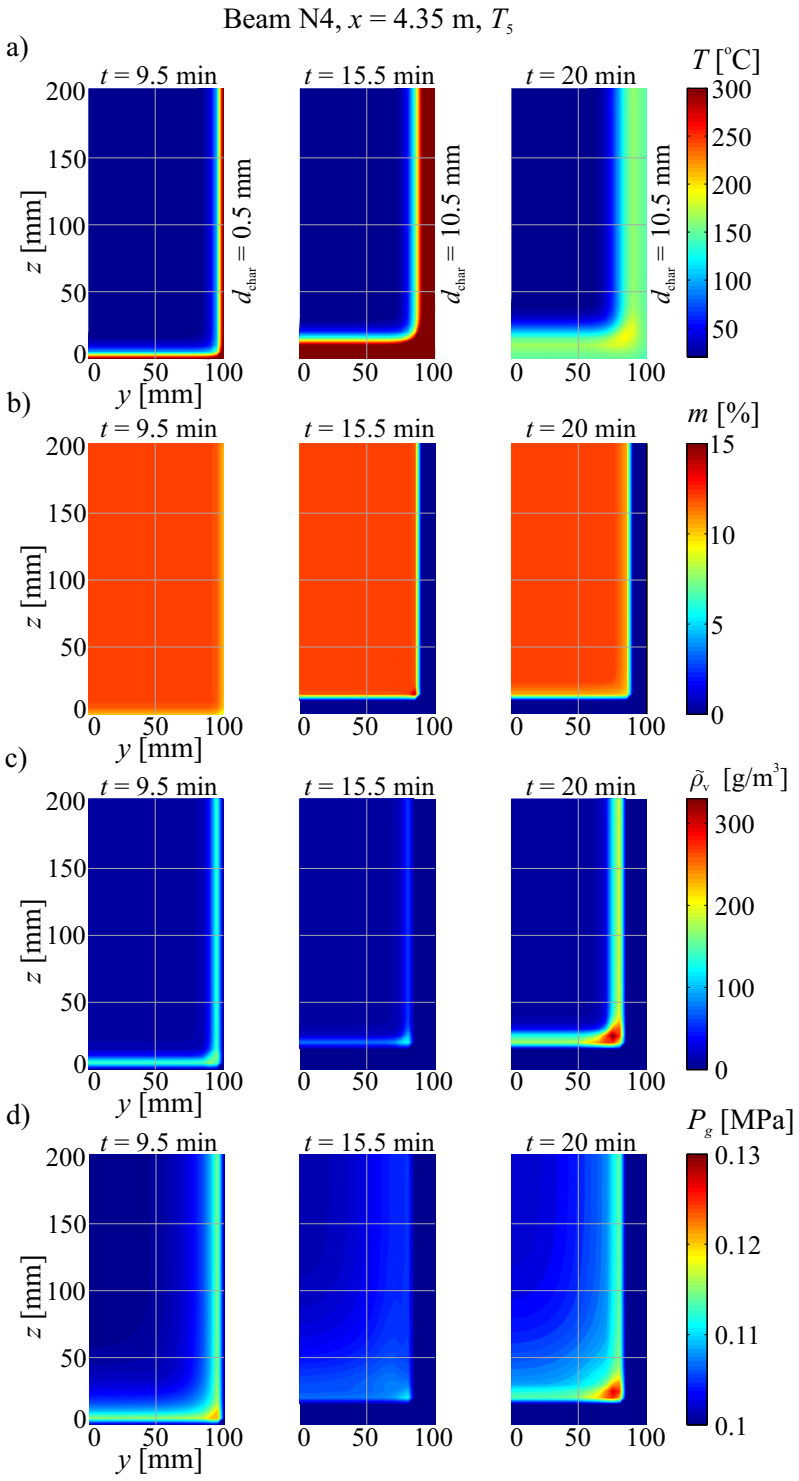

Figure 6.13: Distribution of: a) Temperature. b) Moisture content. c) Water vapour concentration. d) Gas pressure over the cross-section of beam N4 at x = 4.35 m.

Slika 6.13: Razporeditev: a) Temperature. b) Vsebnosti vlage. c) Koncentracije vodne pare. d) Pritiska plinske mešanice po prečnem prerezu nosilca N4 pri x = 4.35 m.

process, the charring depth remains 10.5 mm also in the cooling phase. Other three figures (Figs. 6.13b, c and d) distinctly demonstrate the progression of moisture front inwards the beam cross-section as it

was described in section 3.6.2.1.

6.2.3 Mechanical analysis

For the mechanical analysis the beam is modelled as a simply supported tapered beam with the length of 28.3 m, while the height varies from 2.0 m to 2.28 m (Fig. 6.14). Beam N4 is modelled with 35 and beam N5 with 32 finite elements. Timber class composing the beam is GL28c. The parameters for stress-strain relationship for the considered timber class are as follows: $E_{t,T0} = E_{c,T0} = 1260$ kN/cm^2, $f_{t,T0} = f_{c,T0} = 2.8$ kN/cm^2, $D_{t,T0} = D_{c,T0} = 0.0022$, $D_{c,p} = 0.035$, $D_{t,p} = 0.018$, $E_{c,p,T0} = E_{t,p,T0} = 50$ kN/cm^2. It is assumed that the strengths in compression and tension are the same. The reductions of mechanical properties of timber are considered according to Eurocode [17] (section 4.3.1). When determining the load on the beam, combinations of actions for the accidental design situation need to be considered [111]. According to [125], the characteristic values of permanent load, wind load and snow load are: $g_k = 1.3$ kN/m^2, $w_k = 0.8$ kN/m^2, $s_k = 1.3$ kN/m^2. Considering snow load as the leading variable action and the distance between the beams 5.4 m, the total accidental design load is equal to $q_{Ed,fi} = 8.424$ kN/m [129].

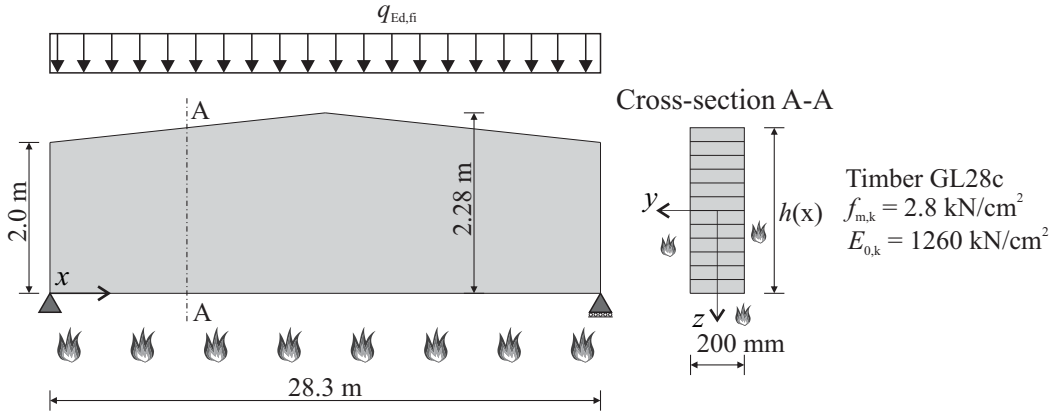

Figure 6.14: Presentation of the considered beam (the image is not in aspect ratio).
Slika 6.14: Prikaz obravnavanega nosilca (slika ni v razmerju).

According to the findings in section 6.2.1, the entire fire time duration is 20 min. Mechanical analysis revealed that failure during this time does not occur neither for both beams N4 nor N5. The development of vertical mid-span displacement ($x = 14.15$ m) during fire simulation is presented in Fig. 6.15. The maximum vertical displacement is 38.6 mm for beam N4. Slightly greater maximum displacement (41.5 mm) is observed for beam N5. The maximum mid-span displacement increases from the initial one ($w_0 = 32.8$ mm) only by 5.8 mm and 8.7 mm, for beams N4 and N5, respectively.

The stress field of beam N4 is presented in Fig. 6.16. The distribution of stresses is presented at the point of maximum adiabatic temperatures ($x = 4.35$ m) and maximum mechanical load ($x = 12.15$ m). The highest stress in compression is 0.58 kN/cm^2 and 0.64 kN/cm^2 in tension. These values are detected at $x = 12.15$ m. The levels of stresses are much lower compared to the strength of timber GL28c at room temperature ($f_{t,T0} = f_{c,T0} = 2.8$ kN/cm^2). It can be assumed that both beams N4 and N5 are capable of withstanding much more severe fire and mechanical load. In Fig. 6.16 also the redistribution of stresses

for $t > 0$ min is observed. At t = 15 min and t = 20 min higher stresses occur in the cold interior of the cross-section. On the other hand, due to the increased temperatures and consequently lower material strength, stresses closer to the exposed edge of the cross-section are smaller. Further on, it is seen that stresses where charring took place are equal to zero (Fig. 6.16a, 15 and 20 min).

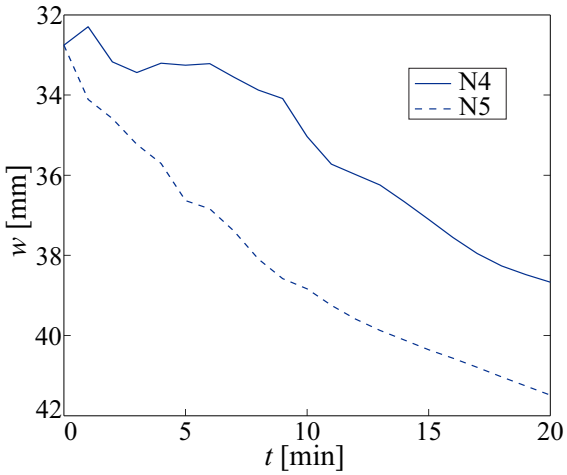

Figure 6.15: Development of mid-span displacement for beams N4 and N5.
Slika 6.15: Razvoj navpičnega pomika na sredini nosilcev N4 in N5.

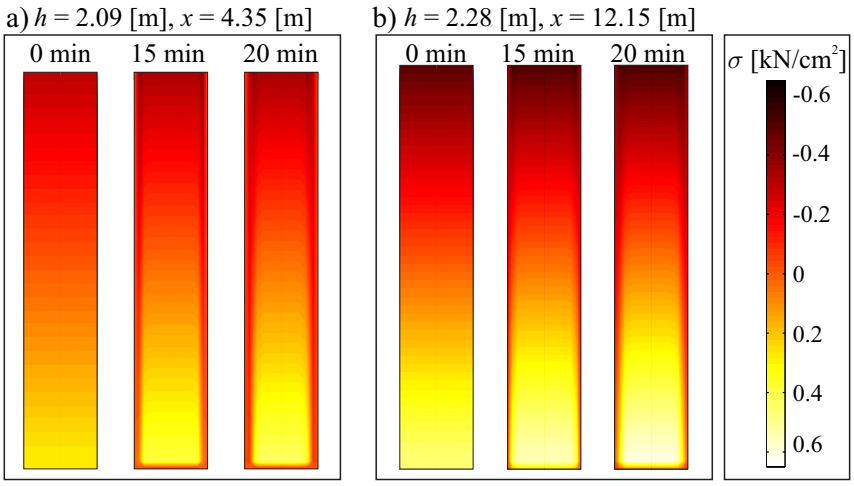

Figure 6.16: Distribution of stresses over the cross-section of beam N4 at:
a) x = 4.35 m. b) x = 12.15 m.
Slika 6.16: Razpored napetosti po prečnem prerezu nosilca N4 pri: a) x = 4.35 m. b) x = 12.15 m.

6.3 Reliability of curved timber beam exposed to fire

In the last study the performance based approach to determine the reliability of curved timber beam during the fire is given. The reliability is preformed with the Monte Carlo simulation method, where, in order to reduce the number of simulations, Latin hypercube sampling is applied. Two different fire exposures are considered, i.e, standard ISO fire curve and parametric fire curve. In both cases, the uncertainties are implemented in the advanced calculation method as randomly generated parameters for both thermal and mechanical analysis. With parametric fire curve, also the uncertain fire behaviour is taken into account. Due to the large number of numerical simulations, simplified thermal analysis is implemented in the reliability analysis, where the heat transfer is modelled by the Fourier partial differential equation (Eq. (6.1)).

The beam considered in the analysis is presented in Fig. 6.17. The arc length of the beam is 11.5 m and it is exposed to fire from three sides.

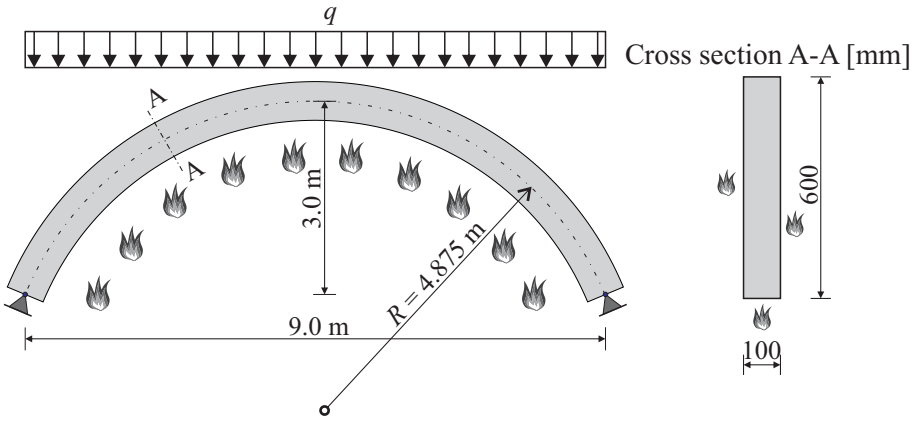

Figure 6.17: Load, geometry and cross section of the curved timber beam considered in the reliability analysis.

Slika 6.17: Obtežba, geometrija in prečni prerez ukrivljenega lesenega nosilca, ki je upoštevan v analizi zanesljivosti.

Data for the uncertain parameters for the analysis are given in Table 6.4. When a variable is described with normal or gumbel distribution, it may in some cases take an unrealistic value, for instance, a negative value for density ρ or fire load q_f. For this reason, limitations are introduced in the term of minimum and maximum values of a variable.

The correlation between uncertain parameters is presented in Table 6.5. The correlation coefficients for $\rho - E$, $\rho - f$ and $E - f$ are given in [99]. Strong correlation between density and thermal conductivity was reported by Kiran et al. [124]. For coefficients $k_0 - E$, $k_0 - f$ and $\alpha_c - \varepsilon_m$ no data can be found in the literature. Therefore, the values of these coefficients are only assumed.

Table 6.4: Data for uncertain parameters.
Preglednica 6.4: Podatki za negotove parametre.

Parameter	Distribution	Mean	COV	Min	Max
q_f - fire load	Gumbel	564 MJ/m^2	0.62	190	3800
O - opening factor	Normal	0.15	0.05	0.02	0.2
ρ_0 - initial dry density	Normal	400 kg/m^3	0.1	250	600
k_0 - initial thermal conductivity	Normal	0.12 W/mK	0.1	0.09	0.16
m_0 - initial moisture content	Normal	0.12	0.4	0	0.3
α_c - convective heat transfer coeff.	Normal	25 W/m^{2}K	0.15	15	35
ε_m - surface emissivity	Normal	0.7	0.15	0.5	1
E - modulus of elasticity	Log-Normal	1200 kN/cm^2	0.13	700	1600
f - strength	Log-Normal	3 kN/cm^2	0.15	1	5
q - load	Normal	10 kN/m	0.05	5	20

Table 6.5: Correlation coefficient matrix.
Preglednica 6.5: Matrika korelacijskih koeficientov.

	O	ρ	k	m_0	α_c	ε_m	E	f	q
q_f	0	0	0	0	0	0	0	0	0
O		0	0	0	0	0	0	0	0
ρ			0.92	0	0	0	0.6	0.6	0
k				0	0	0	0.6	0.6	0
m_0					0	0	0	0	0
α_c						0.2	0	0	0
ε_m							0	0	0
E								0.8	0
f									0

6.3.1 Standard ISO fire exposure

In the case of standard fire exposure, the total number of simulations in reliability analysis is N_{TOT} = 10134. Fig. 6.18 presents the output variables of the study which are found interesting. The graphical representation of the numerical data distribution (histograms) and the corresponding probability density functions are presented. It was found out that the normal distribution can be applied for the mid-span displacement at 30 min (w_{30}) and for the failure time (t_{fail}). On the other hand, log-normal distribution is more suitable to characterize the mid-span displacement at 45 min (w_{45}) and at failure time. Corresponding parameters for mentioned distributions are shown in Table 6.6.

The distribution of the failure time is chosen as the limit state function of this case. The target probability of failure during the structure lifetime for normal use defined in Eurocode [111] is $p_t = 7.23 \cdot 10^{-5}$, which

corresponds to the reliability index β = 3.8. The same safety requirement is also adopted as acceptable criterion for the fire safety of the analysed structure. Failure time that meets this criterion is 40 minutes.

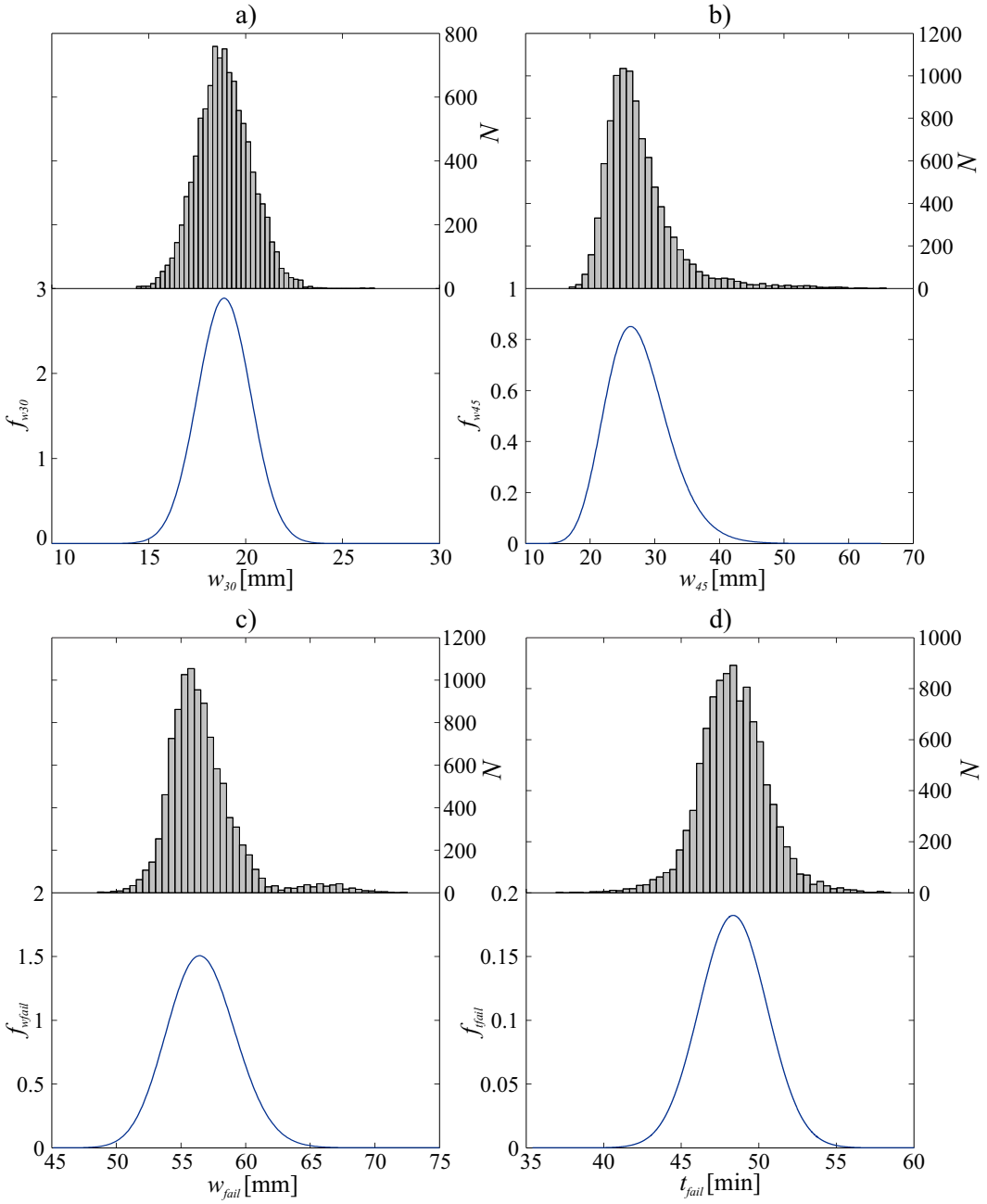

Figure 6.18: Histograms and probability density functions for: a) mid-span displacement at 30 min, w_{30}. b) mid-span displacement at 45 min, w_{45}. c) mid-span displacement at failure time, w_{fail}. d) failure time, t_{fail}.

Slika 6.18: Histogrami in gostote verjetnosti za: a) pomik na sredini razpona pri 30 min, w_{30}. b) pomik na sredini razpona pri 45 min, w_{45}. c) pomik na sredini razpona pri času porušitve, w_{fail}. d) čas porušitve, t_{fail}.

Table 6.6: Statistical distributions, mean values and coefficients of variation for the chosen output variables.

Preglednica 6.6: Statistične porazdelitve, srednje vrednosti in koeficienti variacij izbranih izhodnih spremenljivk.

Output variable	Distribution	Mean	COV
w_{30}	Normal	18.9 mm	0.07
w_{45}	Log-Normal	27.5 mm	0.24
w_{fail}	Log-Normal	56.6 mm	0.07
t_{fail}	Normal	48.3 min	0.04

Failure time of the beam is determined when the tangent stiffness matrix of the beam becomes singular (details are given in section 4.4). Possible failure due to the exceeded stresses perpendicular to grain is not directly incorporated in the calculation. Therefore, additional analysis was performed, where stresses perpendicular to grain were post-processed according to the equations given in section 4.5. Mean values from Table 6.4 were taken as the input data for the analysis. The distribution of stresses perpendicular to grain at different simulation times are presented in Fig. 6.19. As observed, strength perpendicular to the grain $f_{\mathrm{t,90,k}} = 0.04$ kN/cm^2 is exceeded at time $t = 49.25$ min, i.e., when the failure of the beam occurred. This means that failure of the beam conditioned by the singularity of the stiffness matrix and failure due to the exceeded stresses perpendicular to grain occur at the same time for the observed case. It was therefore assumed that failure due to the exceeded stresses perpendicular to the grain did not have an influence on the beam failure also in others Monte-Carlo simulations, and, for this reason, was not specifically taken into account.

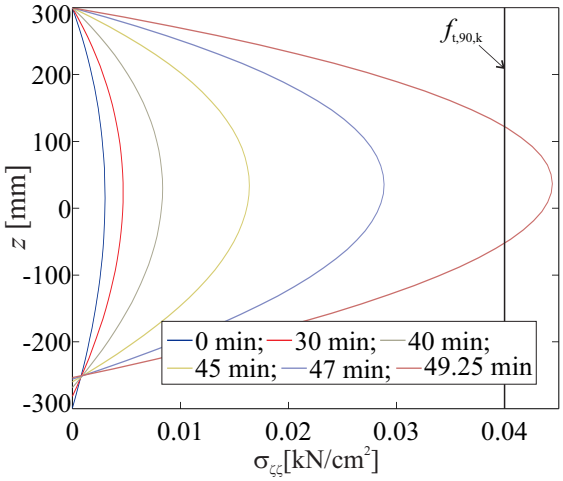

Figure 6.19: Distribution of normal stress perpendicular to grain $\sigma_{\zeta\zeta}$ at different times.

Slika 6.19: Razpored normalne napetosti pravokotno na vlakna $\sigma_{\zeta\zeta}$ pri različnih časih.

6.3.2 Parametric fire exposure

For the study with parametric fire curve, the room size of $b/h = 8/10$ m is considered. To describe the possible fire scenarios, the uncertainties of the parametric fire curve are implemented through the design fire load q_f and opening factor O, as presented in Table 6.4. Further on, the properties of the boundary enclosure are: density $\rho = 2500$ kg/m^3, specific heat $c = 1100$ J/kgK and thermal conductivity $\lambda = 1$ W/mK. Medium fire growth rate is accounted for in the analysis. Therefore, $t_{\text{lim}} = 20$ min. Different parametric fire curves generated from the input data are presented in Fig. 6.20. Two different temperature developments can be distinguished. When fire is ventilation controlled (Eq.(2.8)), temperature increase is faster than when fire is fuel controlled. In addition, ISO fire curve is added. It can be observed that ventilation controlled parametric fires are much more severe than ISO fire.

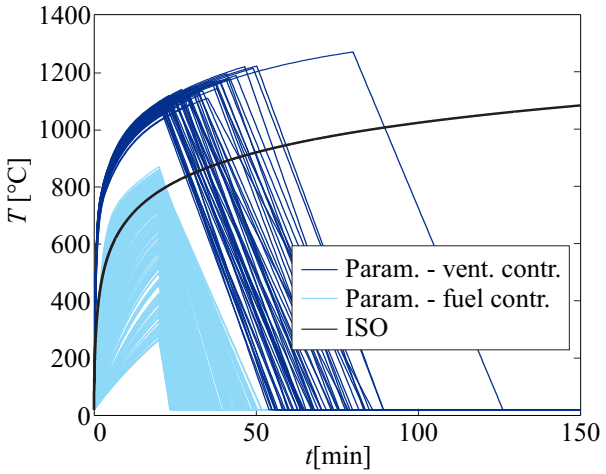

Figure 6.20: Some of the parametric fire curves ($n = 500$) considered in the analysis.
Slika 6.20: Nekaj izmed parametričnih krivulj ($n = 500$) upoštevanih v analizi.

The total number of Monte Carlo simulations in this study is $N_{\text{TOT}} = 12144$. The probability of failure p_f as a function of fire duration is shown in Fig. 6.21. Results with both ISO and parametric fire curves are presented. In case of parametric fire curve, the probability of failure starts increasing after 20 min of fire exposure and reaches the plateau after 30 min of exposure ($p_{\text{f},30} = 0.213$). This means that failure occurs in a time range between 20 min and 30 min, which corresponds to the more severe ambient temperature development, when fire is ventilation controlled. On the other hand, the results with ISO fire demonstrate, that failure prior time $t = 38.3$ min does not occur. Therefore, it is not always safe to use ISO fire curve and for the performance based design it is better to consider the possible spectrum of real fire curves.

At the end of this study, the reliability index β is calculated. It is determined as the normal inverse cumulative distribution function of the probability of failure:

$$\beta = \text{norminv}\,(1 - p_{\text{f}}) \tag{6.2}$$

The development of β as a function of time is presented in Fig. 6.22. The time that meets the Eurocode [111] safety requirement ($\beta \geq 3.8$) is 20 min for the parametric curve and 40 min for the ISO curve. β

levels at 0.8 for the parametric fire, whereas for the ISO fire, it reaches minus infinity which corresponds to the $p_f = 1$.

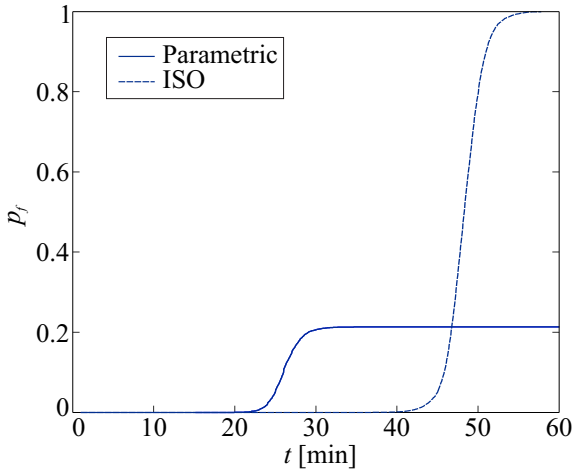

Figure 6.21: Probability of beam failure as a function of fire duration.
Slika 6.21: Verjetnost porušitve nosilca v odvisnosti od trajanja požara.

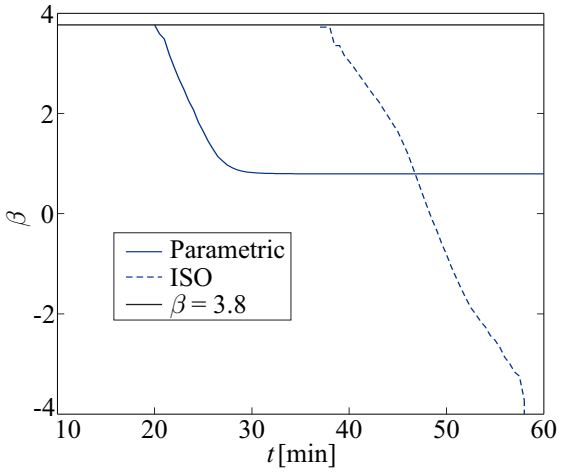

Figure 6.22: Reliability index β as a function of fire duration.
Slika 6.22: Indeks zanesljivosti β v odvisnosti od trajanja požara.

7 CONCLUSIONS

The thesis presents a new numerical model for the non-linear fire analysis of the curved and tapered timber beam. The model is divided in three separated phases. The fire behaviour within the fire compartment is discussed in the first phase. Two different perspectives are adopted. Firstly, the analytical expressions given by the standardized fire curves are used. Secondly, advanced computational model based on the computational fluid dynamics is applied. The most advanced software to predict fire behaviour, program package Fire Dynamics Simulator [45], is chosen. The governing Navier-Stokes equations in the software are written to be applicable for thermally driven, low speed flow.

The main topic of the thesis is the second phase of the numerical model. Here, a new mathematical and numerical model to describe and determine the coupled heat and moisture transfer in timber exposed to fire is introduced. The model accounts for the transfer of bound water, water vapour and air, coupled by the heat transfer. The convective and diffusive transfer of gaseous mixture is considered, while the bound water transfer follows Fick's law of diffusion refined by also including the Soret effect. In addition, coupling between bound water and water vapour, know as sorption, is accounted for. The sorption model is modified to be applicable for the temperatures above the boiling point. The conductive transfer of heat through the cell wall accompanied by the convective heat transfer of the gaseous mixture is considered. Further on, the energy consumed or required due to the phase change from bound water to vapour or vice versa is accounted for. The model has also a built-in temperature dependent criterion of charring. Since charring depth normally increases with the fire exposure, a moving boundary surface is introduced to prescribe water vapour flux and pressure at the contact between timber and char layer. The governing equations of the presented problem are solved numerically by the finite element method developed in the Matlab environment. The developed software allows to determine two-dimensional temporal development of temperatures, gas pressures, water vapour and bound water concentration. Extensive validation and parametric studies were conducted and the following points were concluded:

- convergence test revealed that the size of the finite element should be 2.5 mm or less in order to accurately predict the charring depth,
- by validating the numerical results with the experiment carried out by König and Walleij [77] and Lache [78] it was confirmed that the numerical model is capable of reproducing an accurate temperature field for the timber element exposed to fire,
- the validation of the charring depth revealed good agreement between the measurements and the numerical results. Furthermore, the assumption to set the char front temperature at 300°C for fires with heating regime similar to ISO curve is appropriate,
- different levels of the initial moisture content of timber have a significant influence on the temperature development. Higher initial moisture content results in slower development of temperatures. Also the advantage of the presented numerical model compared to the simplified *Heat* model (Fourier partial differential equation) was demonstrated. The presented model can account for dif-

ferent levels of initial moisture contents, while the *Heat* model is restricted to only one moisture state of timber, namely 12 %,

- the sensitivity analysis revealed two major discoveries: Firstly, the influence of bound water diffusion (D_0) on the total moisture content is significant compared to the room temperature behaviour. Secondly, the convective heat transfer is not having a significant impact on temperature distribution. Therefore, in order to increase the calculation efficiency, while preserving the accuracy of the model, the simplification of the energy equations was introduced.

The mechanical model for the analysis of curved and tapered timber beam simultaneously exposed to mechanical and fire load is presented in the third phase of the numerical model. The mechanical model is a continuation of the work conducted by Čas [47] and is here expanded to be applicable at elevated temperatures. In addition, constitutive relations for timber material are introduced. Beam deformation is mathematically described by Reissner's kinematically exact beam theory [48] where membrane, shear and flexural deformation of the beam are accounted for. Following Reissner's model, the time dependent stress-strain state of the beam is determined by the system of kinematic, equilibrium and constitutive equations with the corresponding boundary conditions. The equations are discretizited by the Galerkin finite element method. The strain-based finite element [39] is incorporated. The problem is solved by the Newton increment-iterative procedure. The entire fire time domain $[0, t_{\mathrm{cr}}]$ is divided into time steps $\left[t^{i-1}, t^{i}\right]$. Within each time step, known additive decomposition of the geometrical strain is considered. The failure criterion of the beam is the singularity of the tangent stiffness matrix of structure. This may occur due to the global instability of the structure or due to the material failure. The adequacy of the presented mechanical model was justified by different parametric studies and by comparing the numerical results with those available in the literature. The following conclusions can be provided:

- the model is appropriate for fire analysis of curved and tapered timber beam,
- in view of failure criterion, the post-processed normal stresses perpendicular to the grain can sufficiently describe the exact normal stresses perpendicular to the grain calculated by the 2D FEM model,
- the different levels of initial moisture content considered in the coupled heat and moisture analysis have a considerable influence on the mechanical behaviour of the timber beam during fire. The difference in the failure time was almost 5 minutes in case of standard ISO fire exposure.

In addition to the three-phase numerical model, the thesis also demonstrates the performance based approach to determine fire safety of a timber beam. The methodology for the reliability of a timber beam exposed to fire is presented. The uncertainties are introduced through the uncertain fire behaviour, thermal and mechanical properties of wood and also mechanical load. The reliability analysis was presented on a curved glulam beam exposed to ISO and parametric fire curve. The Monte Carlo simulation method was used. With the purpose to reduce the number of simulations, Latin hypercube sampling was applied. This study leads to the conclusion that it is not always safe to use ISO fire curve and it is better to consider the possible spectrum of real fire curves.

RAZŠIRJENI POVZETEK

UVOD

Les dandanes predstavlja sodoben, okolju prijazen, trajnostni material, s široko možnostjo uporabe v gradbeništvu. Eden izmed bolj razširjenih lesenih produktov je lameliran lepljen les, ki se je razvil iz potrebe po lesenih elementih večjih dimenzij, z namenom gradnje lesenih objektov večjih razponov. Poleg številnih prednosti, ki jih ponuja les kot gradbeni material, je ena izmed njih nedvomno ugodno obnašanje pri povišanih temperaturah in posledično tudi dobra požarna odpornost.

V literaturi se številne raziskave osredotočajo na obnašanje lesa pri povišanih temperaturah oziroma v požaru. Ker je les izrazito higroskopen material, ima vlaga velik vpliv na razvoj temperatur v lesu. V ta namen je bilo razvitih veliko modelov, ki povezano obravnavajo prenos toplote in vlage [5–16]. Večina teh modelov je bila razvita za simulacijo sušenja lesa pri povišanih temperaturah, zato v modelih večinoma ni bila upoštevana piroliza in oglenenje lesa. Za določitev razvoja oglenenja v požaru obstaja mnogo empiričnih modelov [17–20]. V nasprotju z empiričnimi modeli, pa se danes vedno večje število raziskovalcev posveča razvoju kompleksih numeričnih modelov za simulacijo pirolize in oglenenja lesa [21–25]. Poleg kompleksnih toplotno-vlažnostnih in piroliznih modelov, je v literaturi mogoče zaslediti tudi mnogo numeričnih in eksperimentalnih raziskav osredotočenih na mehansko obnašanje lesenih elementov v požaru. Še vedno so najpogostejše standardne požarne raziskave [26–29]. Čeprav so ti testi zelo pomembni za določitev nominalne požarne odpornosti, pa obenem ne omogočajo vpogleda v obnašanje lesenega elementa v realnem požaru. Nekaj nedavnih raziskav, kjer je obravnavano obnašanje lesenega elementa v naravnem požaru, je mogoče najti v [30, 31].

Pregled literature razkriva pomanjkanje na področju naprednih in celovitih modelov za analizo lesenih elementov izpostavljenim naravnim požarom. Večina raziskovalcev za določitev mehanskega odziva lesenega elementa pri požaru za modeliranje prenosa toplote po lesu uporablja poenostavljen pristop, ki temelji na Fourierjevi parcialni diferencialni enačbi prevajanja toplote po trdni snovi. Kot se je izkazalo, poenostavljen toplotni model lahko zajame le eno vlažnostno stanje lesa in zagotavlja zadovoljive rezultate za les z začetno vsebnostjo vlage okoli 12 % [42]. Običajno se vsebnost vlage lesa nenehno spreminja. V primerih ko je ta različna od 12 %, je izračunano temperaturno polje s poenostavljenim toplotnim modelom nepravilno, kar posledično vodi tudi v nepravilen mehanski odziv [29, 43, 44]. S tem se ustvarja potreba po naprednem toplotnem modelu za les v pogojih požara. Zaradi tega je glavni cilj doktorske disertacije razvoj naprednega numeričnega modela za analizo lesenih elementov izpostavljenim naravnim požarom, z glavnim poudarkom na modelu za povezan prenos toplotne in vlage, s katerim lahko predvidimo razvoj temperature, vlage in debeline zoglenele plasti ter s katerim lahko zajamemo različna vlažnostna stanja lesa.

Vsebina dela

V doktorski disertaciji je predstavljen nov matematični in numerični model za določitev odziva ukrivljenega lesenega nosilca in lesenega nosilca s spremenljivo višino hkrati izpostavljenega mehanski in požarni obtežbi. Numerični model je razdeljen v tri ločene faze. V prvi fazi določamo temperature plinov znotraj požarnega sektorja. V ta namen uporabimo znane požarne krivulje [54] ali pa računalniški program Fire Dynamics Simulator [45], s katerim natančneje opišemo razvoj požara v požarnem sektorju.

V drugi fazi modela, ki predstavlja glavno temo doktorske naloge, je razvit nov matematični in numerični model za povezan prenos toplote in vlage po lesenem elementu, izpostavljenemu požaru. Zaradi porozne strukture in higroskopne narave les v svoji sestavi vsebuje različne medije, ti so vezana voda, vodna para in zrak. Gibanje vsakega izmed medijev poteka po različnih transportnih poteh. Tako prenos vodne pare in zraka poteka znotraj celičnega lumna in je fizikalno opisan s konvekcijskim prenosom, poleg tega pa se pojavlja tudi difuzija med vodno paro in zrakom. Prenos vezane vode je omejen na celično steno in je opisan s Fickovim zakonom difuzije. Proces difuzije se bistveno pospeši pri povišanih temperaturah, zato je prenos vezane vode dodatno izpopolnjen tako, da vključuje še Soretov efekt (termodifuzija). Kot smo že omenili je les higroskopen material, kar pomeni, da pride do vezave molekul vode (vezana voda) v celično steno. Prehajanje molekul vodne pare v vezano vodo (adsorpcija) oziroma molekul vezane vode v vodno paro (desorpcija) imenujemo s skupnim izrazom sorpcija. V toplotno-vlažnostnem modelu to formalno upoštevamo s sorpcijskim modelom, ki je primeren tudi za temperature nad točko vrelišča. Podobno kot prenos vlage, tudi prenos toplote poteka po več transportnih poteh. Po celični steni prihaja do kondukcijskega prenosa toplote, medtem ko konvekcijski prenos toplote nastopi zaradi gibanja plinov v celičnem lumnu. Poleg tega se zaradi spremembe agregatnega stanja vezane vode v vodno paro in obratno, sprošča oziroma porablja energija, kar v modelu upoštevamo z latentno toploto sorpcije ob spremembi faze. Pri povišanih temperaturah in pri požaru, je za les značilno, da ogleni. V modelu je vgrajeno temperaturno odvisno oglenenje lesa, natančneje, predpostavimo, da les začne ogleneti pri 300 °C [17]. Ker se debelina zoglenele plasti veča s požarno izpostavljenostjo, je v model vpeljana premikajoča robna ploskev, s katero zajamemo časovni razvoj oglenenja. Matematično povezan prenos toplote in vlage opišemo s sistemom štirih diferencialnih enačb. Ker analitična rešitev tega sistema ni možna, enačbe rešujemo numerično z metodo končnih elementov, kjer je uporabljena Galerkinova diskretizacija in štiri-vozliščni izoparametrični končni element. Izbrane osnovne neznanke sistema enačb za metodo končnih elementov so: temperatura T, pritisk plinske mešanice P_g, koncentracija vodne pare $\widetilde{\rho}_v$ in koncentracija vezane vode c_b.

V zadnji fazi predstavljamo mehanski model za določitev napetostno-deformacijskega stanja lesenega ukrivljenega nosilca in nosilca s spremenljivo višino pri požaru. Model temelji na formulaciji ukrivljenega nosilca, ki ga je v doktorski nalogi predstavil Čas [47]. Mehanski model je tukaj razširjen na uporabo pri povišanih temperaturah, dodatno pa je preurejen za račun lesenih nosilcev s spremenljivo višino. Nosilec opišemo z geometrijsko točnim modelom Reissnerjevega ravninskega nosilca, kjer je upoštevan tudi vpliv strižne deformacije na deformiranje nosilca. V modelu je zajeta materialna nelinearnost [49] ter temperaturno odvisno obnašanje lesa [17]. Sistem posplošenih ravnotežnih enačb je rešen z metodo končnih elementov z vgrajenim deformacijskim končnim elementom [39]. Pripadajoči sistem nelinearnih algebrajskih enačb končnega elementa je rešen z Newtonovo inkrementno-iteracijsko

metodo, kjer celotni čas požara razdelimo na časovne prirastke $\left[t^{i-1},\ t^{i}\right]$. Kriterij porušitve konstrukcije, ki je lahko posledica globalne nestabilnosti ali materialne porušitve, predstavlja singularnost tangentne togostne matrike konstrukcije.

POVEZAN PRENOS TOPLOTE IN VLAGE

Osnovne enačbe

Matematično povezan prenos toplote in vlage opišemo s sistemom kontinuitetnih enačb za ohranitev mase, ki so dopolnjene z enačbo za ohranitev entalpije. Enačbe za ohranitev mase so zapisane za vsak medij posebej:

vezana voda: $$\frac{\partial c_b}{\partial t} + \nabla \cdot \mathbf{J}_b = \dot{c},$$

vodna para: $$\frac{\partial \left(\varepsilon_g \widetilde{\rho}_v\right)}{\partial t} + \nabla \cdot \mathbf{J}_v = -\dot{c},$$

zrak: $$\frac{\partial \left(\varepsilon_g \widetilde{\rho}_a\right)}{\partial t} + \nabla \cdot \mathbf{J}_a = 0.$$

Koncentracija vezane vode c_b je definirana na enoto volumna lesa, medtem ko sta koncentraciji vodne pare in suhega zraka $\widetilde{\rho}_v$ in $\widetilde{\rho}_a$, definirani na enoto volumna plinske mešanice. ε_g predstavlja poroznost lesa. Masni tokovi vezane vode, vodne pare in zraka $\mathbf{J}_i$ $(i = b, v, a)$ so definirani na enoto volumna lesa. $\dot{c}$ predstavlja stopnjo sorpcije, ki medsebojno povezuje ohranitev mase med vezano vodo in vodno paro, ∇ je nabla operator.

Enačba za ohranitev energije je naslednja:

$$\underbrace{\underline{\left(\rho C\right)} \frac{\partial T}{\partial t}}_{a} = \underbrace{\nabla \cdot (\mathbf{k} \nabla T)}_{b} - \underbrace{\underline{\left(\rho C \mathbf{v}\right)} \nabla T}_{c} - \underbrace{\Delta H_s \dot{c}}_{d},$$

V zgornji enačbi člen *a* predstavlja spremembo notranje energije lesa, člen *b* predstavlja dovedeno energijo zaradi prevajanje toplote, člen *c* dovedeno energijo zaradi konvekcije različnih medijev, člen *d* pa predstavlja energijo, ki je potrebna oziroma se sprošča pri spremembi faze iz vezane vode v vodno paro in obratno. Člen $\underline{\rho C}$ označuje specifično toploto lesa, matrika $\mathbf{k}$ vsebuje toplotne prevodnosti za različne smeri, ΔH_s predstavlja latentno toploto sorpcije, prenos toplote s konvekcijo plinov $\underline{\rho C \mathbf{v}}$ pa je določen kot:

$$\underline{\rho C \mathbf{v}} = \rho_g C_g \mathbf{v}_g = \left(\varepsilon_g \widetilde{\rho}_a C_a + \varepsilon_g \widetilde{\rho}_v C_v\right) \mathbf{v}_g,$$

kjer sta C_a in C_v specifični toploti zraka in vodne pare, $\mathbf{v}_g$ pa je hitrost plinske mešanice.

Konstitucijske zveze

V nadaljevanju prikazujemo konstitucijske zakone, s katerimi opišemo masni tok vezane vode, vodne pare in zraka. Prenos vezane vode v celični steni poteka zaradi koncentracijskega gradienta (∇c_b) in temperaturnega gradienta(∇T) [63]:

$$\mathbf{J}_b = -\mathbf{D}_b \nabla c_b - \mathbf{D}_{bT} \nabla T.$$

Drugi člen na desni strani zgornje enačbe je prepoznan kot Soretov efekt oziroma tako imenovana termodifuzija. Matriki $\mathbf{D}_b$ in $\mathbf{D}_{bT}$ določamo na naslednji način:

$$\mathbf{D}_b = \mathbf{D}_0 \exp\left(-\frac{E_b}{RT}\right),$$
$$\mathbf{D}_{bT} = \mathbf{D}_b \frac{c_b E_b}{RT^2},$$

kjer je R univerzalna plinska konstanta, matrika $\mathbf{D}_0$ pa vsebuje osnovne vrednosti za difuzijske koeficiente v različnih smereh, in sicer, za vzdolžno (D_L^0) in prečno smer (D_T^0).

Vodne molekule se vežejo na lesene polimerne verige. Med molekulami vode in hidroksilnimi skupinami lesenih polimernih verig nastajajo vodikove vezi. Energija, potrebna za prekinitev teh vezi, E_b, je skladno s [67] enaka:

$$E_b = (38.5 - 29\ m) \cdot 10^3,$$

kjer je vsebnost vlage m definirana kot:

$$m = \frac{c_b}{\rho_0}$$

Plinska mešanica znotraj lesa je sestavljena iz vodne pare in zraka, pri čemer produkti pirolize niso upoštevani. Koncentracija plinske mešanice je na ta način določena kot: $\widetilde{\rho}_g = \widetilde{\rho}_v + \widetilde{\rho}_a$. V konstitucijskih enačbah, ki določajo masni tok vodne pare in zraka, upoštevamo dva različna procesa prenosa snovi. Z Darcyjevim zakonom opišemo konvekcijski prenos plina skozi porozno snov, ki je posledica gradienta pritiska. Dodatno upoštevamo še Fickov zakon, s katerim opišemo difuzijo med vodno paro in zrakom. Masna tokova tako določimo na naslednji način:

$$\mathbf{J}_a = \varepsilon_g \widetilde{\rho}_a \mathbf{v}_g - \varepsilon_g \widetilde{\rho}_g \mathbf{D}_{av} \nabla \left(\frac{\widetilde{\rho}_a}{\widetilde{\rho}_g}\right).$$
$$\mathbf{J}_v = \varepsilon_g \widetilde{\rho}_v \mathbf{v}_g - \varepsilon_g \widetilde{\rho}_g \mathbf{D}_{va} \nabla \left(\frac{\widetilde{\rho}_v}{\widetilde{\rho}_g}\right).$$

Hitrost plinske mešanice lahko skladno z Darcyjevim zakonom zapišemo kot:

$$\mathbf{v}_g = \frac{\mathbf{K} K_g}{\mu_g} \nabla P_g.$$

Matrika $\mathbf{K}$ vsebuje prepustnosti suhega lesa za različne materialne smeri, K_g je relativna prepustnost plinske mešanice v lesu, μ_g je dinamična viskoznost te faze, ∇P_g pa gradient pritiska plinske mešanice.

V skladu z Daltonovim zakonom, je tlak plinske mešanice enak vsoti delnega tlaka zraka in vodne pare $P_g = P_a + P_v$. Predpostavimo, da lahko delne pritiske z zadostno natančnostjo opišemo s splošno plinsko enačbo [37]:

$$P_a = R_a \widetilde{\rho}_a T,$$

$$P_v = R_v \widetilde{\rho}_v T.$$

Difuzijski koeficient zraka v vodni paro $\mathbf{D}_{va}$ je enak difuzijskemu koeficientu vodne pare v zrak $\mathbf{D}_{av}$. Določimo ga kot [68]:

$$\mathbf{D}_{av} = \zeta 1.87 \left(\frac{T^{2.072}}{P_g} \right) \cdot 10^{-5},$$

kjer ζ predstavlja redukcijski faktor zaradi ovirane difuzije v celični strukturi lesa in je odvisen smeri.

Sorpcija

Sorpcija se pojavi ko nastopi razlika med potencialom vlage v celični steni in vlage v celičnem lumnu. Formulacijo za sorpcijo, ki jo je predlagal Frandsen [73], modificiramo tako, da je primerna za temperature nad točko vrelišča T_{boil}:

$$\dot{c} = \begin{cases} H_c \left(c_{bl} - c_b \right), & T \leq T_{boil}, \\ H_c \left(0 - c_b \right), & T > T_{boil}. \end{cases}$$

V zgornji enačbi je c_{bl} enakovredna koncentracija vezane vode pri znanem pritisku vodne pare P_v in jo določimo pri ravnovesnem stanju vlage prek sorpcijskih krivulj. Povzeto po [73] je funkcija, ki določa hitrost sorpcije H_c, naslednja:

$$H_c = \begin{cases} C_1 \exp\left(-C_2 \left(\frac{c_{bl}}{c_b} \right)^{C_3} \right) + C_4, & c_b \leq c_{bl}, \\ C_1 \exp\left(-C_2 \left(2 - \frac{c_{bl}}{c_b} \right)^{C_3} \right) + C_4, & c_b > c_{bl}, \end{cases}$$

kjer je

$$C_2 = C_{21} \exp\left(C_{22} h \right).$$

Koeficienti $C_1 - C_4$ predstavljajo parametre modela.

Ravnovesno stanje vlage sledi Anderson-McChartyijevi sorpcijski izotermi [74], kjer so adsorpcijske ($k = a$) in desorpcijske ($k = d$) krivulje opredeljene kot:

$$\frac{c_{bl}}{\rho_0} = \frac{\ln(\ln(1/h)/f_1^k)}{f_2^k}.$$

V zgornji enačbi, h označuje relativno vlažnost, ki je definirana kot razmerje med tlakom vodne pare P_v in njenim nasičenim parnim tlakom P_s pri dani temperaturi, f_i^k pa so parametri, ki določajo obliko adsorpcijske ali desorpcijske izoterme. Definirani so kot:

$$f_i^k = \sum_{j=0}^{n} b_{ij}^k T^j, \qquad i \in \{1,2\}.$$

Parametri b_{ij} so kalibrirani na osnovi desorpcijske izoterme, ki jo je eksperimentalno določil Kelsey [75].

Robni pogoji

Na stiku med lesom in okolico ali zoglenelo plastjo predpostavimo, da je pritisk v lumnih enak pritisku okolice $P_{g,\infty}$:

$$P_g = P_{g,\infty}.$$

Toplotni površinski pretok na robni ploskvi med lesom in okolico je predpisan na naslednji način:

$$h_{cr} = k\frac{\partial T}{\partial n},$$

kjer $\frac{\partial T}{\partial n}$ predstavlja temperaturni gradient v smeri normale na robno ploskev, h_{cr} je toplotni površinski pretok na robni ploskvi, sestavljen iz konvekcijskega in radiacijskega dela: $h_{cr} = h_c + h_r$. Toplotni pretok zaradi konvekcije je določen kot:

$$h_c = \alpha_c \left(T_\infty - T_m\right),$$

kjer je α_c konvekcijski prestopni koeficient, T_∞ je temperatura okolice, T_m pa je temperatura na površini lesa izpostavljenega požaru. Radiacijski toplotni pretok je določen v skladu s Stefan-Boltzmannovim zakonom:

$$h_r = \sigma \varepsilon_m \varepsilon_f \left(T_\infty^4 - T_m^4\right).$$

Z σ označujemo Stefan-Boltzmannovo konstanto, ε_m predstavlja emisivnost površine lesa, ε_f pa emisivnost plamena.

Izmenjava vodne pare v lumnih z vodno paro v okolici, je opisana s tokom vodne pare na robni ploskvi med lesom in okolico:

$$\mathbf{n} \cdot \mathbf{J}_v = -k_c \left(\widetilde{\rho}_{v,\infty} - \widetilde{\rho}_v\right),$$

kjer $\widetilde{\rho}_{v,\infty}$ predstavlja koncentracijo vodne pare v okolici, $\mathbf{n}$ je enotski vektor normale na zunanjo površino lesa in k_c je masni prestopni koeficient [68] definiran kot:

$$k_c = \frac{\alpha_c}{\widetilde{\rho}_a C_a}\left(\frac{D_{av}}{\alpha_{air}}\right)^{2/3}.$$

α_{air} je termična difuzivnost zraka.

Vezana voda se nahaja v celični steni lesa in se z okolico izmenjuje samo prek sorpcije. Zato je uporabljen Neumannov robni pogoj :

$$\mathbf{n} \cdot \mathbf{J}_b = 0.$$

Sistem diferencialnih enačb in formulacija metode končnih elementov

Sistem osnovnih enačb prevajanja toplote in vlage je nelinearen, zato analitična rešitev praviloma ni znana. Za reševanje nelinearnih parcialnih diferencialnih enačb se uporabljajo numerične metode. V doktorski disertaciji uporabimo metodo končnih elementov. V ta namen je potrebno osnovne enačbe problema skupaj s konstitucijskimi zakoni preurediti, tako da so primerne za metodo končnih elementov. Izbrane osnovne neznanke povezanega modela prenosa toplote in vlage so: temperatura T, pritisk plinske mešanice P_g, koncentracija vodne pare $\widetilde{\rho}_v$ in koncentracija vezane vode c_b. Sistem diferencialnih enačb za povezan model prenosa toplote in vlage, izražen z osnovnimi neznankami je:

$$\begin{aligned}
&C_{TT}\frac{\partial T}{\partial t}+(0)\frac{\partial P_g}{\partial t}+(0)\frac{\partial \widetilde{\rho}_v}{\partial t}+C_{TB}\frac{\partial c_b}{\partial t}= \\
&\qquad =\nabla\cdot\left(K_{TT}\nabla T+(0)\nabla P_g+(0)\nabla\widetilde{\rho}_v+K_{TB}\nabla c_b\right)-K_{TVV}\nabla T, \\
&C_{AT}\frac{\partial T}{\partial t}+C_{AP}\frac{\partial P_g}{\partial t}+C_{AV}\frac{\partial \widetilde{\rho}_v}{\partial t}+(0)\frac{\partial c_b}{\partial t}= \\
&\qquad =\nabla\cdot\left(K_{AT}\nabla T+K_{AP}\nabla P_g+K_{AV}\nabla\widetilde{\rho}_v+(0)\nabla c_b\right), \\
&(0)\frac{\partial T}{\partial t}+(0)\frac{\partial P_g}{\partial t}+C_{VV}\frac{\partial \widetilde{\rho}_v}{\partial t}+(0)\frac{\partial c_b}{\partial t}= \\
&\qquad =\nabla\cdot\left(K_{VT}\nabla T+K_{VP}\nabla P_g+K_{VV}\nabla\widetilde{\rho}_v+(0)\nabla c_b\right)-\dot{c}, \\
&(0)\frac{\partial T}{\partial t}+(0)\frac{\partial P_g}{\partial t}+(0)\frac{\partial \widetilde{\rho}_v}{\partial t}+C_{BB}\frac{\partial c_b}{\partial t}= \\
&\qquad =\nabla\cdot\left(K_{BT}\nabla T+(0)\nabla P_g+(0)\nabla\widetilde{\rho}_v+K_{BB}\nabla c_b\right)+\dot{c}.
\end{aligned}$$

Matematični postopki s katerimi pretvorimo osnovne enačbe skupaj s konstitucijami zvezami v zgoraj zapisani sistem diferencialnih enačb izražen z osnovnimi neznankami, so podrobneje opisani v [94].

Sistem differencialnih enačb izražen z osnovnimi neznankami lahko v matrični obliki zapišemo kot:

$$\mathbf{C}\dot{\mathbf{u}}-\nabla\cdot\left(\mathbf{K}_{ij}\nabla\mathbf{u}\right)+\mathbf{K}_V\nabla\mathbf{u}=\mathbf{F}_s,$$

kjer robne pogoje zapišemo kot:

$$\frac{\partial\mathbf{u}}{\partial n}=\mathbf{F}_\infty-\mathbf{F}_k\mathbf{u},$$

začetni pogoji pa so:

$$\mathbf{u}=\mathbf{u}_0.$$

Zgoraj je $\mathbf{u}$ vektor osnovnih neznank, $\mathbf{u}=\left[T\ P_g\ \widetilde{\rho}_v\ c_b\right]$, matriki $\mathbf{C}$ in $\mathbf{K}_{ij}$ vsebujejo koeficiente C_{ij} in K_{ij} $(i=T,A,V,B,j=T,P,V,B)$, ki so določeni v [94], matrika $\mathbf{K}_V$ vsebuje člene zaradi prenosa toplote s konvekcijo plinov, $\mathbf{F}_s$ je vektor, ki vsebuje stopnjo sorpcije, $\mathbf{F}_s=[0\ 0\ -\dot{c}\ \dot{c}]$, matriki $\mathbf{F}_\infty$ in $\mathbf{F}_k$ vsebujeta člene ki nastopijo zaradi robnih pogojev in $\mathbf{u}_0=\left[T_0\ P_{g,0}\ \widetilde{\rho}_{v,0}\ c_{b,0}\right]$ je vektor začetnih vrednosti osnovnih neznank pri času $t=0$.

Pri metodi končnih elementov celotno računsko domeno razdelimo na končno število elementov. Osnovne neznanke pri času t po vsakem elementu aproksimiramo kot funkcije vozliščnih neznank:

$$\mathbf{u} = \sum_{i=1}^{n_{nodes}} \mathbf{N}\,\mathbf{y}^i,$$

kjer **y** predstavlja vektor diskretnih vozliščnih neznank, **N** pa je matrika oblikovnih funkcij izoparametričnega 4-vozliščnega končnega elementa:

$$N_1 = 1/4(1-\xi)(1-\eta),$$

$$N_2 = 1/4(1+\xi)(1-\eta),$$

$$N_3 = 1/4(1+\xi)(1+\eta),$$

$$N_4 = 1/4(1-\xi)(1+\eta),$$

kjer ξ in η zavzemata vrednosti na intervalu $[-1, 1]$.

Z uporabo Galerkinove metode in integracije po delih [46], lahko sistem diferencialnih enačb, izražen z osnovnimi neznankami, prevedemo na sistem diferencialnih enačb prvega reda:

$$\hat{\mathbf{C}}\dot{\mathbf{y}} + \hat{\mathbf{K}}\mathbf{y} = \hat{\mathbf{F}},$$

kjer je:

$$\hat{\mathbf{C}} = \sum_{e=1}^{n_{el}} \hat{\mathbf{C}}^e, \quad \hat{\mathbf{K}} = \sum_{e=1}^{n_{el}} \hat{\mathbf{K}}^e + \hat{\mathbf{K}}_V^e + \hat{\mathbf{K}}_F^e, \quad \hat{\mathbf{F}} = \sum_{e=1}^{n_{el}} \hat{\mathbf{F}}^e + \hat{\mathbf{F}}_s^e, \quad \mathbf{u} = \sum_{e=1}^{n_{el}} \mathbf{u}^e,$$

$$\hat{\mathbf{C}}^e = \int_{\Omega_e} \mathbf{N}^T \mathbf{C}^e \mathbf{N} d\Omega, \quad \hat{\mathbf{K}}^e = \int_{\Omega_e} \nabla\mathbf{N}^T \mathbf{K}^e \nabla\mathbf{N} d\Omega, \quad \hat{\mathbf{K}}_V^e = \int_{\Omega_e} \mathbf{N}^T \mathbf{K}_V^e \nabla\mathbf{N} d\Omega,$$

$$\hat{\mathbf{K}}_F^e = \int_{\Gamma_e} \mathbf{N}^T \mathbf{K}^e \mathbf{F}_k^e \mathbf{N} d\Gamma, \quad \hat{\mathbf{F}}^e = \int_{\Gamma_e} \mathbf{N}^T \mathbf{K}^e \mathbf{F}_\infty^e d\Gamma, \quad \hat{\mathbf{F}}_s^e = \int_{\Omega_e} \mathbf{N}^T \mathbf{F}_s^e d\Omega,$$

$$\mathbf{C}^e = \begin{bmatrix} C_{TT} & 0 & 0 & C_{TB} \\ C_{AT} & C_{AP} & C_{AV} & 0 \\ 0 & 0 & C_{VV} & 0 \\ 0 & 0 & 0 & C_{BB} \end{bmatrix}, \quad \mathbf{K}^e = \begin{bmatrix} K_{TT} & 0 & 0 & K_{TB} \\ K_{AT} & K_{AP} & K_{AV} & 0 \\ K_{VT} & K_{VP} & K_{VV} & 0 \\ K_{BT} & 0 & 0 & K_{BB} \end{bmatrix},$$

$$\mathbf{K}_V^e = \begin{bmatrix} K_{TVV} & 0 & 0 & 0 \\ 0 & 0 & 0 & 0 \\ 0 & 0 & 0 & 0 \\ 0 & 0 & 0 & 0 \end{bmatrix}, \quad \mathbf{F}_s^e = \begin{Bmatrix} 0 \\ 0 \\ -\dot{c} \\ \dot{c} \end{Bmatrix}, \quad \mathbf{u} = \begin{Bmatrix} T \\ P_g \\ \widetilde{\rho}_v \\ c_b \end{Bmatrix},$$

$$\mathbf{F}_\infty^e = \begin{Bmatrix} F_{T,\infty} \\ 0 \\ F_{v,\infty} \\ 0 \end{Bmatrix}, \quad \mathbf{F}_k^e = \begin{bmatrix} \frac{h_{cr}^*}{K_{TT}} & 0 & 0 & 0 \\ 0 & 0 & 0 & 0 \\ 0 & 0 & \frac{k_c}{K_{VV}} & 0 \\ 0 & 0 & 0 & 0 \end{bmatrix}.$$

Zgoraj Ω_e predstavlja domeno končnega elementa, Γ_e pa ja rob končnega elementa na katerem predpišemo robne pogoje. Za časovno diskretizacijo uporabimo diferenčno shemo. V vsakem časovnem intervalu $[t^{k-1}, t^k]$ predpostavimo, da se vozliščne količine spreminjajo linearno. Sistem diferenicalnih enačb prvega reda $\left(\hat{\mathbf{C}}\dot{\mathbf{y}} + \hat{\mathbf{K}}\mathbf{y} = \hat{\mathbf{F}}\right)$ rešujemo v vsakem časovnem koraku, t.j., pri času $t^k = t^{k-1} + \mu\delta t$, kjer je δt časovni prirastek, μ pa je brezdimenzijski časovni parameter, ki določa, v kateri točki znotraj časovnega intervala zadostimo enačbam. V doktorski nalogi upoštevamo implicitno metodo, za katero velja da $\mu = 1$. Ko v enačbi $\hat{\mathbf{C}}\dot{\mathbf{y}} + \hat{\mathbf{K}}\mathbf{y} = \hat{\mathbf{F}}$ upoštevamo časovno diskretizacijo, dobimo končni sistem, ki ga iterativno rešujemo v vsakem časovnem koraku:

$$\widetilde{\mathbf{C}}^k \mathbf{y}^k = \widetilde{\mathbf{F}}^k, \tag{7.1}$$

kjer je

$$\widetilde{\mathbf{C}}^k = \hat{\mathbf{K}} + \frac{1}{\delta t}\hat{\mathbf{C}}, \tag{7.2}$$

in

$$\widetilde{\mathbf{F}}^k = \frac{1}{\delta t}\hat{\mathbf{C}}\mathbf{y}^{k-1} + \hat{\mathbf{F}}^k. \tag{7.3}$$

OSNOVNE ENAČBE ZA UKRIVLJEN NOSILEC IN NOSILEC S SPREMENLJIVO VIŠINO

Matematični model, s katerim opišemo deformiranje nosilca temelji na Reissnerjevem kinematično točnem modelu nosilca [48]. V modelu je upoštevan vpliv membranske, strižne in upogibne deformacije na deformiranje nosilca. Upoštevana je Timoshenkova hipoteza, ki predpostavlja, da prečni prerez ostane raven, vendar ne več pravokoten na referenčno os nosilca v deformirani legi. Poleg tega je upoštevano, da se oblika in velikost prečnega prereza med deformiranjem ne spreminja. V skladu z Reissnerjevim modelom nosilca je napetostno in deformacijsko stanje nosilca določeno z reševanjem sistema kinematičnih, ravnotežnih in konstitucijskih enačb skupaj s pripadajočimi robnimi pogoji. Kinematične enačbe predstavljajo zveze med deformacijskimi količinami $(\varepsilon, \gamma, \kappa)$ in kinematičnimi količinami (u, w, φ) ter jih zapišemo na naslednji način:

$$X' + u' - (1+\varepsilon)\cos\varphi - \gamma\sin\varphi = 0,$$

$$Z' + w' + (1+\varepsilon)\sin\varphi - \gamma\cos\varphi = 0,$$

$$\varphi' - \kappa_0 - \kappa = 0,$$

kjer s predstavlja naravni parameter, s katerim parametriziramo ukrivljen nosilec, $()'$ predstavlja odvod po parametru s, $\varepsilon(s)$ in $\varphi(s)$ sta specifična sprememba dolžine in zasuk referenčne osi nosilca, $\gamma(s)$ je strižna deformacija, κ predstavlja psevdoukrivljenost referenčne osi nosilca, κ pa je začetna ukrivljenost referenčne osi nosilca.

Ravnotežne enačbe med seboj povezujejo notranje statične količine in zunanjo obtežbo. Ob upoštevanju, da na nosilec deluje konservativna linijska obtežba $\mathbf{p} = p_X\mathbf{E}_X + p_Z\mathbf{E}_Z$ in konservativni linijski moment $\mathbf{m} = m_Y\mathbf{E}_Y$, lahko ravnotežne enačbe zapišemo kot:

$$R'_X + p_X = 0,$$

$$R'_Z + p_Z = 0,$$

$$M'_Y - (1+\varepsilon)Q + \gamma N + m_Y = 0,$$

kjer sta R_X in R_Z komponenti ravnotežne osne sile N in prečne sile Q, v smeri X in Z, M_Y je ravnotežni moment. Ravnotežno osno in prečno silo določimo iz naslednje zveze:

$$N = R_X \cos\varphi - R_Z \sin\varphi,$$

$$Q = R_X \sin\varphi + R_Z \cos\varphi.$$

Zadnji sklop enačb ukrivljenega ravninskega nosilca predstavljajo konstitucijske enačbe, ki povezujejo ravnotežne sile (N, Q, M_Y) z deformacijskimi količinami $(\varepsilon, \gamma, \kappa)$:

$$N_\mathrm{c} - N = 0,$$

$$Q_\mathrm{c} - Q = 0,$$

$$M_\mathrm{c} - M_Y = 0,$$

kjer sta N_c in Q_c konstitucijska osna in prečna sila, M_c pa je konstitucijski moment. Konstitucijske količine določimo v odvisnosti od normalne in strižne napetosti, σ in τ:

$$N_\mathrm{c} = \int_{A(s)} \sigma\,(s,\eta,\zeta)\,dA,$$
$$Q_\mathrm{c} = \int_{A(s)} \tau\,(s,\eta,\zeta)\,dA,$$
$$M_\mathrm{c} = \int_{A(s)} \zeta\sigma\,(s,\eta,\zeta)\,dA,$$

kjer A označuje prečni prerez nosilca. Konstitucijske količine N_c, Q_c in M_c sledijo izbranim materialnem modelom, ki so definirani iz zveze med vzdolžno normalno napetostjo σ in mehansko deformacijo D_σ ter med strižno napetostjo τ in strižno deformacijo γ. Materialne modele definiramo z izrazoma:

$$\sigma(s,\eta,\zeta) = \mathscr{F}\big(D_\sigma(s,\eta,\zeta), T(s,\eta,\zeta), m(s,\eta,\zeta)\big),$$

$$\tau(s,\eta,\zeta) = \mathscr{G}\big(\gamma(s,\eta,\zeta), T(s,\eta,\zeta), m(s,\eta,\zeta)\big).$$

V splošnem funkciji $\mathscr{F}$ in $\mathscr{G}$ določamo na podlagi eksperimentalnih raziskav. Ob upoštevanju enostavnega strižnega modela lahko izračun konstitucijske prečne sile poenostavimo v [47, 95]:

$$Q_\mathrm{c}(\gamma(s)) = G(T) A_\mathrm{s} \gamma,$$

kjer je $G(T)$ strižni modul, A_s pa strižni prerez. Pri tem je vpliv vlage na strižni modul zanemarjen, po prečnem prerezu nosilca pa je predpostavljena konstantna strižna deformacija.

Osnovni sistem enačb za mehanski del požarne analize ukrivljenih lesenih nosilcev, je dopolnjen z robnimi pogoji:

$s = 0$:

$$S_1 + R_X(0) = 0 \qquad \text{ali} \qquad u(0) = u_1,$$

$$S_2 + R_Z(0) = 0 \qquad \text{ali} \qquad w(0) = u_2,$$

$$S_3 + M_Y(0) = 0 \qquad \text{ali} \qquad \varphi(0) = u_3,$$

$s = L$:

$$S_4 - R_X(L) = 0 \qquad \text{ali} \qquad u(L) = u_4,$$

$$S_5 - R_Z(L) = 0 \qquad \text{ali} \qquad w(L) = u_5,$$

$$S_6 - M_Y(L) = 0 \qquad \text{ali} \qquad \varphi(L) = u_6,$$

kjer u_j, $j = 1,2,...,6$ predstavlja predpisane posplošene robne pomike in S_j, $j = 1,2,...,6$ označuje predpisane posplošene robne sile.

Reševanje enačb ukrivljenega nosilca

Sistem osnovnih algebrajsko-diferencialnih enačb ukrivljenega nosilca lahko analitično rešimo samo v posebnih primerih pri sobni temperaturi. V našem primeru se srečamo z geometrijsko in materialno nelinearnostjo, zato analitična rešitev ni možna. Zaradi tega je sistem osnovnih enačb ukrivljenega nosilca rešen numerično z metodo končnih elementov (MKE). Pri tem je uporabljen deformacijski končni element, ki temelji na interpolaciji deformacijskih količin [39]. Izpeljavo deformacijskega končnega elementa za ukrivljen nosilec, ki temelji na Galerkinovi metodi končnih elementov, je v svoji doktorski disertaciji podrobno predstavil Čas [47]. Galerkinovo metodo uporabimo tudi v našem primeru. Ker je sam postopek izpeljave metode končnih elementov zelo podoben kot v [47], v nadaljevanju prikazujemo le osnovne korake za formulacijo deformacijskega končnega elementa. Osnovne enačbe za metodo končnih elementov izpeljemo na podlagi modificiranega principa virtualnega dela [47]:

$$\begin{aligned}
\delta W^* = \int_0^L \left((N_c - N)\,\delta\varepsilon + (Q_c - Q)\,\delta\gamma + (M_c - M_Y)\,\delta\kappa\right) ds + \\
+ \left(u(L) - u(0) + \Delta X_L - \int_0^L \left((1+\varepsilon)\cos\varphi + \gamma\sin\varphi\right) ds\right) \delta R_X(0) + \\
+ \left(w(L) - w(0) + \Delta Z_L - \int_0^L \left((1+\varepsilon)\sin\varphi - \gamma\cos\varphi\right) ds\right) \delta R_Z(0) + \\
+ \left(\varphi(L) - \varphi(0) - \int_0^L (\kappa + \kappa_0)\, ds\right) \delta M_Y(0) + \\
+ (S_1 + R_X(0))\,\delta u(0) + (S_2 + R_Z(0))\,\delta w(0) + (S_3 + M_Y(0))\,\delta\varphi(0) + \\
+ (S_4 - R_X(L))\,\delta u(L) + (S_5 - R_Z(L))\,\delta w(L) + (S_6 - M_Y(L))\,\delta\varphi(L) = 0.
\end{aligned}$$

Deformacijske količine $\varepsilon, \gamma, \kappa$, posplošene robne sile $R_X(0), R_Z(0), M_Y(0)$ in posplošeni robni pomiki $u(0), w(0), \varphi(0), u(L), w(L), \varphi(L)$ so osnovne neznanke problema. Deformacijske količine, ki so odvisne od naravnega parametra s, interpoliramo po končnem elementu, kjer za interpolacijo izberemo Lagrangeve polinome. Interpolacijske nastavke ter njihove variacije zapišemo kot:

$$\varepsilon(s) = \sum_{m=1}^{M} P_m(s)\varepsilon_m, \qquad \delta\varepsilon(s) = \sum_{m=1}^{M} P_m(s)\delta\varepsilon_m,$$
$$\gamma(s) = \sum_{m=1}^{M} P_m(s)\gamma_m, \qquad \delta\gamma(s) = \sum_{m=1}^{M} P_m(s)\delta\gamma_m,$$
$$\kappa(s) = \sum_{m=1}^{M} P_m(s)\kappa_m, \qquad \delta\kappa(s) = \sum_{m=1}^{M} P_m(s)\delta\kappa_m,$$

kjer $\varepsilon_m, \gamma_m, \kappa_m$ predstavljajo vrednosti neznank v interpolacijskih točkah, $P_m(m = 1, 2, ..., M)$ pa so Lagrangevi polinomi reda $(M-1)$. Ob vstavitvi zgornjih nastavkov v modificiran izrek o virtualnem delu, dobimo sistem Euler-Lagrangevih enačb za končni element:

$$g_m = \int_0^L (N_c - N)\, P_m ds = 0,$$
$$g_{M+m} = \int_0^L (Q_c - Q)\, P_m ds = 0,$$
$$g_{2M+m} = \int_0^L (M_c - M_Y)\, P_m ds = 0,$$
$$g_{3M+1} = u(L) - u(0) + \Delta X_L - \int_0^L ((1+\varepsilon)\cos\varphi + \gamma\sin\varphi)\, ds = 0,$$
$$g_{3M+2} = w(L) - w(0) + \Delta Z_L - \int_0^L ((1+\varepsilon)\sin\varphi - \gamma\cos\varphi)\, ds = 0,$$
$$g_{3M+3} = \varphi(L) - \varphi(0) - \int_0^L (\kappa + \kappa_0)\, ds = 0,$$
$$g_{3M+4} = S_1 + R_X(0) = 0,$$
$$g_{3M+5} = S_2 + R_Z(0) = 0,$$
$$g_{3M+6} = S_3 + M_Y(0) = 0,$$
$$g_{3M+7} = S_4 - R_X(0) + \int_0^L p_X ds = 0,$$
$$g_{3M+8} = S_5 - R_Z(0) + \int_0^L p_z ds = 0,$$
$$g_{3M+9} = S_6 - M_Y(0) - \int_0^L ((1+\varepsilon)Q - \gamma N - m_Y)\, ds = 0.$$

Za izvrednotenje integralov v zgodnjih enačbah uporabimo Gaussovo numerično integracijo. Zgornje enačbe tvorijo sistem $3M+9$ nelinearnih algebrajskih enačb za $3M+9$ neznank. Med temi je $3M+3$ notranjih prostostnih stopenj $\varepsilon_m(m = 1, ..., M), \gamma_m(m = 1, ..., M), \kappa_m(m = 1, ..., M), R_X(0), R_Z(0), M_Y(0)$ ter šest zunanjih prostostnih stopenj $u(0), w(0), \varphi(0), u(L), w(L), \varphi(L)$ končnega elementa. Zaradi bolj

učinkovitega numeričnega izračuna notranje prostostne stopnje kondenziramo, zunanje pa združimo v enačbo konstrukcije:

$$\mathbf{G}(\mathbf{x}^i, \lambda^i, T^i, m^i) = 0,$$

kjer je $\mathbf{x}^i$ vektor posplošenih pomikov pri času t^i, sestavljen iz vozliščih pomikov in zasukov ukrivljenega nosilca, λ^i predstavlja obtežni faktor, T^i je temperaturno polje ter m^i je vlažnostno polje konstrukcije. Algebrajski sistem nelinearnih enačb rešimo z Newtonovo inkrementno-iteracijsko metodo. Popravke prirastkov posplošenih pomikov $\delta\mathbf{x}^i$ do želene natančnosti določamo znotraj časovnega inkrementa $\left[t^{i-1}, t^i\right]$ pri znanem temperaturnem polju T^i, vlažnostnem polju m^i in obtežnem faktorju λ^i.

$$\Delta_x \mathbf{G}(\mathbf{x}^{i-1} + \Delta\mathbf{x}_h^i, \lambda^i, T^i, m^i) = -\mathbf{G}(\mathbf{x}^{i-1} + \Delta\mathbf{x}_h^i, \lambda^i, T^i, m^i),$$

$$\Delta\mathbf{x}_{h+1}^i = \Delta\mathbf{x}_h^i + \delta\mathbf{x}_{h+1}^i.$$

Zgoraj $\Delta_x \mathbf{G} = \mathbf{K}_{T,h}^k$ predstavlja tangentno togostno matriko konstrukcije. Porušitev konstrukcije nastopi, ko togostna matrika konstrukcije postane singularna $\Delta_x \mathbf{G} = 0$.

ZAKLJUČEK

V doktorski disertaciji je predstavljen nov numerični model za nelinearno analizo ukrivljenega lesenega nosilca s spremenljivo višino. Numerični model je razdeljen v tri faze. V prvi fazi določamo obnašanje požara znotraj požarnega sektorja kjer uporabimo bodisi standardizirane požarne krivulje, bodisi napredno programsko opremo Fire Dynamics Simulator [45].

Osrednja temo doktorske disertacije je druga faza numeričnega modela, kjer je predstavljen nov matematični in numerični model za določitev povezanega prenosa toplote in vlage po lesenem nosilcu izpostavljenem požaru. Osnovne enačbe so rešene numerično z metodo končnih elementov, ki je bila razvita v programskem okolju Matlab. Razvito programsko orodje omogoča določitev razvoja temperature, pritiskov, koncentracije vodne pare in koncentracije vezane vode po prečnem prerezu lesenega nosilca. Z ustrezno validacijo modela in parametričnimi študijami je bilo ugotovljeno:

- konvergenčni test je pokazal, da mora biti velikost končnega elementa 2.5 mm ali manj, da dovolj natančno določimo debelino zoglenele plasti,
- z validacijo numeričnih rezultatov z eksperimentom, ki so ga izvedli König in Walleij [77] ter Lache [78], je bilo prikazano da numerični model omogoča natančno določitev temperaturnega polja lesenega elementa izpostavljenega požaru,
- dobro ujemanje numeričnih in eksperimentalnih rezultatov je bilo odkrito z validacijo debeline zoglenele plasti. Poleg tega, se je predpostavka, da temperatura oglenenja za požare z režimom ogrevanja podobnim ISO požaru znaša 300°C, izkazala za pravilno,
- različna začetna vsebnost vlage lesa ima pomemben vpliv na razvoj temperatur. Višja začetna vsebnost vlage povzroči počasnejši razvoj temperatur po lesenem elementu.

- analiza občutljivosti modela za povezan prenos toplote in vlage je pokazala dve poglavitni lastnosti modela: Prvič, odkrit je bil velik vpliv difuzije vezane vode (D_0) na skupno vsebnost vlage lesa. Drugič, izkazalo se je, da konvekcijski prenos toplote nima pomembnega vpliva na razvoj temperature po lesenem elementu, zato smo, da bi povečali hitrost izračuna, hkrati pa ohranili natančnost modela, ta člen v energijski enačbi zanemarili.

Tretjo fazo numeričnega modela predstavlja mehanski model za analizo lesenega ukrivljenega nosilca s spremenljivo višino hkrati izpostavljenega statični in požarni obtežbi. Deformiranje nosilca je matematično opisano z Reissnerjevo kinematično točno teorijo nosilca [48], kjer je upoštevan vpliv membranske, strižne in upogibne deformacije na deformiranje nosilca. Osnovne enačbe so diskretizirane z Galerkinovo metodo končnih elementov, rešujemo pa jih z Newtonovo inkremento-iteracijsko metodo. Na podlagi različnih parametričnih študij ter validacije modela, so podani naslednji zaključki:

- mehanski model je primeren za požarno analizo ukrivljenega lesenega nosilca s spremenljivo višino,
- z vidika kriterija porušitve, naknadno izračunane normalne napetosti pravokotno na vlakna, izračunane s predstavljenim modelom nosilca, zadovoljivo opišejo normalne napetosti pravokotno na vlakna, določene z 2D modelom končnih elementov,
- različni nivoji začetne vsebnosti vlage imajo velik vpliv na obnašanje lesenega nosilca med požarom. Višja začetna vsebnost vlage povzroči kasnejšo porušitev nosilca.

Poleg trifaznega numeričnega modela, doktorska disertacija ponuja tudi metodologijo za določitev zanesljivosti lesenega nosilca, izpostavljenega požaru. Analiza zanesljivosti je bila opravljena z metodo Monte Carlo, kjer je bila z namenom, da bi zmanjšali število simulacij, uporabljena metoda vzorčenja v latinski hiperkocki (latin hypercube sampling). V analizi sta bili upoštevani dve različni požarni krivulji in sicer standardna ISO krivulja ter parametrična požarna krivulja. V obeh primer so bile negotovosti upoštevane z naključno generiranimi parameteri za toplotno in mehansko analizo. S parametrično krivuljo smo še dodatno upoštevali negotovo obnašanje požara. Z analizo zanesljivosti je bilo ugotovljeno, da uporaba standardne ISO krivulje ni vedno na varni strani. Ob upoštevanju parametrične požarne krivulje, ki bolje opiše razvoj realnega požara, se izkaže, da je v primerjavi z ISO krivuljo v določenih primerih razvoj temperatur v požarnem sektorju precej hitrejši. To posledično lahko privede do hitrejše porušitve nosilca.

BIBLIOGRAPHY

[1] Thelandersson, S., Larsen, H. J. 2003. Timber Engineering. Chichester, John Wiley & Sons: 446 p.

[2] Dalton, J. Olympic Countdown Begins. <https://literallife.wordpress.com/2010/01/25/olympic-countdown-begins/>(Acquired: 23.7.2015).

[3] Premrov, M., Dobrila, P. 2008. *Lesene konstrukcije*. Maribor, Univerza v Mariboru, Fakulteta za gradbeništvo: 347 p.

[4] Buchanan, A. H. 2002. Structural Design for Fire Safety. Chichester, John Wiley & Sons: 421 p.

[5] Luikov, A. V. 1966. Heat and mass transfer in capillary porous bodies. Oxford, Pergamon Press: 623 p.

[6] Thomas, H. R., Morgan, K., Lewis, R. W. 1980. A fully nonlinear analysis of heat an mass transfer problems in porous bodies. Int. J. Numer. Meth. Eng. 15: 1381–1393.

[7] Irudayarajomas, J., Haghighi, K., Stroshine, R. L. 1990. Nonlinear finite element analysis of coupled heat and mass transfer problems with an application to timber drying. Drying Technol. 8: 731–749.

[8] Younsi, R., Kocaefe, D., Poncsak, S., Kocaefe, Y. 2006. Thermal modelling of the high temperature treatment of wood based on Luikov's approach. Int. J. Energ. Res. 30: 699–711.

[9] Younsi, R., Kocaefe, D., Poncsak, S., Kocaefe, Y. 2006. A diffusion-based model for transient high temperature treatment of wood. J. of Build. Mater. 30: 113–135.

[10] Kocaefe, D., Younsi, R., Chaudry, B., Kocaefe, Y. 2006. Modeling of heat and mass transfer during high temperature treatment of aspen. Wood. Sci. Technol. 40: 371–391.

[11] Schnabl, S. 2007. *Mehanska in požarna analiza kompozitnih nosilcev*. Doktorska disertacija, Univerza v Ljubljani, Fakulteta za gradbeništvo in geodezijo, Oddelek za gradbeništvo, Konstrukcijska smer: 109 str.

[12] Di Blasi, C. 1998. Multi-phase moisture transfer in the high-temperature drying of wood particles. Chem. Eng. Sci. 53: 353–366.

[13] Johansson, A., Fyhr, C., Rasmuson, A. 1997. High temperature convective drying of wood chips with air and superheated steam. Int. J. Heat Mass Transfer 40: 2843–2858.

[14] Perré, P., Turner, I. A. 1999. A 3-D version of Transpore: a comprehensive heat and mass transfer computational model for simulating the drying of porous media. Int. J. Heat Mass Transfer 42: 4501–4521.

[15] Perré, P., Moser, M., Martin, M. 1993. Advances in transport phenomena during convective drying with superheated steam and moist air. Int. J. Heat Mass Transfer 36: 2725–2746.

[16] Nijdam, J. J., Langrish, T. A. G., Keey, R. B. 2000. A high-temperature drying model for softwood timber. Chem. Eng. Sci. 55: 3585–3598.

[17] EN 1995-1-2 2005, Eurocode 5: Design of Timber Structures - Part 1-2: General - Structural Fire Design. European committee for standardisation. Brussels: 69 p.

[18] Schaffer, E. L. 1967. Charring rate of selected woods-transverse to grain. Forest Service Research Paper FPL 69. Forest Products Laboratory, Madison, Winsconsin.

[19] Mikkola, E. 1990. Charring of wood. Research reports 689. Espoo, VTT, Technical Research Centre of Finland: 35 p.

[20] White, R., Nordheim, E. 1992. Charring rate of wood for ASTM E 119 exposure. Fire Tech. 28: 5–30.

[21] Lautenberger, C., Fernandez-Pello, C. 2009. Generalized pyrolysis model for combustible solids. Fire Saf. J. 44: 819–839.

[22] Lautenberger, C., Fernandez-Pello, C. 2009. A model for the oxidative pyrolysis of wood. Combust. Flame 156: 1503–1513.

[23] Turner, I., Rousset, P., Rémond, R., Perré, P. 2010. An experimental and theoretical investigation of the thermal treatment of wood (*Fagus sylvatica* L.) in the range 200-260°C. Int. J. Heat Mass Transfer 53: 715–725.

[24] Di Blasi, C. 2008. Modeling chemical and physical processes of wood and biomass pyrolysis. Prog. Energ. Combust. 34: 47–90.

[25] Park, W. C., Atreya, A., Baum, H. R. 2010. Experimental and theoretical investigation of heat and mass transfer processes during wood pyrolysis. Combust. Flame 157: 481–494.

[26] Frangi, A., Knobloch, M., Fontana, M. 2009. Fire design of timber slabs made of hollow core elements. Eng. Struct. 31: 150–157.

[27] Frangi, A., Fontana, M., Hugi, E., Jöbstl, R. 2009. Experimental analysis of cross-laminated timber panels in fire. Fire Saf. J. 44: 1078–1087.

[28] Yang, T. H., Wang, S. Y., Tsai, M. J., Lin, C. Y., Chuang, Y. J. 2009. Effect of fire exposure on the mechanical properties of glued laminated timber. Mater. Des. 30: 698–703.

[29] Zhang, J., Xu, Q. F., Xu, Y. X., Wang, B., Shang, J. X. 2012. A numerical study on fire endurance of wood beams exposed to three-side fire. J. Zhejiang Univ-Sci. A (Appl. Phys. & Eng.) 13: 491–505.

[30] Lennon, T., Hopkin, D., El-Rimawi, J., Silberschmidt, V. 2010. Large scale natural fire tests on protected engineered timber floor systems. Fire Saf. J. 45: 168–182.

[31] Kolaitis, D. I., Asimakopoulou, E. K., Founti, M. A. 2014. Fire protection of light and massive timber elements using gypsum plasterboards and wood based panels: A large-scale compartment fire test. Construct. Build. Mater. 73: 163–170.

[32] Zhu, Z., Kaliske, M. 2010. Modeling of coupled heat, moisture transfer and mechanical deformations of wood during drying process. Eng. Comput. 28: 802–826.

[33] Zhou, H., Zhu, E., Fortino, S., Toratti, T. 2010. Modelling the hygrothermal stress in curved glulam beams. The J. of Strain Anal. for Eng. Design 45: 129–140.

[34] Gams, M. 2003. *Povezan prenos toplote in vlage v poroznem materialu*. Diplomska naloga, Univerza v Ljubljani, Fakulteta za gradbeništvo in geodezijo, Oddelek za gradbeništvo, Konstrukcijska smer: 79 str.

[35] Hozjan, T. 2009. *Nelinearna analiza vpliva požara na sovprežne linijske konstrukcije*. Doktorska disertacija, Univerza v Ljubljani, Fakulteta za gradbeništvo in geodezijo, Oddelek za gradbeništvo, Konstrukcijska smer: 117 str.

[36] Kolšek, J. 2013. *Požarna analiza dvoslojnih kompozitnih linijskih konstrukcij*. Doktorska disertacija, Univerza v Ljubljani, Fakulteta za gradbeništvo in geodezijo, Oddelek za gradbeništvo, Konstrukcijska smer: 113 str.

[37] Tenchev, R. T., Li, L., Purkiss, J. A. 2001. Finite element analysis of coupled heat and moisture transfer in concrete subjected to fire. Numer. Heat Transfer, Part A 39: 685–710.

[38] Davie, C. T., Pearce, C. J., Bičanič, N. 2010. A fully generalised, coupled, multi-phase, hygro-thermo-mechanical model for concrete. Mater. Struct. 43: 13–33.

[39] Planinc, I. 1998. *Račun kritičnih točk konstrukcij s kvadratično konvergentnimi metodami*. Doktorska disertacija, Univerza v Ljubljani, Fakulteta za gradbeništvo in geodezijo, Oddelek za gradbeništvo, Konstrukcijska smer: 83 str.

[40] Schnabl, S., Turk, G., Planinc, I. 2011. Buckling of timber columns exposed to fire. Fire Saf. J. 46: 431–439.

[41] Srpčič, S., Srpčič, J., Saje, M., Turk, G. 2009. Mechanical analysis of glulam beams exposed to changing humidity. Wood. Sci. Technol. 43: 9–22.

[42] Pečenko, R., Svensson, S., Hozjan, T. 2014. influence of heat and mass transport on mechanical behaviour of timber elements in fire. IFireSS – International Fire Safety Symposium, Coimbra.

[43] Audebert, M., Dhima, D., Taazount, M., Bouchaïr, A. 2013. Thermo-mechanical behaviour of timber-to-timber connections exposed to fire. Fire Saf. J. 56: 52–64.

[44] Audebert, M., Dhima, D., Taazount, M., Bouchaïr, A. 2014. Experimental and numerical analysis of timber connections in tension perpendicular to grain in fire. Fire Saf. J. 63: 125–137.

[45] Fire Dynamics Simulator (FDS) and SmokeView (SMV). <http://firemodels.github.io/fds-smv/>(Acquired: 13.7.2013).

[46] Zienkiewicz, O. C., Taylor, R. L. 1991. The finite element method. Vol. 2, Solid and fluid mechanics Dynamics and non-linearity. McGraw-Hill, London.

[47] Čas, B. 2004. *Nelinearna analiza kompozitnih nosilcev z upoštevanjem zdrsa med sloji*. Doktorska disertacija, Univerza v Ljubljani, Fakulteta za gradbeništvo in geodezijo, Oddelek za gradbeništvo, Konstrukcijska smer: 136 str.

[48] Reissner, E. 1972. On one-dimensional finite-strain beam theory: the plane problem. J. Appl. Math. Phys. (ZAMP) 23: 795–804.

[49] Pischl, R. 1980. *Holzbau mit kritischen betractungen und neuen vorschlägen zur bemessung nach theorie 1. und 2. ordnung*. Graz, Technische Universität Graz, Institut für Stahlbau, Holzbau und Flächentragwerke.

[50] Bratina, S., Saje, M., Planinc, I. 2004. On materially and geometrically non-linear analysis of reinforced concrete planar frames. Int. J. Solid. Struct. 41: 7181–7207.

[51] Drysdale, D. 1998. An introduction to fire dynamics - 2nd edition. Chichester, John Wiley & Sons: 451 p.

[52] Quintiere, J. G. 2006. Fundamentals of Fire Phenomena. Chichester, John Wiley & Sons: 439 p.

[53] ISO-834 1999. Fire-Resistance Test-Elements of Building Construction: Part 1. General Requirements. International Organization for Standardization, Geneva, Switzerland.

[54] EN 1991-1-2 2004. Eurocode 1: Actions on structures - Part 1-2: General actions - Actions on structures exposed to fire. European committee for standardisation. Brussels: 56p.

[55] Bailey, C. One Stop Shop in Structural Fire Engineering. <http://www.mace.manchester.ac.uk/project/research/structures/strucfire/Design/performance/fireModelling>(Acquired: 29.6.2015).

[56] McGrattan, K., Hostikka, S., Floyd, J., Baum, H., Rehm, R. 2007. Fire Dynamics Simulator (Version 5) Technical Reference Guide. NIST Special Publication 1018-5. Washington, U.S. Government Printing Office: 86 p.

[57] Ferziger, J. H., Perič, M. 2002. Computarional Methods for Fluid Dynamics. Berlin-Heidelberg-New York, Springer-Verlag: 431 p.

[58] Shah, M., Talukdar, P., Subbarao, P. M. V. 2012. Modeling of gray gas radiation with different shapes of heat source in three-dimensional enclosures. Heat. Tran. Eng. 33: 651–660.

[59] Wang, P., Fan, F., Li, Q. 2014. Accuracy evaluation of the gray gas radiation model in CFD simulation. Case Stud. in Therm. Eng. 3: 51–58.

[60] Rein, G., Empis, A. C., Carvel, R. 2006. The Dalmarnock Fire Test: Experiments and Modelling. Edinburgh, University of Edinburgh, School of Engineering and Electronics.

[61] Huč, S., Rozman, M., Kolšek, J., Hozjan, T. 2015. *Performančni način projektiranja požarne odpornosti lepljenega lesenega nosilca. Del 1, Modeliranje razvoja požara v računalniškem programu FDS*. Gradbeni vestnik 64: 91–100.

[62] QualiSTAT. <http://www.qualistat.com/Hardwood- - -Humidity.html>(Acquired: 16.6.2015).

[63] Frandsen, H. L. 2007. Selected constitutive models for simulating the hygromechanical response of wood. Doctoral dissertation, Aalborg University, Department of Civil Engineering.

[64] Omarsson, S. 1999. Numerical Analysis of Moisture-Related Distorsion in Sawn Timber. Doctoral thesis. Gothenburg, Chalmer University of Technology, Department of Structural Mechanics: 99 p.

[65] Village Life Group.
<http://857756494524377064.weebly.com/ggi-energy-pyrolysis.html >(Acquired: 16.6.2015).

[66] Milla, O.
<http://doctor-biochar.blogspot.com/2013_10_01_archive.html >(Acquired: 16.6.2015).

[67] Siau, J. F. 1995. Wood: influence of moisture on physical properties. Dept. of Wood Science and Forest Products, Virginia Polytechnic Institute and State University.

[68] Cengel, Y. A. 1998. Heat transfer: A practical approach. WCB/McGraw-Hill, New York.

[69] Anderson, N. T., McCharty, J. L. 1977. Simultaneous heat, mass, and momentum transfer in porous media: A theory of drying. Adv. Heat Transfer 13: 119–203.

[70] Time, B. 1998. Hygroscopic Moisture Transport in Wood. Doctoral thesis. Trondheim, Norwegian University of Science and Technology, Department of Building and Constructional Engineering: 216 p.

[71] Skaar, C. 1988. Wood-Water Relations. Springer Berlin Heidelberg, Berlin.

[72] Hozjan, T., Svensson, S. 2011. Theoretical analysis of moisture transport in wood as an open porous hygroscopic material. Holzforschung 65: 97–102.

[73] Frandsen, H. L., Svensson, S. 2007. Implementation of sorption hysteresis in multi-fickian moisture transport. Holzforschung 61: 693–701.

[74] Anderson, N. T., McCharty, J. L. 1963. Two parameter isotherm equation for fiber-water systems. Ind. Eng. Chem. Process Des. Develop. 2: 103–105.

[75] Kelsey, K. E. 1956. The sorption of water vapour by wood. Aust. J. Appl. Sci. 8: 42–54.

[76] Bayley, F. J., Owen, J. M., Turner, A. B. 1972. Heat transfer. Barnes and Noble Book Co., New York.

[77] König, J., Walleij, L. 1999. One-dimensional charring of timber exposed to standard and parametric fires in initially unprotected and postprotection situations. Rapport I 9908029. Insitutet för träteknisk forskning, Stockholm, Sweden.

[78] Lache, M. 1992. *Untersuchungen zur Abbrandgeschwindigkeit von Vollholz und zur Feuerwiderstandsdauer biegebeanspruchter Brettschichtholzträger*. Doctoral disertation, Ludwig-Maximilians-Universität, München.

[79] Yang, T. H., Wang, S. Y., Tsai, M. J., Lin, C. Y. 2009. Temperature distribution within glued laminated timber during a standard fire exposure test. Mater. Des. 30: 518–525.

[80] Yang, T. H., Wang, S. Y., Tsai, M. J., Lin, C. Y. 2009. The charring depth and charring rate of glued laminated timber after a standard fire exposure test. Mater. Des. 44: 518–525.

[81] Le Tallec, P., Laporte, A. 2003. Numerical Methods in Sensitivity Analysis and Shape Optimization. Birkhäuser, Boston.

[82] Saltelli, A., Tarantola, S., Campolongo, F., Ratto, M. 2004. Sensitivity Analysis in Practice: A Guide to Assessing Scientific Models. John Wiley and Sons Ltd, Chichester.

[83] Cariboni, J., Gatelli, D., Liska, R., Saltelli, A. 2007. The role of sensitivity analysis in ecological modelling. Ecol. Model. 203: 167–182.

[84] Feyissa, A. H., Gernaey, K. V., Adler-Nissen, J. 2012. Uncertainty and sensitivity analysis: Mathematical model of coupled heat and mass transfer for a contact baking process. J. Food. Eng. 109: 281–290.

[85] Mayer, L. S., Younger, M. S. 1974. Procedures for estimating standardized regression coefficients from sample data. Socio. Meth. Res. 2: 431–453.

[86] Sin, G., Gernaey, K. V., Lantz, A. E. 2009. Good modeling practice for PAT applications: Propagation of input uncertainty and sensitivity analysis. Biotechnol. Progr. 25: 1043–1053.

[87] Tian, W. 2013. A review of sensitivity analysis methods in building energy analysis. Renew. Sustain. Energ. Rev. 20: 411–416.

[88] Pečenko, R., Huč, S., Turk, G., Svensson, S., Hozjan, T. 2014. Implementation of fully coupled heat and mass transport model to determine the behaviour of timber elements in fire. Proceedings of 13th World Conference on Timber Engineering (WCTE), Quebec City.

[89] Hozjan, T., Saje, M., Srpčič, S., Planinc, I. 2011. Fire analysis of steel-concrete composite beam with interlayer slip. Comput. Struct. 89: 189–200.

[90] Kolsek, J., Planinc, I., Saje, M., Hozjan, T. 2013. The fire analysis of a steel-concrete side-plated beam. Finite Elem. Anal. Des. 74: 93–110.

[91] Schnabl, S., Planinc, I., Turk, G., Srpčič, S. 2009. Fire analysis of timber composite beams with interlayer slip. Fire. Saf. J. 44: 770–778.

[92] Larsen, F., Ormarsson, S. 2013. Numerical and experimental study of moisture-induced stress and strain field developments in timber logs. Wood. Sci. Technol. 47: 837–852.

[93] Stamm, A. 1959. Bound-water diffusion into wood in the fiber direction. For. Prod. J. 9: 27–32.

[94] Pečenko, R., Svensson, S., Hozjan, T. 2015. Modelling heat and moisture transfer in timber exposed to fire. Int. J. Heat Mass Transfer 87: 598–605.

[95] Oden, J. T. 1967. Mechanics of Elastic Structures. New York, McGraw-Hill: 369 p.

[96] Schmidt, J., Kaliske, M. 2009. Models for numerical failure analysis of wooden structures. Eng. Struct. 31: 571–579.

[97] Kirkegaard, P. A., Sørensen, J. D., Čizmar, D., Rajčič, V. 2011. System reliability of timber structures with ductile behaviour. Eng. Struct. 33: 3093–3098.

[98] Jorissen, A., Fragiacomo, M. 2011. General notes on ductility in timber structures. Eng. Struct. 33: 2987–2997.

[99] Probabilistic Model Code: Part III - Resistance Models. 2006. Joint Committee of Structural Safety. <http://www.jcss.byg.dtu.dk/>(Acquired: 26.6.2015).

[100] Glos, P. 1981. *Zur Modellierung des Festigkeitsverhaltens von Bauholz bei Druck-, Zug- und Biegebeanspruchung. Berichte zur Zuverlässigkeitstheorie der Bauwerke*. Munich, Sonderforschungsbeieich 96, Lab. f. d. Konstruktiven Ingenieurbau (LKI): 59 p.

[101] Srpčič, S. 1991. *Račun vpliva požara na jeklene konstrukcije*. Doktorska disertacija, Univerza v Ljubljani, Fakulteta za gradbeništvo in geodezijo, Oddelek za gradbeništvo, Konstrukcijska smer: 104 p.

[102] Bratina, S. 2003. *Odziv armiranobetonskih linijskih konstrukcij na požarno obtežbo*. Doktorska disertacija, Univerza v Ljubljani, Fakulteta za gradbeništvo in geodezijo, Oddelek za gradbeništvo, Konstrukcijska smer: 159 p.

[103] Simo, J. C., Hughes, T. J. R. 1998. Computational Inelasticity. New York, Springer: 392 p.

[104] Ibrahimbegovic, A. 2009. Nonlinear solid mechanics: Theoretical formulations and finite element solution methods. Dordrecht, Springer: 574 p.

[105] Christoph, N., Brettel, G. 1977. *Untersuchungen zur Wärmedehnung von Holz in Abhängigkeit von Rohdichte und Temperatur*. Holz als Roh - und Werkstoff 35: 99–108.

[106] Stanek, M., Turk, G. 2002. *Trdnost*. Univerza v Ljubljani, Fakulteta za gradbeništvo in geodezijo, Oddelek za gradbeništvo, Katedra za mehaniko: 704 p.
<http://www.km.fgg.uni-lj.si/predmeti/trdnost-uni/data/ucbenik/trdnost1.pdf >.

[107] LUSAS. 2013. Engineering analysis software, version 14.7. LUSAS, Kingston upon Thames, United Kingdom. <www.lusas.com>.

[108] COMSOL. 2012. COMSOL Multiphysics, version 4.3. Burlington, Massachusetts, United States. <http://www.comsol.com/>.

[109] Green, D. W., Jerrold, E., Kretschmann, D. E. 1999. Mechanical properties of wood. Wood handbook: wood as an engineering material. General technical report FPL. Madison, USDA Forest Service, Forest Products Laboratory: 45 p.

[110] EN 1995-1-1 2005, Eurocode 5: Design of Timber Structures - Part 1-1: General - Common rules and rules for buildings. European committee for standardisation. brussels: 123 p.

[111] EN 1990 2004. Eurocode - Basis of structural design. European committee for standardisation. Brussels: 87p.

[112] Guo, Q., Shi, K., Jia, Z., Jeffers, A. E. 2012. Probabilistic evaluation of structural fire resistance. Fire. Tech. 49: 793–811.

[113] Das, P. K., Zhang, W. 2003. Guidance on Structural Reliability Analysis of Marine Structures. Glasgow, Universities of Glasgow and Strathclyde, Department of Naval Architecture & Marine Engineering: 181 p.

[114] Toratti, T., Schnabl, S., Turk, G. 2007. Reliability analysis of a glulam beam. Struct. Saf. 29: 279–293.

[115] Hietaniemi, J. 2007. Probabilistic simulation of fire endurance of a wooden beam. Struct. Saf. 29: 322–336.

[116] Pieniak, D., Ogrodnik, P., Oszust, M., Niewczas, A. 2013. Reliability of the thermal treated timber and wood-based materials in high temperatures. Maintenance and Reliab. 15: 18–24.

[117] Iman, R. C., Conover, W. J. 1980. Small sample sensitivity analysis techniques for computer models with an application to risk assessment. Communications in Statistics: Theor. Meth. A 9: 1749–1842.

[118] Iman, R. C., Conover, W. J. 1982. A distribution free approach to inducing rank correlation among input variables. Communications in Statistics B 11: 311–334.

[119] Vořechovský, M., Novák, D. 2009. Correlation control in small-sample monte carlo type simulations i: A simulated annealing approach. Probabilist. Eng. Mech. 24: 452–462.

[120] Choi, S. K., Grandhi, R. V., Canfield, R. A. 2007. Reliability-based structural design. London, Springer-Verlag: 308 p.

[121] Probabilistic Model Code: Part II - Load Models. 2001. Joint Committee of Structural Safety. <http://www.jcss.byg.dtu.dk/>(Acquired: 26.6.2015).

[122] Culver, C. G. 1976. Survey results for fire loads and live loads in office buildings. Washington D.C., National Bureau of Standards: 150 p.

[123] Iqbal, S., Harichandran, R. 2010. Capacity reduction and fire load factors for design of steel members exposed to fire. J. Struct. Eng. 136: 1554–1562.

[124] Kiran, M. C., Nandanwar, A., Venugopal, N. M., Rajulu, K. 2012. Effect of density on thermal conductivity of bamboo mat board. Int. J. Agr. Forest. 2: 257–261.

[125] GiiP d.o.o. 2011. Construction design, Multipurpose sport hall.

[126] Hietaniemi, J., Mikkola, E. 2010. Design Fires for Fire Safety Engineering. VTT Working Papers 139. VTT Technical Research Centre of Finland: 101 p.

[127] McGrattan, K., Klein, B., Hostikka, S., Floyd, J. 2007. Fire Dynamics Simulator (Version 5) User's Guide. NIST Special Publication 1019-5. Washington, U.S. Government Printing Office: 86 p.

[128] Hopkins, D. 1995. Predicting the Ignition Time and Burning Rate of Thermoplastics in the Cone Calorimeter. Master's thesis. College Park, University of Maryland, Department of Fire Protection Engineering: 177 p.

[129] Pečenko, R., Huč, S., Hozjan, T. 2015. Performančni način projektiranja požarne odpornosti lepljenega lesenega nosilca. Del 2, Toplotna in mehanska analiza. Gradbeni vestnik 64: 134–144.